



저작자표시-비영리-변경금지 2.0 대한민국

이용자는 아래의 조건을 따르는 경우에 한하여 자유롭게

- 이 저작물을 복제, 배포, 전송, 전시, 공연 및 방송할 수 있습니다.

다음과 같은 조건을 따라야 합니다:



저작자표시. 귀하는 원저작자를 표시하여야 합니다.



비영리. 귀하는 이 저작물을 영리 목적으로 이용할 수 없습니다.



변경금지. 귀하는 이 저작물을 개작, 변형 또는 가공할 수 없습니다.

- 귀하는, 이 저작물의 재이용이나 배포의 경우, 이 저작물에 적용된 이용허락조건을 명확하게 나타내어야 합니다.
- 저작권자로부터 별도의 허가를 받으면 이러한 조건들은 적용되지 않습니다.

저작권법에 따른 이용자의 권리는 위의 내용에 의하여 영향을 받지 않습니다.

이것은 [이용허락규약\(Legal Code\)](#)을 이해하기 쉽게 요약한 것입니다.

[Disclaimer](#)

Doctoral Thesis

Smart Surgical Microscope based on
Optical Coherence Domain Reflectometry

SungWon Shin

Department of Biomedical Engineering

Graduate School of UNIST

2017

Smart Surgical Microscope based on Optical Coherence Domain Reflectometry

SungWon Shin

Department of Biomedical Engineering

Graduate School of UNIST

Smart Surgical Microscope based on Optical Coherence Domain Reflectometry

A thesis submitted to the Graduate School of UNIST
in partial fulfillment of the requirements
for the degree of Doctor of Philosophy

SungWon Shin

06. 21. 2017

Approved by



Advisor

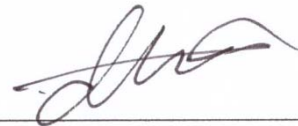
Woonggyu Jung

Smart Surgical Microscope based on Optical Coherence Domain Reflectometry

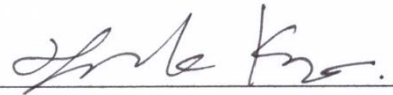
SungWon Shin

This certifies that the thesis of SungWon Shin is approved.

06. 21. 2017



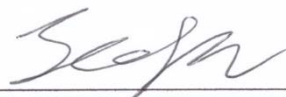
Advisor: Woonggyu Jung



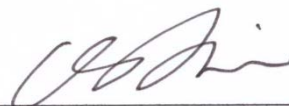
Hyun-Wook Kang



Jung-Hoon Park



Jeehyun Kim



Chang-Seok Kim

Abstract

Over the several decades, there have been clinical needs that requires advanced technologies in medicine. Optical coherence tomography (OCT), one of the newly emerged medical imaging devices, provides non-invasive cross-sectional images in high resolution which is mainly used in ophthalmology. However, due to the limited penetration depth of 1-2 mm in bio-samples, there is a limit to be widely used. In order to easily integrate with existing medical tools and be convenient to users, it is necessary that the sample unit of OCT should be compact and simple.

In this study, we developed high-speed swept-source OCT (SS-OCT) for advanced screening of otolaryngology. Synchronized signal sampling with a high-speed digitizer using a clock signal from a swept laser source, its trigger signal is also used to synchronize with the movement of the scanning mirror. The SS-OCT system can reliably provide high-throughput images, and two-axis scanning of galvano mirrors enables real-time acquisition of 3D data. Graphic processing unit (GPU) can performs high-speed data processing through parallel programming, and can also implement perspective projection 3D OCT visualization with optimal ray casting techniques. In the Clinical Study of Otolaryngology, OCT was applied to identify the microscopic extrathyroidal extension (mETE) of papillary thyroid cancer (PTC). As a result to detect the mETE of around 60% in conventional ultrasonography, it could be improved to 84.1% accuracy in our study. The detection ratio of the mETE was calculated by the pathologist analyzing the histologic image.

In chapter 3, we present a novel study using combined OCT system integrated with a conventional surgical microscope. In the current set-up of surgical microscope, only two-dimensional microscopic images through the eyepiece view are provided to the surgeon. Thus, image-guided surgery, which provides real-time image information of the tissues or the organs, has been developed as an advanced surgical technique. This study illustrate newly designed optical set-up of smart surgical microscope that combined sample arm of the OCT with an existing microscope. Specifically, we used a beam projector to overlay OCT images on existing eyepiece views, and demonstrated augmented reality images.

In chapter 4, in order to develop novel microsurgical instruments, optical coherence domain reflectometry (OCDR) was applied. Introduces smart surgical forceps using OCDR as a sensor that provides high-speed, high-resolution distance information in the tissue. To attach the sensor to the forceps, the lensed fiber which is a small and high sensitivity sensor was fabricated and the results are shown to be less affected by the tilt angle. In addition, the piezo actuator compensates the hand tremor, resulting in a reduction in the human hand tremor of 5 to 15 Hz.

Finally, M-mode OCT needle is proposed for microsurgery guidance in ophthalmic surgery. Stepwise transitional core (STC) fiber was applied as a sensor to measure information within the tissue and attached to a 26 gauge needle. It shows the modified OCT system and the position-guided needle design of the sample stage and shows the algorithm flowchart of M-mode OCT imaging software. The developed M-mode OCT needle has been applied to animal studies using rabbit eyes and demonstrates the big-bubble deep anterior lamellar keratoplasty (DALK) surgery for corneal transplantation. Through this study, we propose a novel microsurgical instrument for lamellar keratoplasty and evaluate its feasibility with conventional regular OCT system images.

In conclusion, for fundamental study required new augmented reality guided surgery with smart surgical microscope, it is expected that OCT combined with surgical microscope can be widely used. We demonstrated a novel microsurgical instrument to share with light source and the various optical components. Acquired information throughout our integrated system would be a key method to meet a wide range of different clinical needs in the real world.

Table of Contents

Abstract.....	1
Table of Contents.....	3
List of figures and tables	5
CHAPTER 1. General background	12
1.1 Medical imaging technology	12
1.2 History of OCT	13
1.3 Principles of OCT	21
1.3.1 Interference and interferometers	21
1.3.2 Fourier-domain optical coherence tomography.....	24
1.4 Research motivations	26
CHAPTER 2. Real-time OCT for advanced screening in surgery	27
2.1 Development of high-speed SS-OCT	27
2.2 Configuration of OCT software	30
2.3 Three-dimensional OCT visualization.....	37
2.4 Clinical study for otolaryngology.....	40
2.4.1 Microscopic extrathyroidal extension.....	40
2.4.2 OCT imaging to identify mETE	40
2.4.3 Result	41
2.5 Conclusions	46

CHAPTER 3. Smart surgical microscope	47
3.1 Microscope integrated OCT	47
3.2 Design for smart surgical microscope	50
3.2.1 Advanced methods for OCT and microscope integration.....	50
3.2.2 Augmented-reality imaging under smart surgical microscope.....	56
3.3 Conclusions	57
CHAPTER 4. Novel microsurgical instruments	58
4.1 Intro: Optical coherence domain reflectometry	58
4.2 Smart surgical forceps	58
4.3 Microsurgery guidance for ophthalmic surgery.....	67
4.3.1 Motivation: lamellar keratoplasty	67
4.3.2 M-mode OCT needle	70
4.3.3 Result	75
4.4 Conclusion.....	83
CHAPTER 5. Concluding remarks.....	84
References	85

List of figures and tables

Figure 1-1. Penetration depth and resolution of imaging modalities. The OCT technology covers both in research and medical imaging.	14
Figure 1-2. Comparison of OCT and histology [4]. The left side is invasive ductal carcinoma and the right side is normal fatty tissue. In the OCT image, we can show tissue density and separation as shown in the graphs above.	15
Figure 1-3. Commercialized OCT machines in ophthalmology. (A) iVue (Optovue incorporated), (B) EnFocus (Leica Microsystems), (C) Envisu C2300 (Leica Microsystems), (D) Cirrus HD-OCT 5000 (Carl Zeiss Meditec).	16
Figure 1-4. 2D and 3D OCT images of finger. C-mode was acquired at $1024 \times 500 \times 500$ pixel with our customized OCT system.	17
Figure 1-5. Schematics of various imaging probes. (Upper) OCT forward-imaging instruments, probe telescope and laparoscope [16], (Bottom) Schematics of two imaging needle designs [19].	18
Figure 1-6. Hand-held OCT scanner and 3D endoscopic MEMS probe. (Upper) The scanner consisted of galvanometer-mounted mirrors, interchangeable lens mounts, and miniaturized video camera [17]. (Bottom) The probe was based on dual-axis scanning MEMS mirror and integrated with an OCT system for volume imaging [18].	19
Figure 1-7. Intraoperative optical coherence tomography using the RESCAN 700 [23]. The OCT images were marked with a red arrow, and a yellow arrow indicates the heads-up display for surgeon.	20
Figure 1-8. Michelson and Mach-Zehnder interferometers. (A) Basic scheme of OCT with a Michelson interferometer, (B) Mach-Zehnder interferometer. LS-light source, RM-reference mirror, L-lens, SAM-sample, DU-detection unit, BS-beam splitter.	23

Figure 1-9. Two ways of Fourier domain OCT techniques. (a) The SD-OCT measures the signal using a spectrometer as a detector of the interferometer. (b) SS-OCT operates as a swept source laser and single photo detector.	25
Figure 2-1. System schematics for high speed SS-OCT with Mach-Zehnder interferometry. Fiber based optical setup for SS-OCT with swept laser, coupler and circulator. Optical signal acquisition is completed through DAQ board and digitizer.	28
Figure 2-2. User Interface made by LabVIEW software for high speed SS-OCT. The user can control scanning range, number of sampling, file saving path raw A-line profiles and OCT images shown in single window.	29
Figure 2-3. Block diagram of galvano mirror control. Through the DAQ and sweep trigger signal of swept laser source, galvano mirror is controlled with two perpendicular axis of x and y. To simplify the code, customized subVI for signal generation was applied (red box).	32
Figure 2-4. Block diagram of digitizer settings and raw signal acquisition. To synchronize digitizer, we applied external trigger and voltage level by independent setting values (top) and acquired raw optical signal data within acquisition loop (bottom).	33
Figure 2-5. Block diagram of FFT signal processing through CUDA library for LabVIEW. To increase computational speed, GPU was installed into CUDA LabVIEW library for setting (top) and multi-dimensional FFT procedure (bottom).	34
Figure 2-6. Block diagram of saving OCT image. After FFT through CUDA, B-mode OCT image is visualized in intensity chart and saved through image save function.	35
Figure 2-7. Block diagram of multi-thread through queue. For multi-thread parallel processing, queue functions are applied to separate acquisition and processing procedures.	36
Figure 2-8. Signal processing flow chart of the multi thread structured GPU architecture for 3D visualization. Solid arrows, main data stream; Hollow arrows, internal data flow;	38

Red box, flow chart of the 3D volume Rendering.

Figure 2-9. LabVIEW block diagram of the real-time 3D OCT image visualization. With 39
 the customized dll file (red box), real-time volume rendering can be obtained. The event structure enables 3D rendered object to be rotated, scaled, shifted by moving mouse (green box).

Figure 2-10. The OCT images and histologic images showing histological features of the 42
 normal thyroid gland [59]. White bar - 1mm, Arrow head - lymphatics, Short arrow - vessels, Asterisk - thyroid follicle, Long arrow - adipose tissue.

Figure 2-11. Comparison of ultrasound, OCT, and histologic images of thyroid cancer 43
 tissue with no ETE [59]. Arrow head and short arrow indicate confined thyroid tumor within the capsule.

Figure 2-12. Comparison of ultrasound, OCT, and histologic images of thyroid cancer 43
 tissue demonstrates minimal ETE (arrow head and short arrow) [59].

Figure 2-13. 3D OCT image of papillary thyroid cancer acquired from one patient with 44
 no mETE. The tumor was identified to be surrounded by capsule with normal tissue (arrow head and short arrow) [59].

Table 2-1. The interpretation result from two investigators. OCT images were evaluated 45
 to identify mETE. The accuracy of mETE detection was 84.1% and 85.3% for two inspectors [59].

Figure 3-1. Various medical imaging systems of Carl Zeiss. (a) A typical ophthalmic 49
 OCT system currently being used most actively in ophthalmology. (b) An intraoperative OCT system that can be diagnosed separately in the operating room next to the surgical microscope. (c) Combination of OCT with a surgical microscope called MI-OCT.

Figure 3-2. Configuration of SS-OCT system. The voltage signal from the balanced 52
 detector is collected through the digitizer, and the Daq board is synchronized with the clock signal from the swept laser source to control the galvanometer scanner. *PC: Polarization Controller.

Figure 3-3. Schematics of 3D CAD design for OCT sample arm with the surgical microscope. (a) 3D model drawings of the hardware components. (b) Assembled design. (c) Schematic of the optical components in the hardware. Optical part consisting of the galvano-mirror, surgical microscope, microscope objective lens, mirror, objective lens, dichroic mirror are designed to attached to the surgical microscope system.	53
Figure 3-4. Configuration of MI-OCT system. Swept- source Laser (SL), Coupler (C), Circulator (Cir), Collimator (Col), L (Lens), Mirror (M), Polarization Controller (PC), Balanced Detector (BD),and PC. Sample Arm attached microscope includes Collimator, Galvano-Mirror (GM), Lens, Beam Splitter (BS), Dichromatic Mirror (DM), Beam projector (BP), ND-filter (NDF).	54
Figure 3-5. Completed MI-OCT system which can be called a smart surgical microscope. It is easily integrated with additional medical devices sharing light source of the OCT.	55
Figure 3-6. Augmented-reality image from smart surgical microscope. (A) Microscopic image in the eyepiece of the surgical microscope. (B) 3D OCT image acquired from high-speed SS-OCT. (C) Scene captured from the eyepiece view that overlays the OCT image on the microscopic image using a beam projector.	56
Figure 4-1. Simulation of the lensed fiber with general equation. (a) Equations of the general ABCD matrix ray transform matrix and working distance and beam diameter. (b) Simulation result of the working distance, (c) beam diameter according to variation of the radius of curvature.	61
Figure 4-2. Fabrication process of a fiber optic probe. (a) Fabrication process of the lensed fiber. (b) Comparison of the lensed fiber size with coin of 22mm diameter. (c) Image of lensed fiber captured with conventional microscope. (d) Simulation of the lensed fiber beam propagation. Cross-section of the beam from the lensed fiber forms the smallest when working distance (WD) corresponds to the focal point (w_0).	62
Table 4-1. Comparison of actuators of various performance. The LL1011A piezo actuator model was selected to compensate for operator hand tremors.	63

Figure 4-3. Schematic of cross-sectional image for intelligent micro forceps. It consists of a piezo actuator used for motion compensation, a case designed to protect against external influences, and a fiber optic probe for distance measurement. 64

Figure 4-4. The intelligent forceps for hand tremor compensation. (Upper) Schematic of 3D CAD modeling. (Bottom) The actual device in which each part is fully assembled and completed. 65

Figure 4-5. System of the intelligent micro-forceps. (a) Image of the intelligent forceps attached on the micro stage for adjusting the distance from the sample. (b) System configuration consisting the Swept source laser, balanced photo detector, and piezo motor driver. (c) Graph of the tip position relative to the target surface while free hand and compensation actuator assisted detecting from the lensed fiber. The Root Mean Square (RMS) value under 20 seconds is 202.92, first compensation interval (20–40 sec) is 9.01. (d) The Fourier analysis of the tip position signal graphs. Here, the amplitude of the free hand and compensated Fourier signal around the major tremor frequency of human, which is from 5 to 15 Hz, is 83.6 and 72.6, respectively. The amplitude of the compensation actuator assisted forceps shows relatively lower in the most of the frequency area. Especially, 13.8 dB is reduced at the major hand tremor frequency band. 66

Figure 4-6. Schematics of anterior segment of human eye. Corneal structure consists of five layers with different thicknesses. The total thickness is about five-hundred and eighty micro-meter. 68

Figure 4-7. Anwar's big-bubble technique for successful DALK surgery. The air is injected through a thin syringe needle that is inserted inside the patient's cornea. The air blow softly makes uniform corneal segments by inflating the air bubble in the cornea. 69

Figure 4-8. Design of position-guided needle. (A) Schematic of stepwise transitional core (STC) fiber [105]. (B) 3D CAD of STC fiber integrated needle. (C) Photo of STC fiber wrapped in metal jacket. (D) Complete position-guided needle applied to 26 gauge needle. 71

Figure 4-9. Schematic and 2D/3D OCT images of regular OCT imaging system. (A) Schematic of regular OCT imaging system. (B) Microscopic image of rabbit eyeball. (C) 72

3D OCT image of rabbit eyeball. (D) Cross-sectional image with regular OCT imaging system.

Figure 4-10. Flow chart of computational steps for real-time M-mode OCT imaging. A 73
high-speed digitizer was used for data acquisition, and M-mode images were displayed on the time-intensity chart through signal processing.

Figure 4-11. Performance representing chart for system sensitivity and latency. (A) SNR 78
graph of STC fiber integrated position-guided needle represent decrease of signal intensity to 12 dB across depth range of 2 mm. (B) Latency histogram of the M-mode OCT imaging system. The average of loop time was 10.008 milliseconds with maximum 8.534 milliseconds and standard deviation of 0.184. SD* : standard deviation.

Figure 4-12. Phantom study evaluating the feasibility of the position-guided needle 79
combined with M-mode OCT. (A) Schematic diagram of phantom study. (B) Corneal mimicking phantom developed with double layers of different concentrated agarose. (C1)-(C3) regular OCT image was presented when the needle punched through the surface of agarose jell and passed by the middle of first layer at 1.68 sec, and came closer to 2nd layer at 4.14 sec, respectively. (D) M-mode imaging from position-guided needle in real time that has capability of tracking depth information. Red and yellow arrows denote the residual thickness between the needle distal end and the boundary (assuming the Descemet's membrane and endothelium) within the phantom, respectively.

Figure 4-13. Animal study on rabbit eyeball demonstrating the M-mode OCT needle. 80
(A1) Animal surgery using position-guided needle when the tip of needle was inserted into the first layer of cornea. (A2) The corresponding M-mode OCT image from the needle when its tip was maintaining the cornea layer with residual thickness of around 300 μ m. (B1) Next medical procedure when the surgeon was aided with the needle to quantitatively find out the desired position of cornea. (B2) The corresponding M-mode OCT image was captured when the needle approached near Descemet's membrane (DM) of the enucleated rabbit eyeball and detected the rest of cornea thickness within 100 μ m.

Figure 4-14. Anterior chamber made with 3D printer to hold rabbit eyes. (A1)-(A3) 81
Process of inserting needle before air injection into the rabbit eye. (B) Failed big-bubble case 1, 2 and successful big-bubble case 3, 4 after air injection.

Figure 4-15. $512 \times 500 \times 500$ voxel of OCT image was captured immediately after needle tip reached the remained cornea layer with thickness of 100um. (A1) – (A4) 3D OCT image, en-face image, and cross sectional images in different view before air injection. (B1) – (B4) after air injection.

CHAPTER 1. General background

1.1 Medical imaging technology

Medical imaging is an indispensable technique to our lives which shed light on hidden internal structures in human body. It realizes visual representation for diagnosis, clinical analysis, medical intervention and treatment of abnormally functioned region. In particular, medical imaging has made such a huge breakthrough by transitioning the technique from invasive to non-invasive. Correspondingly, there has been trials and errors to create new type of imaging modality. In the past, most of imaging technique has been limited in providing two-dimensional (2D) information only, but over the several decades many technologies for 3D or real-time 3D (4D) display have been introduced. The newly invented 3D tomographic techniques in medicine are Radiography (X-ray), Computed Tomography (CT), Nuclear Medicine (SPECT, PET), Ultrasound (US), and Magnetic Resonance Imaging (MRI), respectively. These imaging modalities have been used primarily to diagnose diseases.

Medical imaging technology is not only beneficial to provide clinical information for diagnosis, but also play the crucial role of helping surgeon such in image guided surgery by tracking surgical instruments. For example, advanced medical imaging devices such as CT or MRI scanners can be used to treat surgery for brain tumors [1, 2]. Like this, recent medical imaging technology has a wide range of applications and is being applied to various studies to improve clinical guide in the field of microsurgery.

The optical coherence tomography (OCT) system which will be discussed in this study has also great potential as an emerged medical imaging tool capable of acquiring cross-sectional images noninvasively [3]. Unlike imaging modalities of conventional MRI / CT mentioned above, OCT has the advantage of being harmless to the human body providing high resolution of microscale as presented Figure 1-1 and Figure 1-2 [4]. Nowadays, the OCT system can be assembled with low-cost (Figure 1-3), and its probe can be miniaturized which is fit to micro-surgery, so that it can be presented as a solution to various clinical needs [5-7].

1.2 History of OCT

Optical coherence tomography (OCT) technology was first demonstrated in 1991 by Huang et al., under the discipline of Prof. James Fujimoto at Massachusetts Institute of Technology. OCT is a non-contact imaging modality that can detect photons backscattered from different layer of specimen with high sensitivity and micrometer scale spatial resolution [8, 9]. Since OCT provides cross-sectional, high-resolution images in the human eye, it has become a gold standard for disease diagnosis and therapeutic response tracking in ophthalmology. The first in vivo OCT image for displaying Retina structures was published in 1993, and many studies have begun to adopt OCT into clinics since then [10, 11].

The OCT system can be mainly categorized into two different types, time domain OCT (TD-OCT) and Fourier domain OCT (FD-OCT). The TD-OCT, the first generation of OCT, had a limitation on the acquisition speed due to mechanical movement in the reference arm. To overcome this problem addressed in TD-OCT, the next generation of FD-OCT, which has been mainly used since the 2000's, fixes the reference arm and uses the spectrometer (SD-OCT) or the swept source laser (SS-OCT) [12-15]. These FD-OCT methods are easy to acquire high-speed tomographic images, and it has become possible to provide three-dimensional OCT (3D OCT) images in real time as shown in Figure 1-4. In addition, FD-OCT gives high SNR characteristics of 20-30 dB advantage over TD-OCT, so it is applied to various clinical studies.

A study using OCT probes was first proposed in 1997 as a forward-imaging handheld OCT (HH-OCT) probe using a piezoelectric cantilever [16]. Since the mid-2000's, the HH-OCT with 3D endoscopic probe assembled with galvanometer [17] and 2D microelectromechanical scan method was proposed by W. Jung et al. These probes shows great improvement of utility of compact probe in that it provides a high quality of three dimensional imaging with small size of probe body optimized to human endoscopy [18]. Furthermore, studies using HH-OCT probe have made it possible to perform patient monitoring which has previously been difficult to check with conventional tabletop type OCT system. In 2000, a study utilizing needle-type OCT probes for deep tissue imaging was introduced by Fujimoto et al. in the paper of *imaging needle for optical coherence tomography* [19]. The key technique addressed in this study was to overcome the depth limitation of traditional OCT scanners, so that it consequently allowed OCT to be applied as an intraoperative method in clinics. These HH-OCT and needle-type imaging probes are shown in Figure 1-5, 1-6.

Even though studies on OCT and its probes has been developed for the main purpose of surgical use, there is still a limitation that the primary surgeon cannot monitor on specific site they are aiming. An alternative approach to solve this problem is to integrate the OCT sample arm into the operating microscope. This consideration can be referred to as MI-OCT, which was suggested by Y. K. Tao et al. It made possible for the surgeon to feed back the OCT image at the same time while performing the surgery [20-22]. Also, the RESCAN 700 (Carl Zeiss Meditec, Germany) is a microscope integrated intraoperative OCT system that provides surgeon with head-up display feedback. This commercial machine, shown in Figure 1-7, was used for visualization of instrument-tissue interactions during *en-face* retinal and ophthalmic surgery [23].

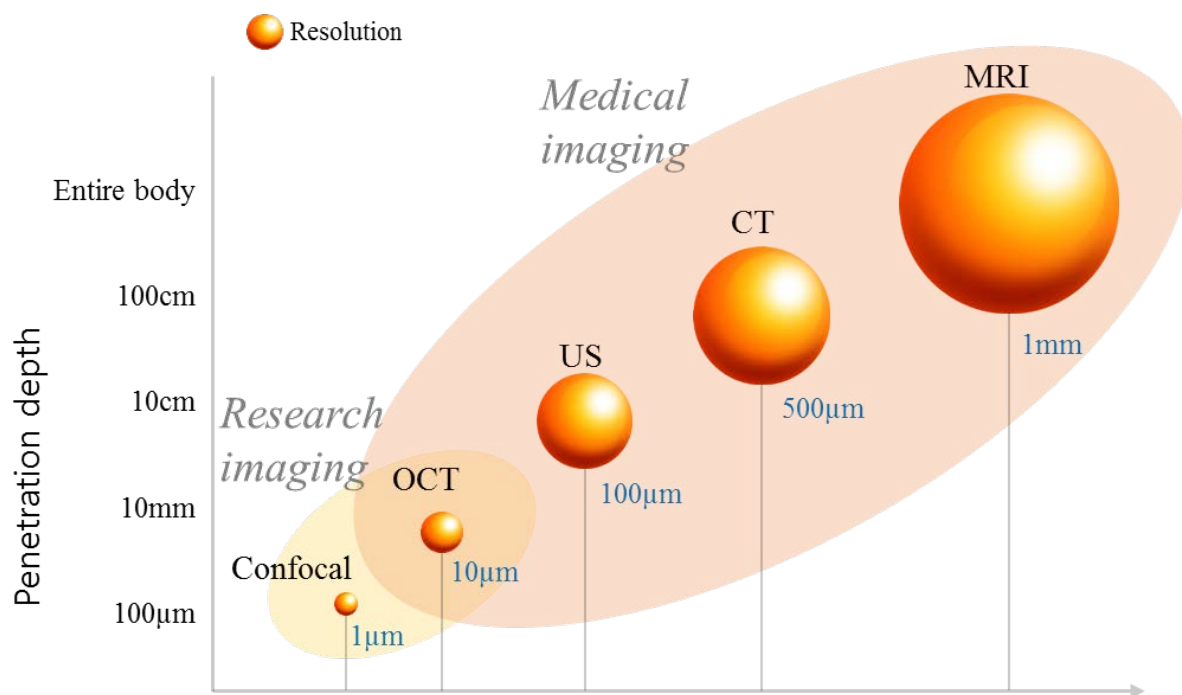


Figure 1-1. Penetration depth and resolution of imaging modalities. The OCT technology covers both in research and medical imaging.

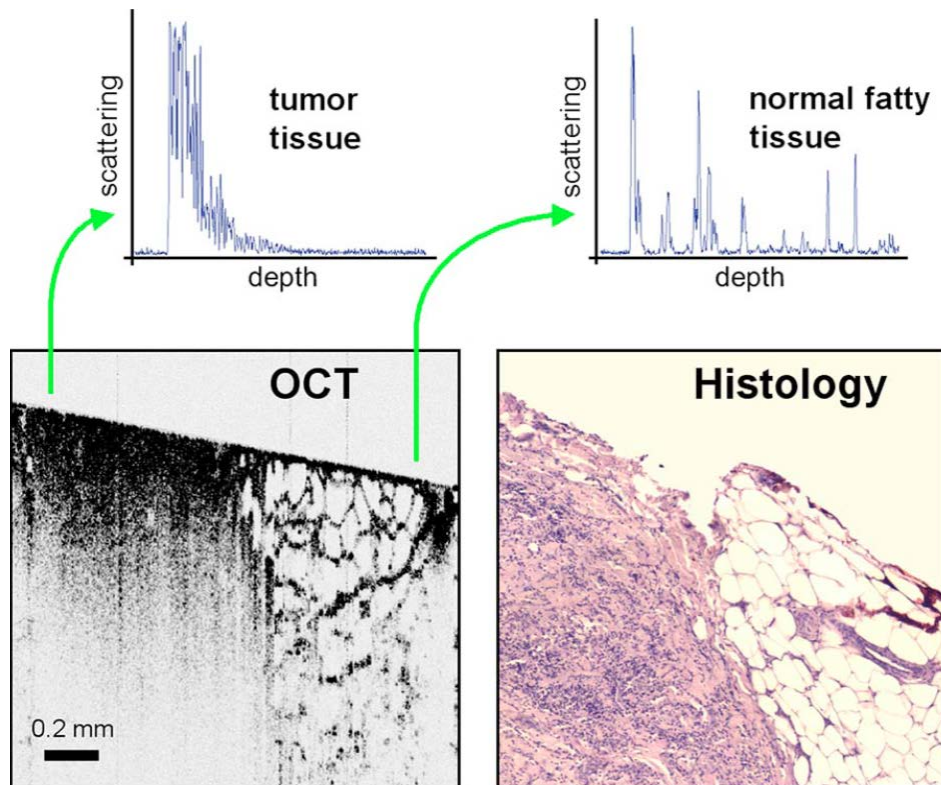


Figure 1-2. Comparison of OCT and histology [4]. The left side is invasive ductal carcinoma and the right side is normal fatty tissue. In the OCT image, we can show tissue density and separation as shown in the graphs above.



Figure 1-3. Commercialized OCT machines in ophthalmology. (A) iVue (Optovue incorporated), (B) EnFocus (Leica Microsystems), (C) Envisu C2300 (Leica Microsystems), (D) Cirrus HD-OCT 5000 (Carl Zeiss Meditec).

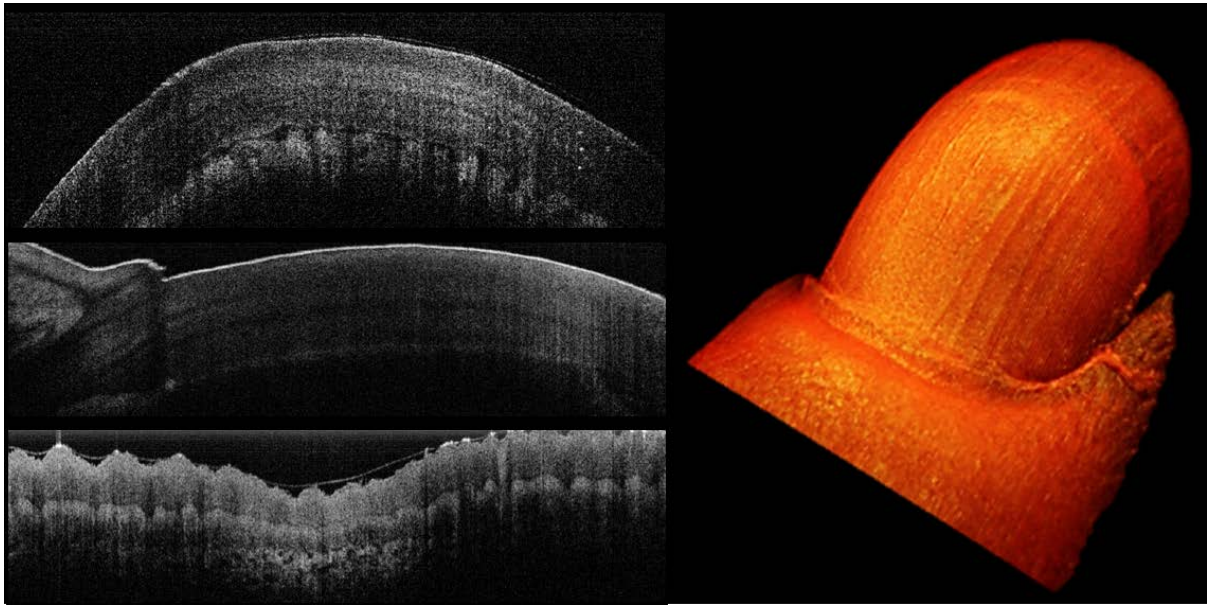


Figure 1-4. 2D and 3D OCT images of finger. C-mode was acquired at $1024 \times 500 \times 500$ pixel with our customized OCT system.

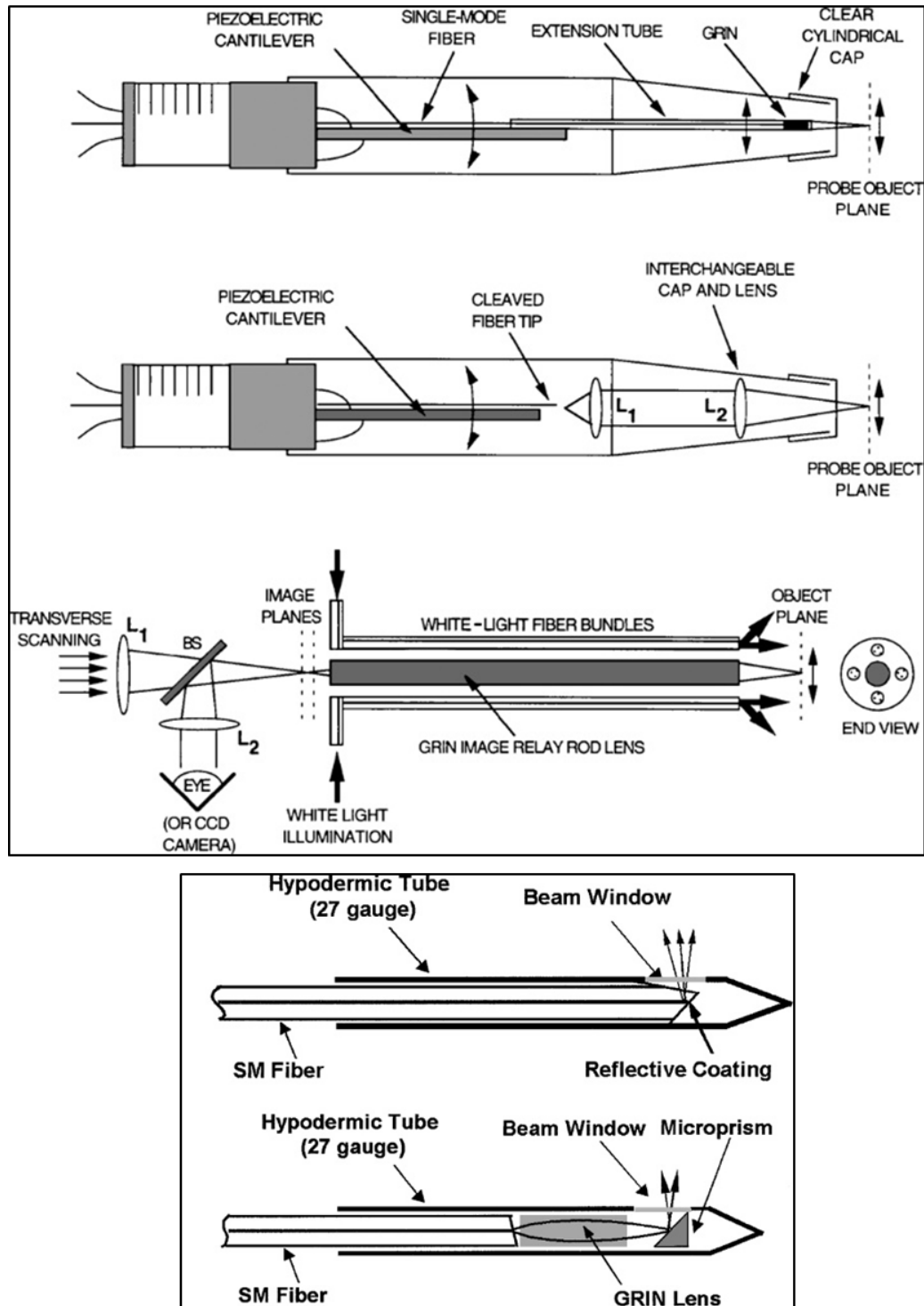


Figure 1-5. Schematics of various imaging probes. (Upper) OCT forward-imaging instruments, probe telescope and laparoscope [16], (Bottom) Schematics of two imaging needle designs [19].

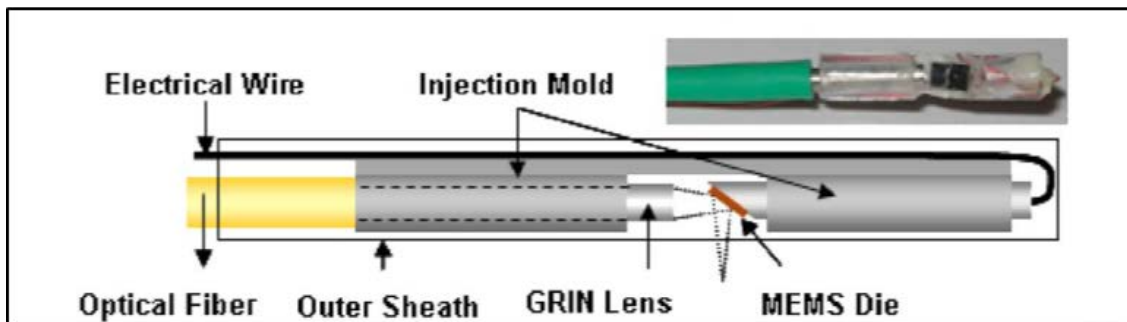


Figure 1-6. Hand-held OCT scanner and 3D endoscopic MEMS probe. (Upper) The scanner consisted of galvanometer-mounted mirrors, interchangeable lens mounts, and miniaturized video camera [17]. (Bottom) The probe was based on dual-axis scanning MEMS mirror and integrated with an OCT system for volume imaging [18].

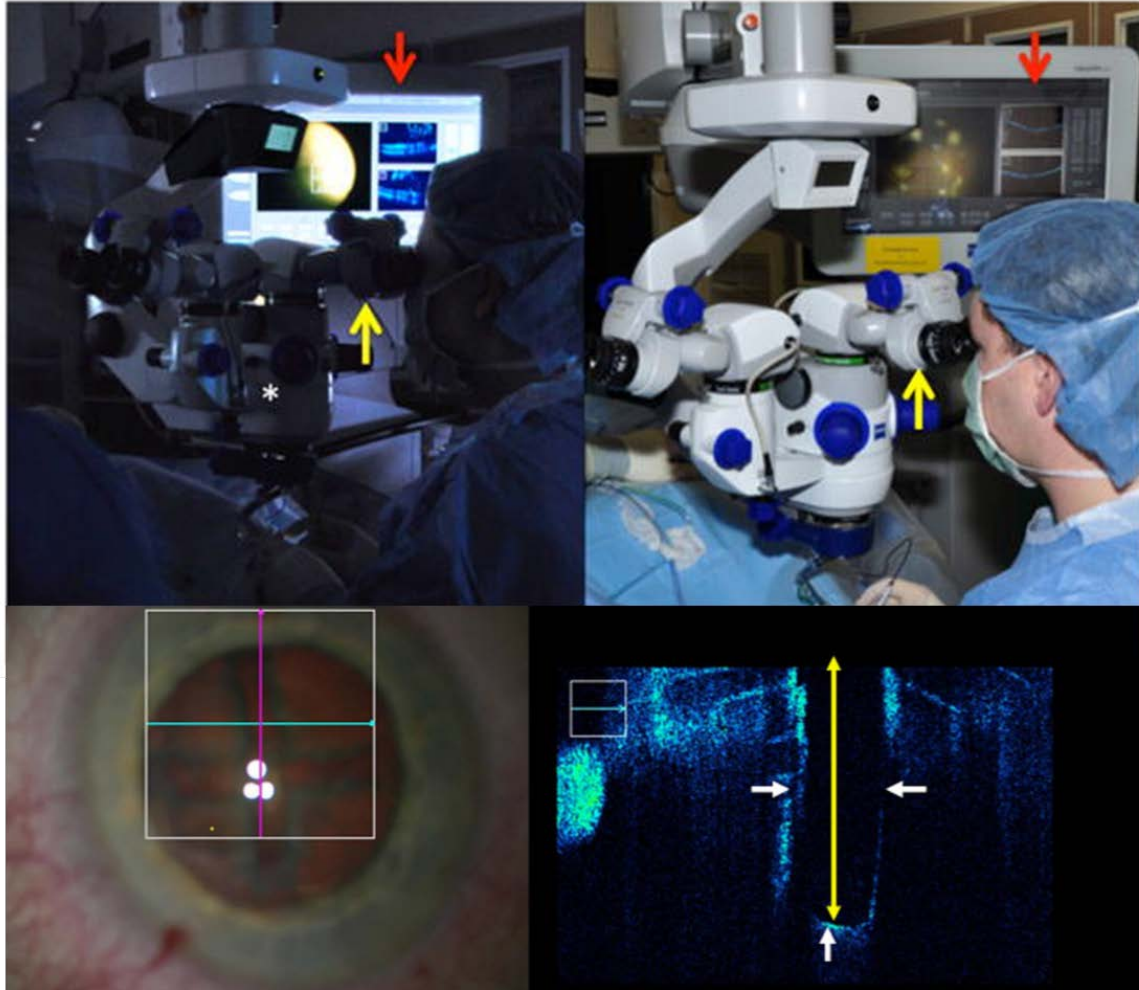


Figure 1-7. Intraoperative optical coherence tomography using the RESCAN 700 [23]. The OCT images were marked with a red arrow, and a yellow arrow indicates the heads-up display for surgeon.

1.3 Principles of OCT

1.3.1 Interference and interferometers

The optical coherence theory is a classical concept in optics that has been generalized for decades, and this chapter will summarize the basic theories [24-27]. Coherence effects can be divided into three types, temporal, spatial and spectral. First, temporal coherence is the extent of how the source holds the characteristics of monochromatic, leading to the concept of relation between coherence time and source bandwidth. For example, monochromatic laser has such a long coherent length with very narrow wavelength bandwidth, while white light source with broad bandwidth shows such a very short coherent length. Second, spatial coherence can be understood by cross correlation between two spatial positions. More simply explaining, this concept illustrates how one wave and its copy of wave have spatial interference at fixed time over the length. Third, spectral coherence represents relative phase relationship between waves of different wavelength. If the waves with temporally incoherent is formed to make interference, the resultant interference will be continuous and randomly fluctuating, while coherent waves make short and localized pulse.

For mathematical illustration, we assumed that two linearly polarized waves transverse in the direction of vector \vec{r} with monochromatic waves of the same frequency, ω , in a homogeneous medium.

$$\begin{aligned}\vec{E}_1 &= \vec{E}_{01} \cos(\vec{k}_1 \cdot \vec{r} - \omega t + \varepsilon_1) \rightarrow \vec{E}_{01} e^{i\theta_1} \\ \vec{E}_2 &= \vec{E}_{02} \cos(\vec{k}_2 \cdot \vec{r} - \omega t + \varepsilon_2) \rightarrow \vec{E}_{02} e^{i\theta_2}\end{aligned}\quad (1-1)$$

Since the two wave sources are assumed to be the same frequency, the phase difference, δ , can be summarized as follows.

$$\delta = \theta_1 - \theta_2 = \vec{k}_1 \cdot \vec{r} - \vec{k}_2 \cdot \vec{r} + \varepsilon_1 - \varepsilon_2 \quad (1-2)$$

The synthetic irradiance (I) when two waves met in Equation 1 is as follows.

$$\begin{aligned}
 I &= |\vec{E}|^2 = \vec{E} \cdot \vec{E} = (\vec{E}_1 + \vec{E}_2) \cdot (\vec{E}_1 + \vec{E}_2)^* \\
 &= |\vec{E}_{01}|^2 + |\vec{E}_{02}|^2 + 2|\vec{E}_{01}| \cdot |\vec{E}_{02}| \cos \delta \\
 &= I_1 + I_2 + 2|\vec{E}_{01}| \cdot |\vec{E}_{02}| \cos \delta
 \end{aligned} \tag{1-3}$$

In equation 3, the cosine term for the phase value is $-1 \leq \cos \delta \leq 1$, so the synthetic irradiance is not equal to the sum of each irradiance. In this equation, $2|\vec{E}_{01}| \cdot |\vec{E}_{02}| \cos \delta$ is called the interference term, and constructive interference occurs when the waves are in phase. At this time, an interference fringe pattern is produced, and the fringe contrast is given by

$$\text{fringe contrast} = \frac{I_{\max} - I_{\min}}{I_{\max} + I_{\min}} \tag{1-4}$$

To acquire high visibility in interferometry recorded in camera, the light source should be coherent temporally and spatially. As can be seen from Equation 4 above, a low coherence source used in OCT achieve high fringe contrast. Furthermore, the axial resolution is related to the bandwidth of light used in the interferometry. Adequate range of broad spectrum of light source in OCT is important to determine the axial resolution. Not only the axial resolution of the OCT, source bandwidth corresponds to the coherence length (l_c). For example, if the bandwidth of the light source at 1310 nm center wavelength (λ_0) is 100 nm, then the ideal axial resolution can be calculated as 7.55 μm , as defined in Equation 5 below.

$$l_c = \frac{2 \ln 2}{\pi} \cdot \frac{\lambda_0^2}{\Delta \lambda} \approx 0.44 \frac{\lambda_0^2}{\Delta \lambda} \tag{1-5}$$

Where $\Delta \lambda$ represents the full-width of the coherence function at half-maximum measured in wavelength units.

One of the main interferometric systems is the Michelson interferometer which is best known for double path interferometers [28-31]. The configuration of interferometry is composed of mainly two different light paths which are the sample arm and the reference arm, respectively. As shown in Figure 1-8(A) below, the beam from the source is split into two arms at beam-splitter. And the beam returning from the mirror of reference arm produces interference pattern with the reflected light from the sample. The resultant interferometric signal is measured and recorded by a photodiode detector. As described in Equation 3, constructive interference occurs only when the path-length between the reference mirror and the sample reflectors is matching within the coherence length of the light source.

Figure 1-8(B) shows the Mach-Zehnder interferometer. The paths are similar to the Michelson interferometer, which is used to provide an equal-spaced sampling signal clock in most SS-OCTs [32-35].

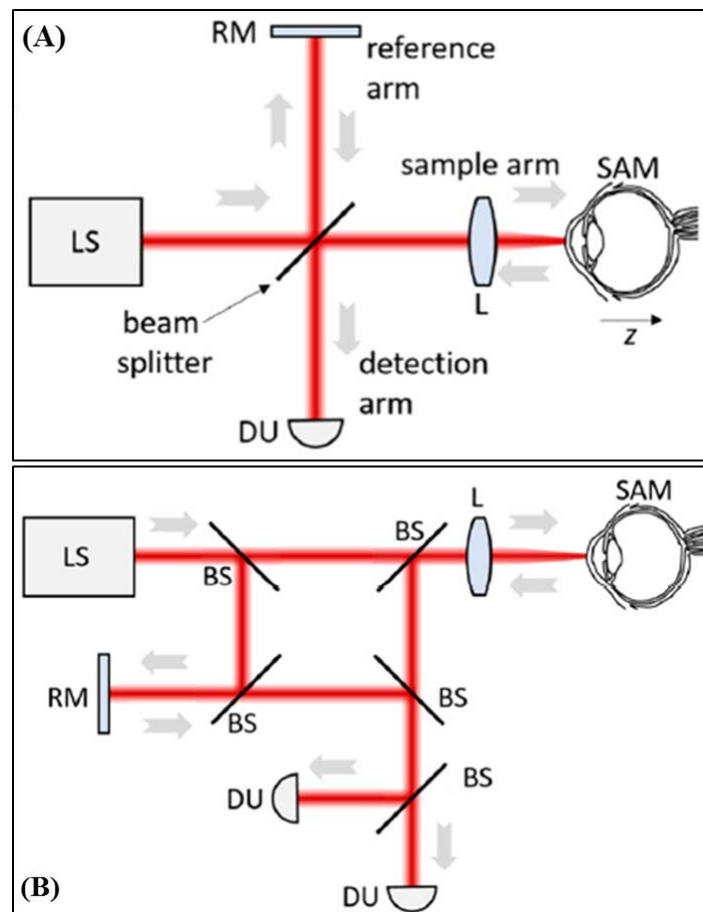


Figure 1-8. Michelson and Mach-Zehnder interferometers. (A) Basic scheme of OCT with a Michelson interferometer, (B) Mach-Zehnder interferometer. LS-light source, RM-reference mirror, L-lens, SAM-sample, DU-detection unit, BS-beam splitter.

1.3.2 Fourier-domain optical coherence tomography

The FD-OCT was first demonstrated by the Fercher group in 1995 [36], which offers a 10-fold higher rate of SNR characteristics of 20-30 dB compared to time-domain OCT (TD-OCT). Figure 1-9 illustrates the structure of the FD-OCT in two ways. First, figure 1-9(a) shows the spectral-domain OCT (SD-OCT) using a broad band light source and a high-resolution spectrometer. In this way, the acquisition speed and sensitivity of the spectrometer are important parameters for determining the performance of the OCT system. The spectrometer consists of the diffraction grating, the focusing lenses, and a photodiode array which is used for mainly charge coupled device (CCD) or complementary metal-oxide semiconductor (CMOS) type line scan camera. In SD-OCT, high-speed line scan camera of 100Khz or more enables image visualization at a rate of several tens of frames per second or more.

Next, Figure 1-9(b) shows a swept-source OCT (SS-OCT) using a swept source laser. In this method, a single photodetector and a data acquisition board with a sampling rate of several hundreds of megahertz (Mhz) or more are used, and other components similar to SD-OCT are used. The speed and resolution between the two methods of FD-OCT are basically similar, but SD-OCT is known to have some disadvantages. If the movement of the sample arm removes the interference fringes when the CCD camera is in pixel integration time, the image is blurred. Thus, unavailability from indium gallium arsenide (InGaAS) CCD cameras with higher pixel resolution limits the application for in-vivo endoscopic applications. Another approach to overcome the disadvantage of SD-OCT is a swept-source OCT using a continuous, repetitively tunable light source with frequency components analyzed over time by a single photodetector. There is no interference fringes removed in this technique, and longer wavelengths from 1um to 1.5um can be used for endoscopy. Therefore, SS-OCT is more advantageous for purposes such as endoscopic application.

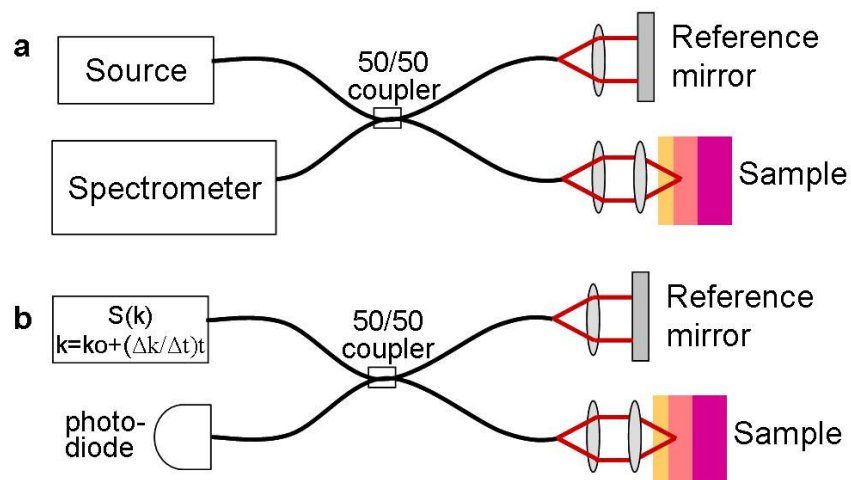


Figure 1-9. Two ways of Fourier domain OCT techniques. (a) The SD-OCT measures the signal using a spectrometer as a detector of the interferometer. (b) SS-OCT operates as a swept source laser and single photo detector.

1.4 Research motivations

Over the decades, there were increasing demand of numerous application in the field of microsurgery. Not only visualizing the top surface of region of surgical target, useful tool for microsurgery were required. OCT, which provides high-resolution images non-invasively in the living body, has potential as a clinical solution. Unlike the surgical microscope providing just two dimensional image of top view, OCT can perform multidimensional imaging in real time during surgical operation which make it to be applied on many surgical application over other imaging modalities. In particular, a smart surgical microscope integrated with label-free imaging technique of OCT is expected to be an alternative tool opening a new avenue as a key method of microsurgery in neurosurgery, pathology, and general surgery.

OCT is promising tool in terms of probe miniaturization at a low cost which offers a great possibility of a new surgical instrument. By combining the OCT with traditional surgical instruments such as forceps or needles, these tools can be compact imaging devices or novel surgical instruments. Surgical instruments based on optical technology may offer a way to revolutionize existing surgical techniques.

With these considerations, I believe that newly developed for surgical operation using optical technique will be used in the study addressed for solving the needs of clinics such as diagnosis and treatment. In this thesis, I will mainly demonstrate about the development of new medical devices using OCT. In the near future, we expect this thesis would be a breakthrough in finding new applications in real-world clinical study.

CHAPTER 2. Real-time OCT for advanced screening in surgery

2.1 Development of high-speed SS-OCT

As introduced in Chapter 1, FD-OCT has the advantage that image acquisition is faster than TD-OCT. Although the methods have similar levels of sensitivity, we have built SS-OCT, which is more advantageous in probe-type applications. High-speed SS-OCT imaging was performed using a swept source laser (Axsun Technologies Inc., USA) centered at 1,310nm center wavelength with sweep rate of 100kHz and bandwidth of 110nm. The infra-red light from swept source laser is delivered through optical fibers to minimize system size and increase mobility of OCT system during surgical procedures. The light then separated to two independent optical path through optical coupler (FC1310-70-50-APC, Thorlabs Inc., USA), which divides laser intensity equally. After then, separated lights propagate to focusing lens of sample arm and reference arm each. The reflected or back scattered lights are combined into another coupler, and generates optical fringe patterns through Mach-Zehnder interferometry. The fringe encodes depth information of sample into intensity and frequency of signal. To decode the optical signal, it is required to convert optical signal to computer configurable signal, such as digital or analog voltage signal. For signal conversion, high sensitive balanced photo-detector (PDB450C, Thorlabs, USA) is connected with two ends of coupler that works as Mach-Zehnder interferometry as shown in Figure 2-1. The balanced photodetector has switchable gain selector so that even small intensity of light signal can be amplified to analog voltage electrical signal. After signal conversion, the analog voltage is acquired through digitizer (ATS9350, Alazartech, CA) to differentiate high frequency information. The digitizer can acquire voltage signal at 500MS/s and the higher frequency it can acquire, the deeper information OCT can visualize.

Following to raw optical fringe signal acquisition, all the hardware control, signal processing and data saving procedure are completed. For high speed swept source OCT (SS-OCT), it is important to control iteration time that consumed during hardware control and signal processing properly. Hardware control contains signal acquisition, digital trigger, analog output and galvano mirror movement, and signal processing covers FFT of raw A-line signal, background noise subtraction, and signal windowing. If the hardware control time is longer than signal processing time, final image will be distorted according to time axis. Also, if signal processing time is longer than hardware control time, acquired

data cannot be fully utilized and overflow the memory. Therefore, high speed system requires accurate synchronization between entire hardware and software. For synchronization of hardware, we utilized trigger signal from laser source as a master trigger of whole connected hardware such as galvano-mirror, digitizer, and GPU. More details about synchronization will be delivered in next part. Through precise synchronization, we can acquire 100 OCT images in a second, and save entire 3D images by scanning galvano mirror. The optical resolution of our system is 10 μm for axial direction with 1024 pixels and 20 μm for lateral direction with the pixel number of B-mode. The final program for high speed SS-OCT system is shown in Figure 2-2 with the image of rabbit cornea for ex-vivo experimentation.

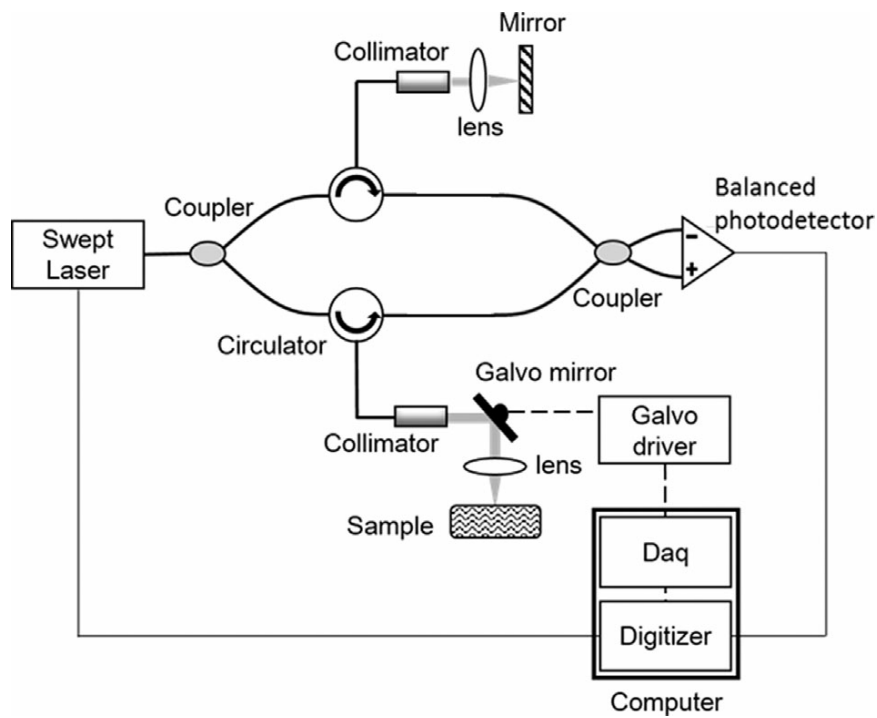


Figure 2-1. System schematics for high speed SS-OCT with Mach-Zehnder interferometry. Fiber based optical setup for SS-OCT with swept laser, coupler and circulator. Optical signal acquisition is completed through DAQ board and digitizer.

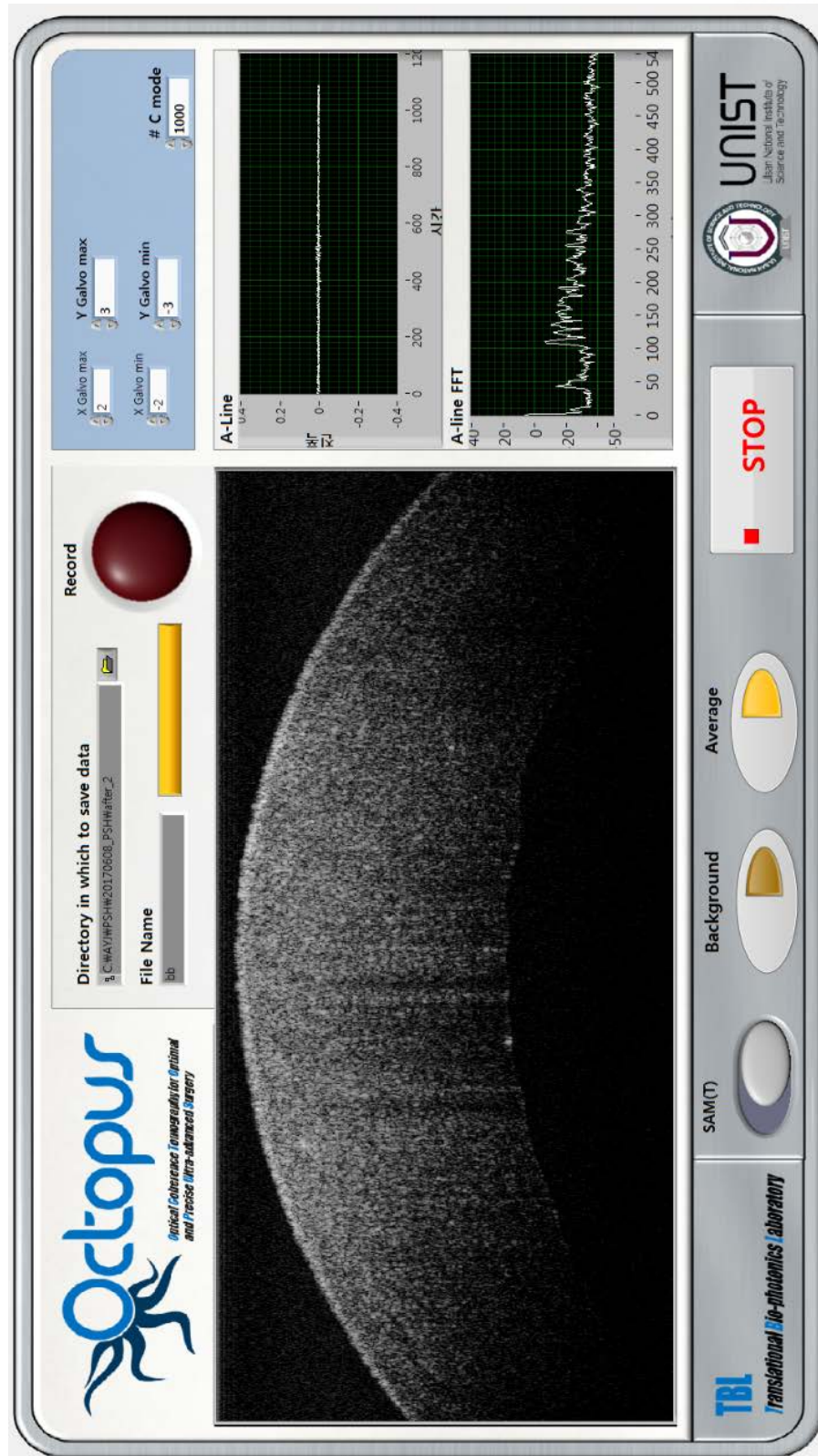


Figure 2-2. User Interface made by LabVIEW software for high speed SS-OCT. The user can control scanning range, number of sampling, file saving path raw A-line profiles and OCT images shown in single window.

2.2 Configuration of OCT software

For image acquisition through high speed SS-OCT, it is required to manage not only for hardware, but also consider computational power during signal processing. To match the speed of hardware control, we utilized sweep trigger from swept laser as the master trigger. The sweep trigger means speed of single sweep of chopped wavelength of 110nm broad band spectrum. We fully utilized the sweep trigger as 100 kHz to obtain 100 frame/s OCT image.

To synchronize system, firstly galvano mirror was controlled through analog output of DAQ (PCIe-6353, National Instruments, USA) with sweep trigger as sampling clock as shown in Figure 2-3. This scan nominates single axis scan for B-mode imaging of OCT. Previously we applied saw tooth shape of analog signal to the galvano mirror, but that signal shape causes damage to galvano mirror due to the rapid physical angle changes. Through the triangular shape of analog signal, we solved the problem and increase imaging speed by acquiring doubled data during increment and decrement of single triangular analog signal. Meanwhile, we also acquire optical signal, also called A-line profile, through balanced photodetector at each Galvano mirror position through digitizer. To acquire signal and control galvano mirror together, same sweep trigger was set as the starting trigger of acquisition and so as the k-clock of swept laser for sampling clock of digitizer as shown in Figure 2-4. After then, optical signals at each position of galvano mirror angle can be acquired through iterative acquisition loop.

With acquired A-line profile, we applied Henning window to reduce truncation of signal. Although performing an FFT on a signal can provide great insight in a short time, it has limitation in signal clarity of frequency domain due to imperfect repetitive pattern of raw signal. Windowing methods can reduce this distortion of result signal by making zero values at the ends of signal. Then the core signal processing part of the OCT system followed by transferring zero padded signal to the onboard memory of graphic processing unit (GPU) for high speed calculation as shown in Figure 2-5. A large amount of data which requires repetitive calculation can be processed faster by GPU rather than a sequential data processing method of the central processing unit (CPU). We utilized GPU as the GeForce GTX 760 (NVIDIA, Inc.) and applied the vertex and texture of the OpenGL API library of compute unified device architecture (CUDA) 5.5 [37-39].

After FFT process through GPU, cross section information of sample can be visualized with speckle noise and line noise. Although SS-OCT has high signal-to-noise ratio, optical property of scattered light generates lots of speckles in object image and interaction between optical components provides static noise in background. Through averaging continuous multiple images, we can reduce

speckle noise which distributed in random position. Also by recording background signals of reference arm only, we could remove static line noise through subtraction of recorded data. The clarified B-mode OCT images are saved through image save function of LabVIEW to 'jpeg' type of image with 8bit pixel size as shown in Figure 2-6. Most important thing during image save is moving another galvano mirror axis that is perpendicular to B-mode scanning axis. For normal 2-dimensional OCT image, single axis scanner is enough for single B-mode image. However, for 3-dimensional OCT image, it is essential to obtain multiple B-mode images of different position at orthogonal direction of cross-section axis. Within the image saving diagram, we additionally attached analog control function for moving Y-axis direction, also called C-mode, to generate 3-dimensional volumetric data.

The functions of signal acquisition, FFT through CUDA [40, 41], background subtraction and image save should have to be positioned in single processing loop so that all the procedures run single time in every loop. However, single iteration time of entire procedures could be increased if additional functions are implied with previous loop. To minimize the running time being lagged, we designed multi-thread loop of signal acquisition and signal processing through queue (Que) as shown in Figure 2-7. To prevent data bottlenecks in each thread, the Que methods was applied by reducing load of CPU with multi-core processors. The acquisition loop only contains digitizer acquisition function to obtain raw data and signal processing loop contains remained functions. To connect two independent acquisition loop and processing loop, we transferred acquired data through 'Write Que' function in acquisition loop to memory and extract data from memory through 'Read Que' function in processing loop. With this software architecture, we could acquire 100frame/s of B-mode images.

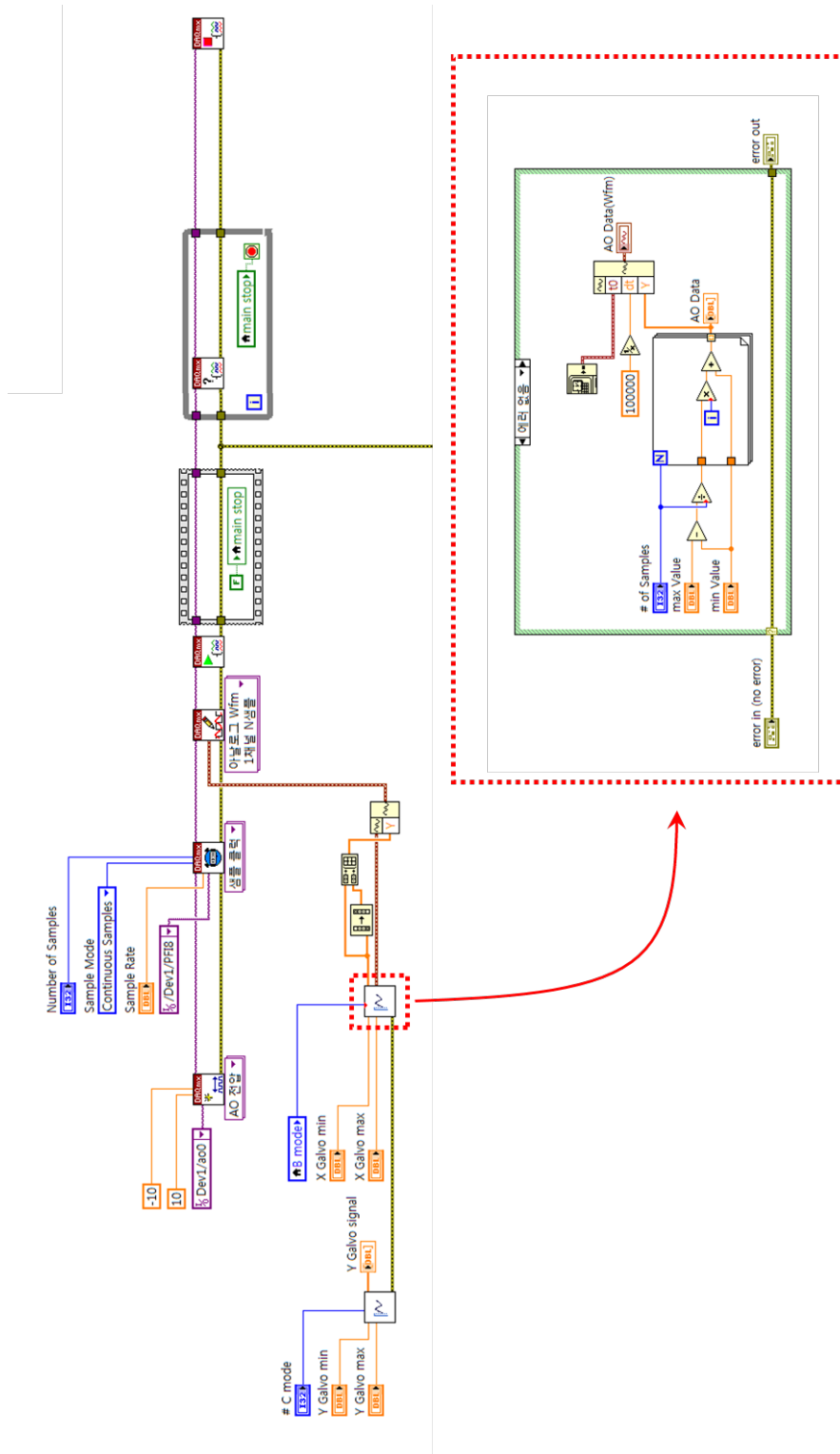


Figure 2-3. Block diagram of galvano mirror control. Through the DAQ and sweep trigger signal of swept laser source, galvano mirror is controlled with two perpendicular axis of x and y. To simplify the code, customized subVI for signal generation was applied (red box).

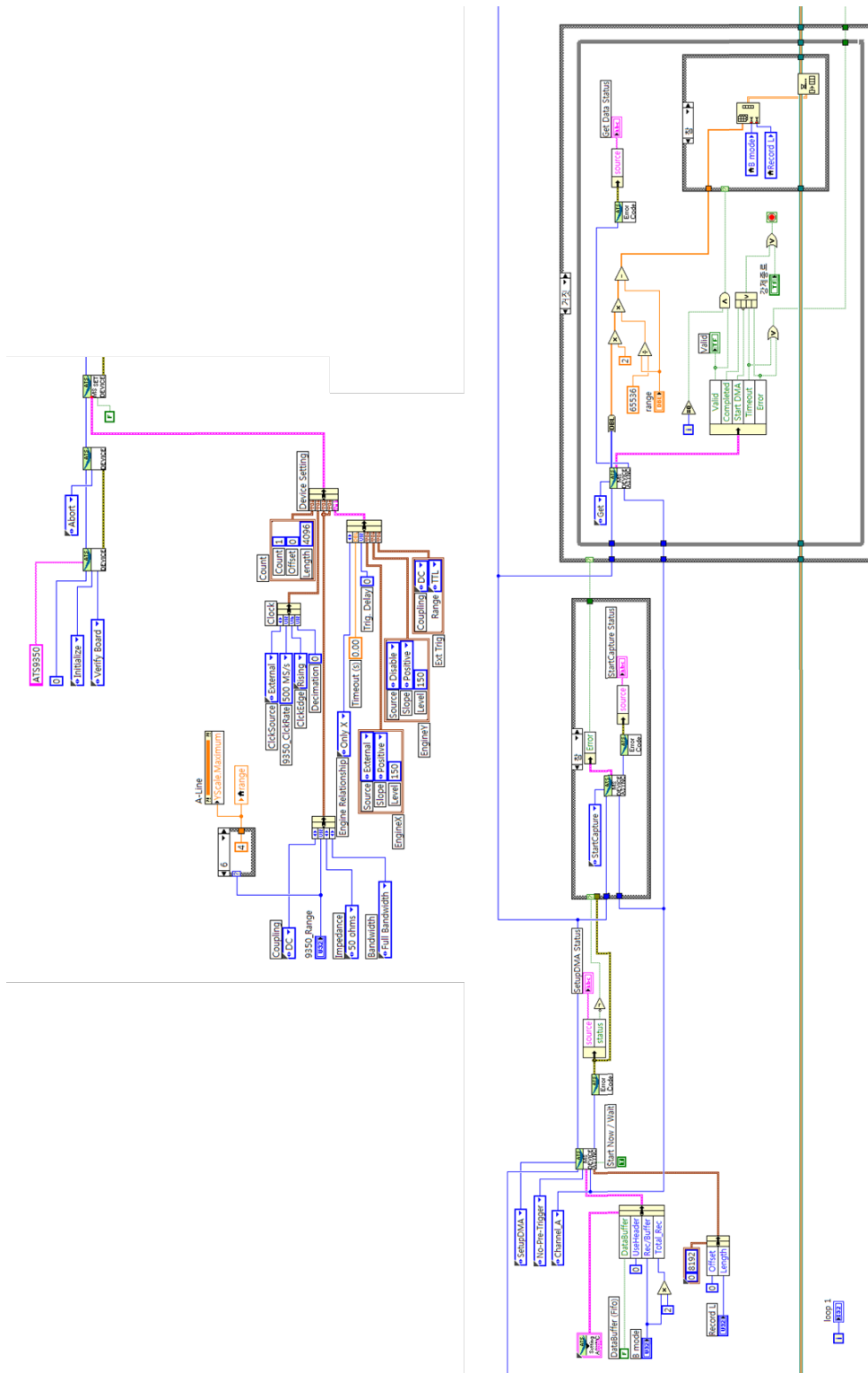


Figure 2-4. Block diagram of digitizer settings and raw signal acquisition. To synchronize digitizer, we applied external trigger and voltage level by independent setting values (top) and acquired raw optical signal data within acquisition loop (bottom).

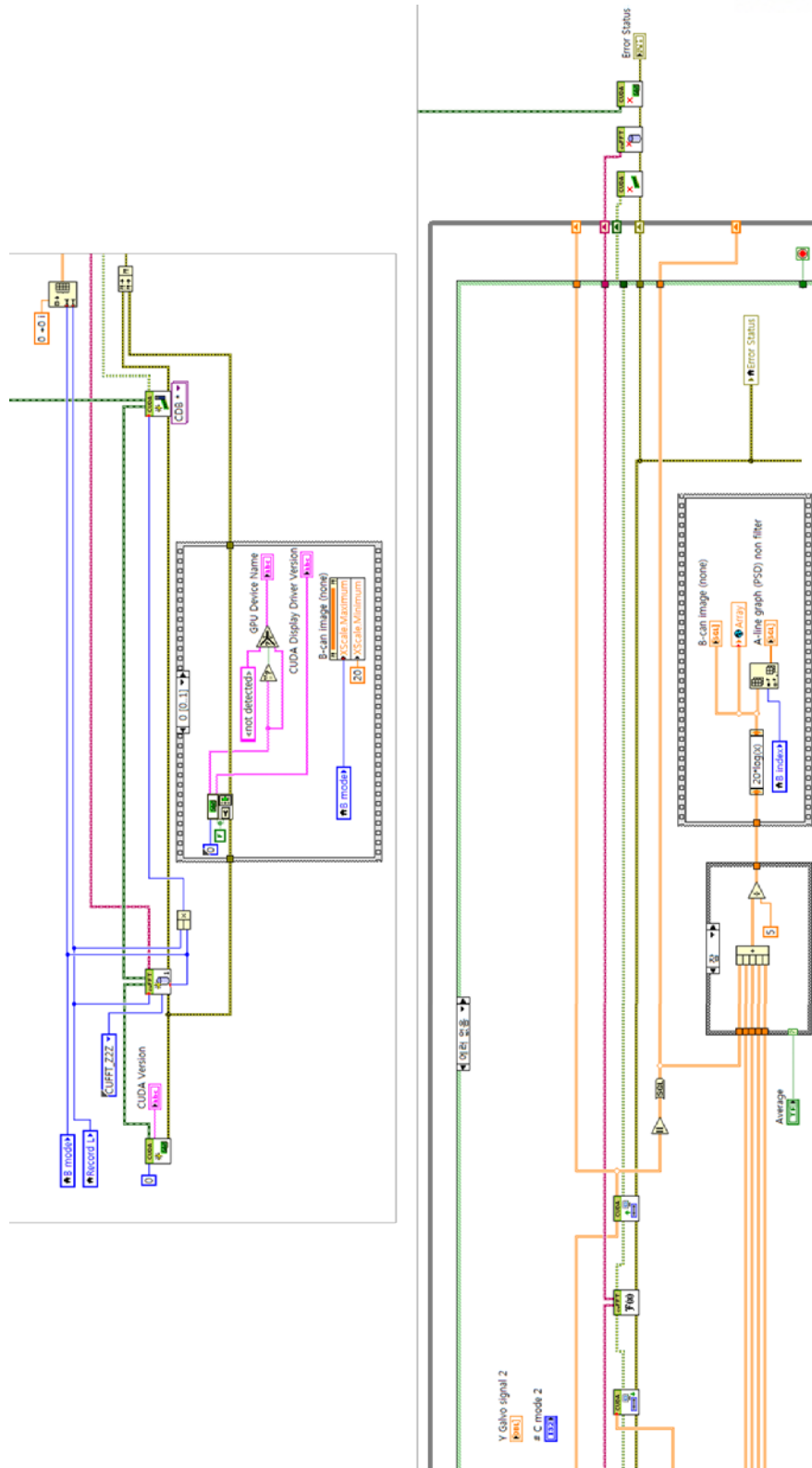


Figure 2-5. Block diagram of FFT signal processing through CUDA library for LabVIEW. To increase computational speed, GPU was installed into CUDA LabVIEW library for setting (top) and multi-dimensional FFT procedure (bottom).

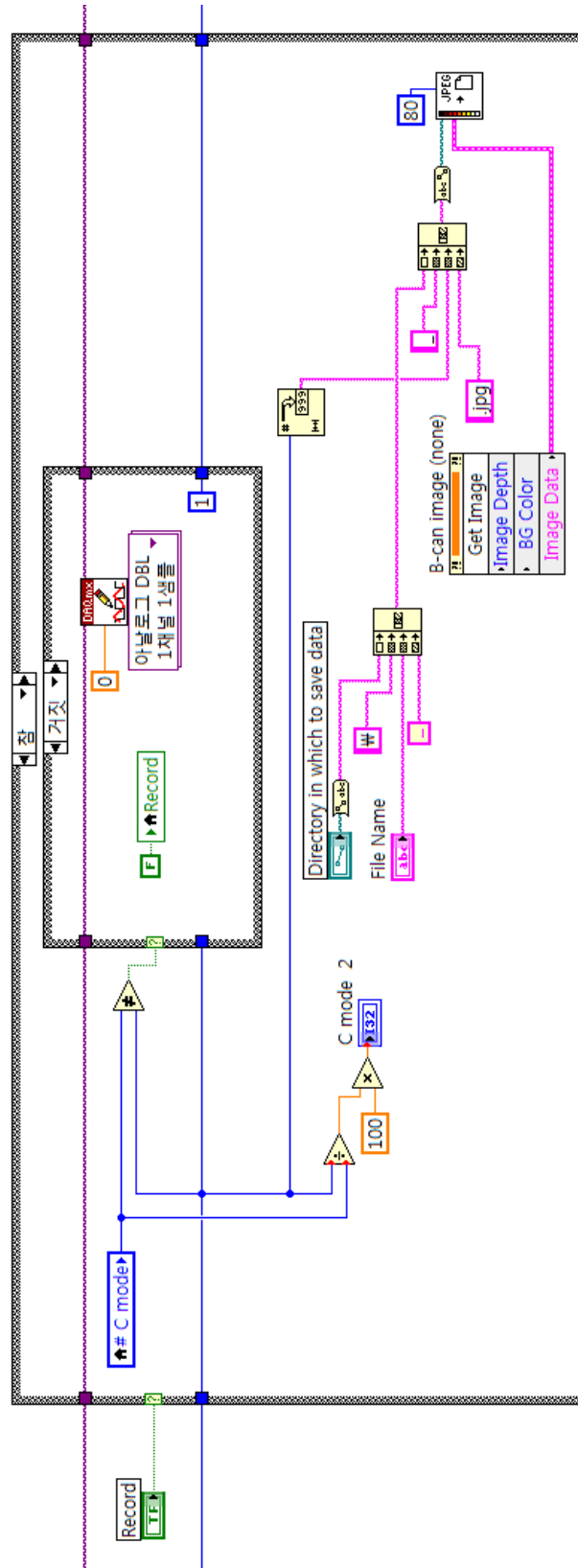


Figure 2-6. Block diagram of saving OCT image. After FFT through CUDA, B-mode OCT image is visualized in intensity chart and saved through image save function.

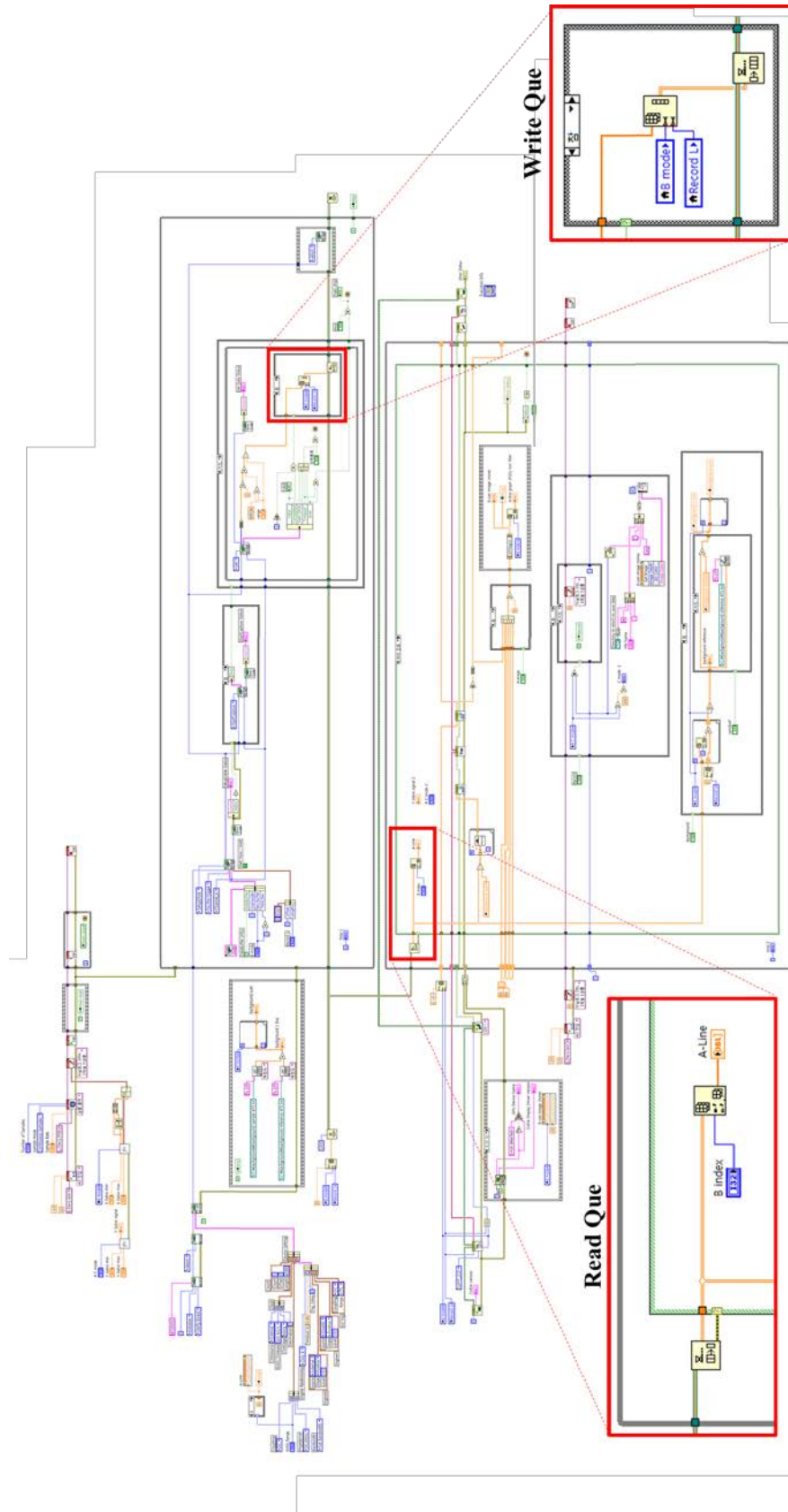


Figure 2-7. Block diagram of multi-thread through queue. For multi-thread parallel processing, queue functions are applied to separate acquisition and processing procedures.

2.3 Three-dimensional OCT visualization

For the study of surgical OCT, three-dimensional visualization of OCT data was developed. In the SS-OCT image acquisition presented in Section 2.2, three-dimensional OCT visualization can be operated mainly by matching the computational time of each software parts. Figure 2-8 represents programming flow chart for real-time 3D volumetric image processing. The flow chart can be roughly divided into three parts. First, data is transferred from a device memory (Digitizer's on-board memory) to a host memory (PC memory). A high-speed digitizer mounted in a PCIe (Peripheral Component Interconnect Express) slot transfers data to the device memory. This data is transferred to the host memory of the computer via the PCIe bus and acquired through a central processing unit (CPU). After then the signal processing of the data followed with the GPU which can process a large amount of volumetric data in parallel. Finally, the customized function library for three-dimensional volume rendering was implemented into LabVIEW software. Also, The development environment provided by NVIDIA for signal processing and image processing 3D imaging using texture analysis techniques, and perspective projection 3D imaging using optimal ray casting techniques.

An important consideration is that images are stacked in a volume buffer through a galvanometer 2-axis scan acquisition. The volume visualization speed is determined by the sweep rate of the swept source laser and the number of C-mode images. For example, the maximum volumetric rendering speed of 100 kHz sweep trigger light source used in our SS-OCT is ideally 10 volumes / second when it is obtained with 100 images each in width and height. In 12-bit and 1024 A-line acquisitions, the memory is transferred to a data throughput of about 200 MB / sec. However, ideal visualization speed will be maximized when the delay time for data processing is smaller than the time interval at which data is acquired. For real-time volume visualization, we customized own dynamic link library (dll) which can process three-dimensional rendering through interaction of GPU, CPU and memory. Figure 2-9 represents the dll implied LabVIEW block diagram with lots of variables for rendering. The variables contain scale factor, rotation angle, volume contrast and translation of each axis and it could be changed through simple mouse interface. If mouse buttons or position change, event structure in block diagram updates new variables of three-dimensional rendering.

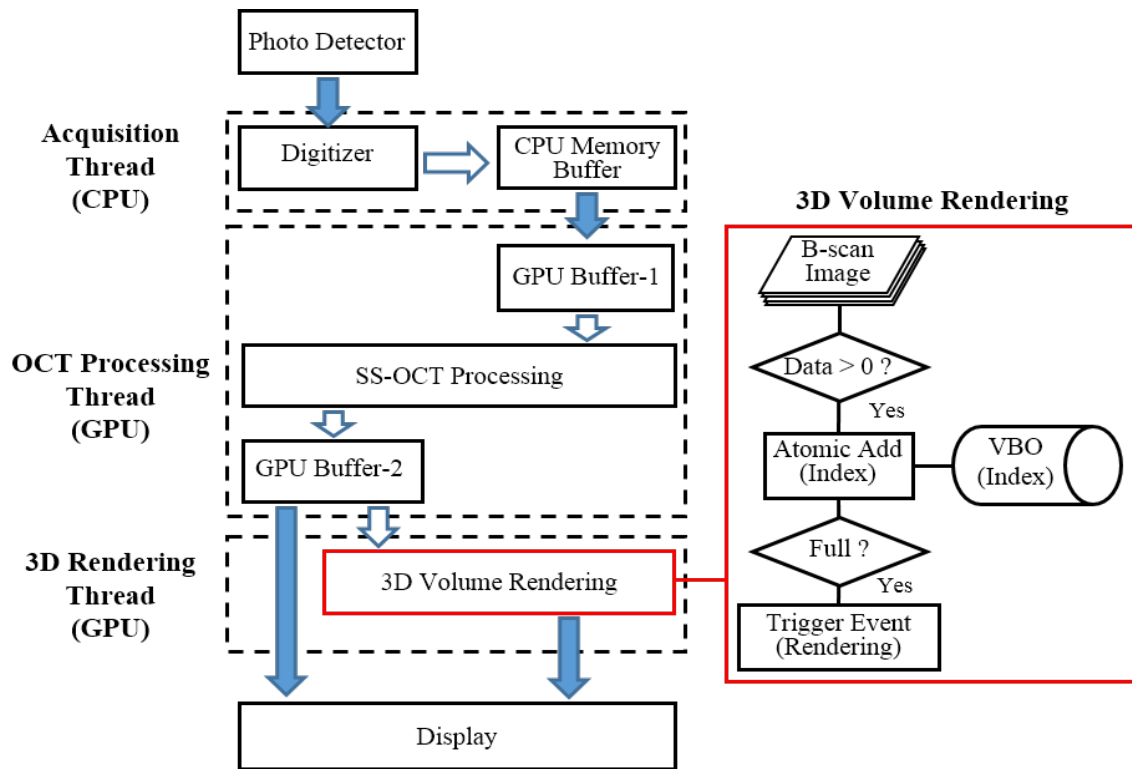


Figure 2-8. Signal processing flow chart of the multi thread structured GPU architecture for 3D visualization. Solid arrows, main data stream; Hollow arrows, internal data flow; Red box, flow chart of the 3D volume Rendering.

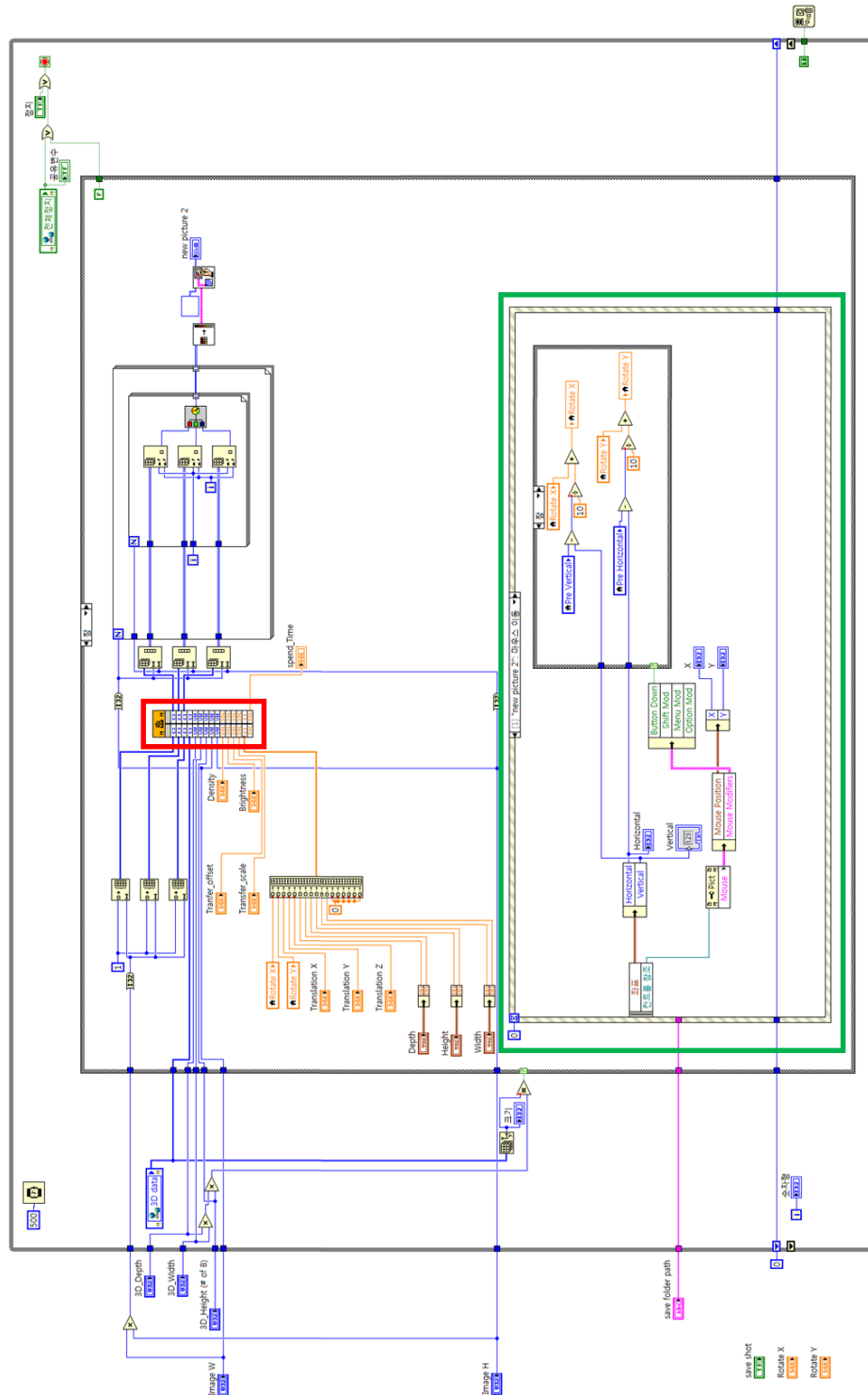


Figure 2-9. LabVIEW block diagram of the real-time 3D OCT image visualization. With the customized dll file (red box), real-time volume rendering can be obtained. The event structure enables 3D rendered object to be rotated, scaled, shifted by moving mouse (green box).

2.4 Clinical study for otolaryngology

2.4.1 Microscopic extrathyroidal extension

Papillary thyroid carcinoma (PTC) is the most common type of thyroid cancer [42-45], if the carcinoma has a size of 10 mm or more, it can be observed with ultrasound and the tissue is surgically removed by the head and neck surgeon [46-49]. Extrathyroidal extension (ETE) is defined as extension of a primary tumor outside the thyroid capsule or invasion of surrounding structures. Macroscopic or gross ETE to surrounding vital structures is categorized as T4 classification and is readily identified either via preoperative imaging studies such as, ultrasonography (US) and computed tomography or intraoperative inspection and palpation [50-52]. However, microscopic ETE (mETE) or minimal ETE (T3 classification) with no gross tumor extension may be difficult to distinguish [53]. Therefore, mETE is considered a factor in determining the extent of thyroidectomy, necessity of prophylactic central neck dissection, or postoperative radioactive iodine therapy. Imaging studies to identify ETE of patients with PTC has been limited to preoperative studies using US. However, the performance of US to identify ETE on the basis of contact of the tumor with the thyroid capsule is still limited with a sensitivity of 60–70% [54]. Moreover, these studies did not discriminate between mETE and gross or extensive ETE. Therefore, the accuracy of US to detect mETE may be even lower [55].

The intra-operative decision regarding extent of surgery, may be based on frozen section analysis to evaluate the presence of capsular invasion [56]. However, this has to be sent to the pathologist to wait for the results of the microscopic for tens of hours, resulting in delayed surgery and rising medical costs. So, we planned a study to identify mETE using intraoperative OCT. ETE imaging studies in thyroid cancer have not been reported yet, and this study suggests the feasibility of image evaluation to allow surgeons to make surgical decision.

2.4.2 OCT imaging to identify mETE

All animal procedures in this study were performed in accordance with institutional guidelines and the National Animal Care and Use Committee of the Kosin University of Medicine. Ex vivo OCT

images were obtained from 17 thyroid specimens removed from 17 patients who underwent thyroidectomy and were pathologically diagnosed as papillary thyroid carcinoma (PTC). Ultrasonography of all patients had a tumor in contact with the thyroid capsule and the radiologist interpreted it as "suspicious ETE" before surgery [57].

The OCT system was installed in the operating room, and the images were taken immediately after ablation of the thyroid specimen. 170 images of the tumor associated with the mass of the thyroid were taken (10 images in each sample were taken at different points with parallel displacements of the scanning axis). After imaging, the axes of the OCT scan are marked with two 26-gauge needles with no tumor invasion, and the histological image may represent a structure corresponding to the OCT image. All specimens were fixed with formalin solution and sent for histology.

Two thyroid surgeons who were familiar with ultrasound and histologic images of mETE randomly reviewed OCT images and did not see the final pathology report for each case. Tumors swollen into adjacent structures with no normal border of the thyroid tissue were considered to have enlarged membranes. The results of each test were matched with pathology reports to calculate sensitivity, specificity, positive predictive value, and negative predictive value. Cohens' k statistics were applied to confirm the inter-observer agreement [58]. The meaning of the k value is interpreted as follows. 0-0.2: slight agreement, 0.2-0.4: fair agreement, 0.4-0.6: moderate agreement, 0.6-0.8: substantial agreement, 0.8-1.0: almost complete agreement.

2.4.3 Result

Figure 2-10 shows the normal tissue of the thyroid as an OCT image [59]. The follicles in the parenchyma were characterized as spherical structural units with low signal density. Thyroid capsule was identified as dense structures at the high signal density including blood vessel, lymph and adipose tissue. Figure 2-11 shows intraglandular tumors located within the thyroid capsule, and OCT images represent tumors free of mETE at high signal intensity without destroying the continuous contours of the capsule. The images of OCT and histology indenting mETE are shown in Figure 2-12. In each of the images, the linear contour of the capsule is destroyed. Figure 2-13 also shows the visualization of three-dimensional OCT with both normal and tumor tissues.

Table 2-1 shows interpretation outcomes by two investigators [59]. Ten images were obtained from 17 thyroid specimens, and the investigators analyzed 170 images. The accuracy of mETE detection is 84.1% when compared to the pathology report.

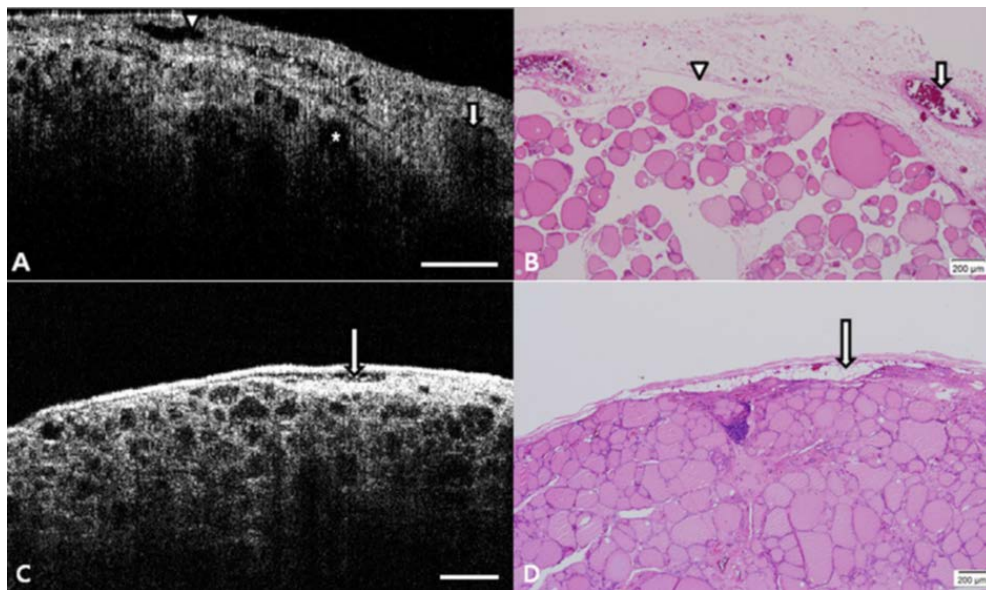


Figure 2-10. The OCT images and histologic images showing histological features of the normal thyroid gland [59]. White bar - 1mm, Arrow head - lymphatics, Short arrow - vessels, Asterisk - thyroid follicle, Long arrow - adipose tissue.

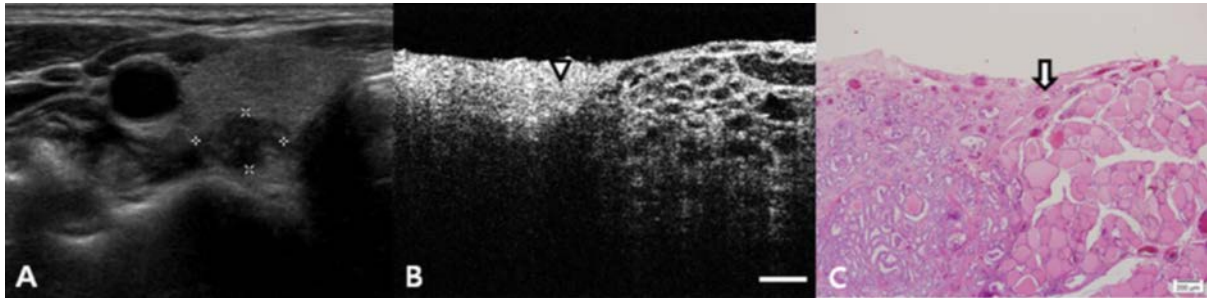


Figure 2-11. Comparison of ultrasound, OCT, and histologic images of thyroid cancer tissue with no ETE [59]. Arrow head and short arrow indicate confined thyroid tumor within the capsule.

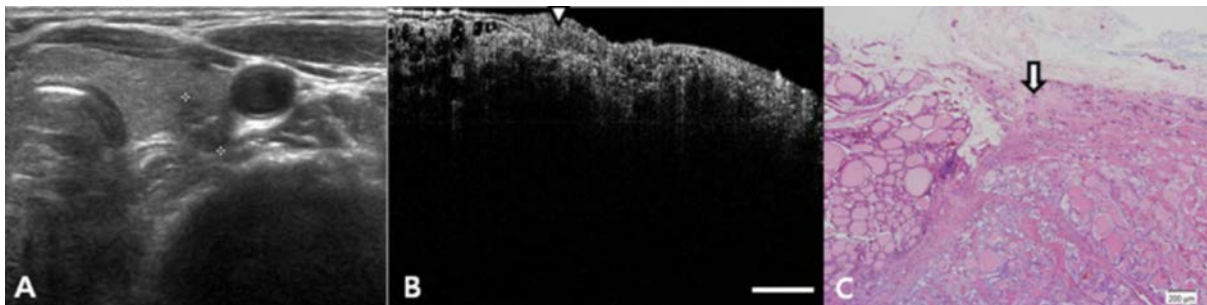


Figure 2-12. Comparison of ultrasound, OCT, and histologic images of thyroid cancer tissue demonstrates minimal ETE (arrow head and short arrow) [59].

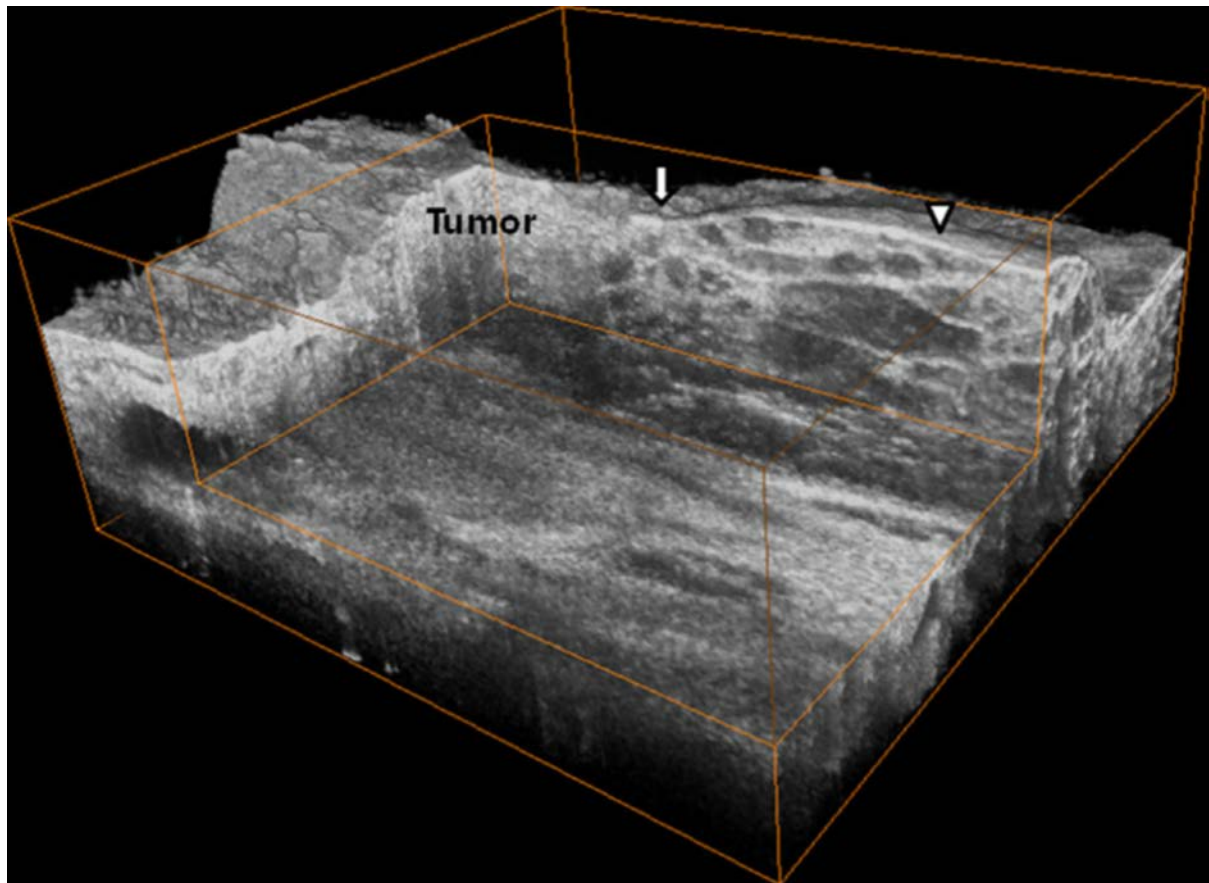


Figure 2-13. 3D OCT image of papillary thyroid cancer acquired from one patient with no mETE. The tumor was identified to be surrounded by capsule with normal tissue (arrow head and short arrow) [59].

Investigator 1 (Investigator 2)	Pathology report		
	No mETE	mETE	Total
No mETE	86 (87)	13 (12)	100 (100)
mETE	14 (13)	57 (58)	70 (70)
Total	100	70	170

Table 2-1. The interpretation result from two investigators. OCT images were evaluated to identify mETE. The accuracy of mETE detection was 84.1% and 85.3% for two inspectors [59].

2.5 Conclusions

A high-speed SS-OCT with a center wavelength of 1310 nm has been developed and confirmed to provide stable performance. It employs sweep triggers at 100 kHz from sweep laser sources, synchronization of high-speed digitizers and scanning mirrors, and parallel structure programming to reduce bottlenecks in the computer. In addition, LabVIEW software using GPU for visualization of 3-dimensional OCT was additionally applied, and the system was able to observe volumetric information. It introduced 3D imaging using texture processing technology and 3D projection optimized ray casting technology with perspective projection, and considered that acquired data with two axes scanned mirror was converted to stacked image in volume buffer.

The developed system was used to identify mETE in otolaryngologic surgery of patients with PTC. The histology of frozen section biopsy and the real-time OCT images of patients with thyroid cancer requiring thyroidectomy were compared and the feasibility was shown with 84.1% accuracy.

CHAPTER 3. Smart surgical microscope

3.1 Microscope integrated OCT

Surgical microscopes are becoming an essential tool in microsurgery because they can be observed with a high magnification surface image in a small field of view [60]. The medical field where microsurgery is often performed includes neurosurgery, ophthalmology, and otorhinolaryngology. Surgical microscopes widely used for over 20 years, have been limited in microsurgery because they provide only surface images of tissues. This may lead to irrecoverable damage to other neighboring tissues during microsurgery, and additional imaging devices such as magnetic resonance imaging (MRI) and computed tomography (CT) are definitely required to observe the underlying tissue during surgery. Common imaging devices used in such microsurgery are limited in their ability to respond flexibly to emergencies occurring in real time, such as bleeding during surgery or fine tissue changes [61].

To overcome these shortcomings addressed over a decade, a variety of microsurgical methods have been proposed. For example, assistive surgery using a fluorescent contrast agent [62-64] and a surgical navigator has been used [65].

Indocyanine green (ICG), a commonly used as a typical fluorescent contrast agent, has the advantage of distinguishing it from normal tissue by staining only a specific tissue such as a tumor. However, it is also has limitation in that patient has to be dosed depending on their current health, weight, allergic to chemicals. It can affect other parts of the body and cause additional diseases. Various surgical image guiding devices have been developed to improve the issues mentioned above by using pre-diagnostic imaging methods such as MRI, and surgical navigation devices are gaining popularity as the most representative out of them.

The surgical navigation system provides relatively more accurate anatomical information. Their main function is to allow the tumor margin to be tracked in real time during surgery. It enables the incision to be made while minimizing the loss of normal tissue. Although the surgical navigation system is applicable to relatively large tissues because of its large field of view, but it has a disadvantage in that it is difficult to apply to micro tissues.

Recently, a surgical microscope integrated optical coherence tomography (OCT) system, referred as MI-OCT, has been introduced and many related studies were conducted [21-23]. The OCT system is an imaging device that provides tomographic information of tissue in real time at a resolution up to 1 μm using interference phenomenon of near-infrared wavelength (800 nm ~ 1550 nm) light.

The OCT system has the advantage of viewing microstructures in real time with high resolution images, but due to the inherent light scattering in bio-sample, there is a limitation in depth penetration. Particularly, it is widely regarded as essential equipment in ophthalmology which treats eye with good light transmittance and provide detailed visualization of eye structure hardly explored with previous imaging modalities. In recent years, however, many research groups and companies have tried to collaborate to develop OCT as a medical device that acts as an imaging device during microsurgery.

Figure 3-1 shows the medical imaging systems of Carl Zeiss, a global provider of OCT manufacturer and surgical microscopes. Figure 3-1(A) shows a typical ophthalmologic OCT system, which is currently being used most actively in ophthalmology. Figure 3-1(B) shows the intraoperative OCT system, which can be diagnosed separately in the operating room beside the surgical microscope. Figure 3-1(C) shows a combination of a surgical microscope and OCT, which is called MI-OCT. These products are designed for use only in ophthalmic surgery of the retina. However, its utility is still limited when it requires specialized operations such as otolaryngology, neurosurgery and require other operations, which are specialized only diagnosis in ophthalmic retinal surgery. To overcome the limitations of the combined surgical microscope and OCT, we propose the smart surgical microscope that can be used in the therapeutic field as well as the diagnostic. We expect it to be a universal medical device that can provide real-time image guidance during surgery.



Figure 3-1. Various medical imaging systems of Carl Zeiss. (a) A typical ophthalmic OCT system currently being used most actively in ophthalmology. (b) An intraoperative OCT system that can be diagnosed separately in the operating room next to the surgical microscope. (c) Combination of OCT with a surgical microscope called MI-OCT.

3.2 Design for smart surgical microscope

3.2.1 Advanced methods for OCT and microscope integration

The OCT system uses the near-infra-red light bandwidth from the 800 to 1310 nm in general. In the shortest wavelength of 800 nm band, due to the characteristic of short wavelength, scattering of light in relatively biological tissue including such aqueous component becomes high. Though high axial resolution image can be obtained due to relatively shorter wavelength, the corresponding penetration depth is shallow. For the eye, highly transparent bio specimen, the 800 nm light source is widely being used in medical fields such as ophthalmology. In the 1310 nm band, the resolution is low, but due to long range of light bandwidth, the image can be acquired from even deeper position. This range of light source can be applied to a medical department such as a dermatology in which the thickness and opaqueness of specimen is relatively thicker compared to other types of tissue.

In this study, we developed a home-built high-speed swept source OCT (SS-OCT), which is specially designed to increase the image acquisition speed as introduced in Chapter 2. The main advantage of using a tunable wavelength of 1310 nm is to make deep penetration in bio tissue. This can be represented as a bifunctional medical device capable of providing a separate diagnostic image. Figure 3-2 below shows the entire configuration of the OCT system that diagnoses the current stage of the targeted skin.

Figure 3-3 shows a 3D CAD (Solidworks 2014, Dassault Systems) design that make it possible to proceed the image acquisition in OCT sample arm with the surgical microscope. One of the main component in the image acquisition part is a collimator (Thorlabs, Inc.) for the purpose of producing parallel light, a galvanometer scanner (Thorlabs, Inc.) for two-dimensional or three-dimensional imaging, a focus lens (Thorlabs, Inc.), a Dichroic mirror (Edmund Optics, Inc.), and an adapter for coupling with a surgical microscope, respectively. A lens with a focal length of 150 mm or longer was used to solve the limitation of the surgical working distance. To obtain three dimensional OCT image at the same position where top view of the surgical microscope is also displaying, a lens having a focal length of 200 mm and a diameter of 2 inches were used.

One of the beam passing through the lens travels in the direction to the sample by the dichroic mirror to acquire the light reflected from the tissue, and the resultant image is displayed as a two or three dimensional image. Three-dimensional CAD is designed to remove disturbance of any fine movement in optical system. It is manufactured for safe and practical use through astel-acrylic processing and painting considering the weight when attaching to a real surgical microscope.

The overall schematic of the developed MI-OCT system is shown in Figure 3-4. It can be explained into three major parts, a microscope image acquisition (visible light), an augmented reality implementation (beam projector), and an image acquisition part of the OCT (near-infrared light).

First, the visible light part was fabricated using a surgical microscope (OPMI pico, Carl Zeiss, Inc.), which is widely used in the actual operating room. The surface image of the sample passed through the eyepiece was divided by a beam splitter mounted on a surgical microscope, and the surface image was collected at camera for surgical image storage.

Next, the augmented reality part projects the tomographic image acquired from the image acquisition part of the OCT to a 640 x 480 resolution beam projector (SmartBeam, SK Telecom, Inc.), and uses a beam splitter in ocular lens of eyepiece. The high - resolution OCT was implemented so that it could be combined with the surface image provided by the surgical microscope through the right ocular lens among the two ocular eyepieces. Also, by inserting an ND filter (Neutral-Density Filter, Thorlabs, Inc.) between the beam projector and the beam splitter, it is possible to optimize the brightness of the tomographic image without overexposure to the reflected light.

Finally, the near-infrared light used in OCT shares the surface path of the microscope and is separated by a dichroic mirror (Edmund Optics, Inc.) so that it can proceed to the OCT-only optical path. The dichroic mirror used in this optical system is a type of optical filter that passes or reflects light of a specific wavelength. In this paper, the light in the near-infrared region is reflected at the incident angle of light is 45 ° with a mirror having a feature of allowing the light beam to pass through.

Our completed MI-OCT which can be called a smart surgical microscope is shown in Figure 3-5. The system will continue to improve optical and electronic components to improve performance. It is also easily integrated with additional medical devices sharing light source of the OCT. And it has systematical stability and convenience so that it can be used immediately in ongoing animal experiments and clinical studies. Figure 3-6 shows the results for evaluating the performance of our smart surgical microscope. We could confirm that the augmented reality was realized by combining the microscopic image and the volumetric image of OCT.

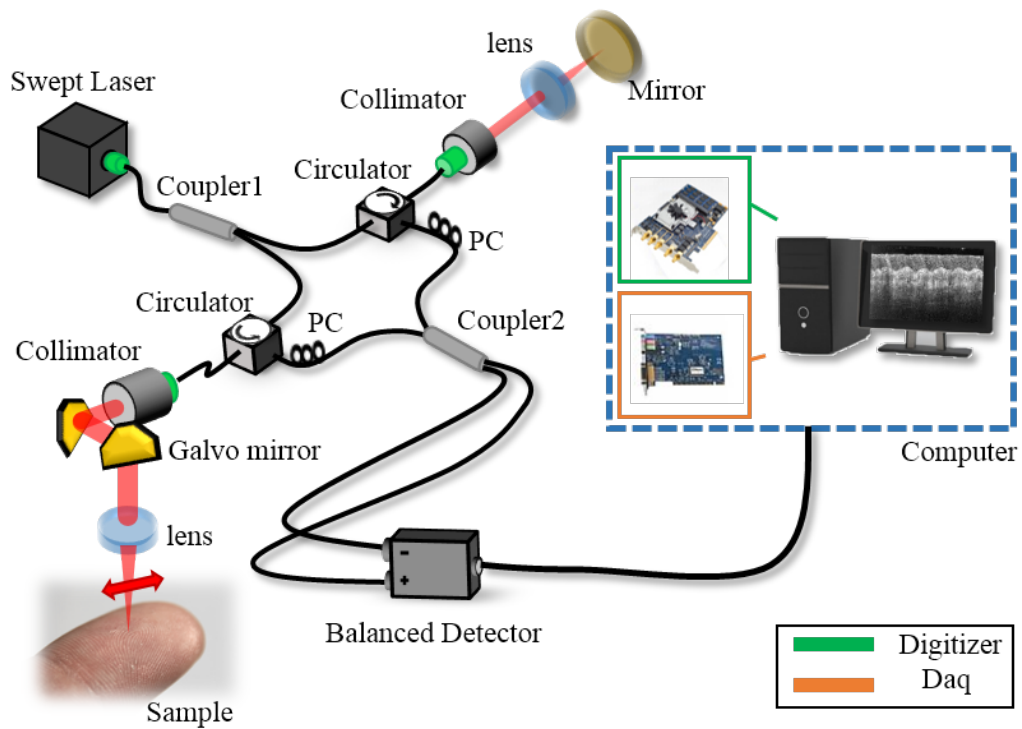


Figure 3-2. Configuration of SS-OCT system. The voltage signal from the balanced detector is collected through the digitizer, and the Daq board is synchronized with the clock signal from the swept laser source to control the galvanometer scanner. *PC: Polarization Controller.

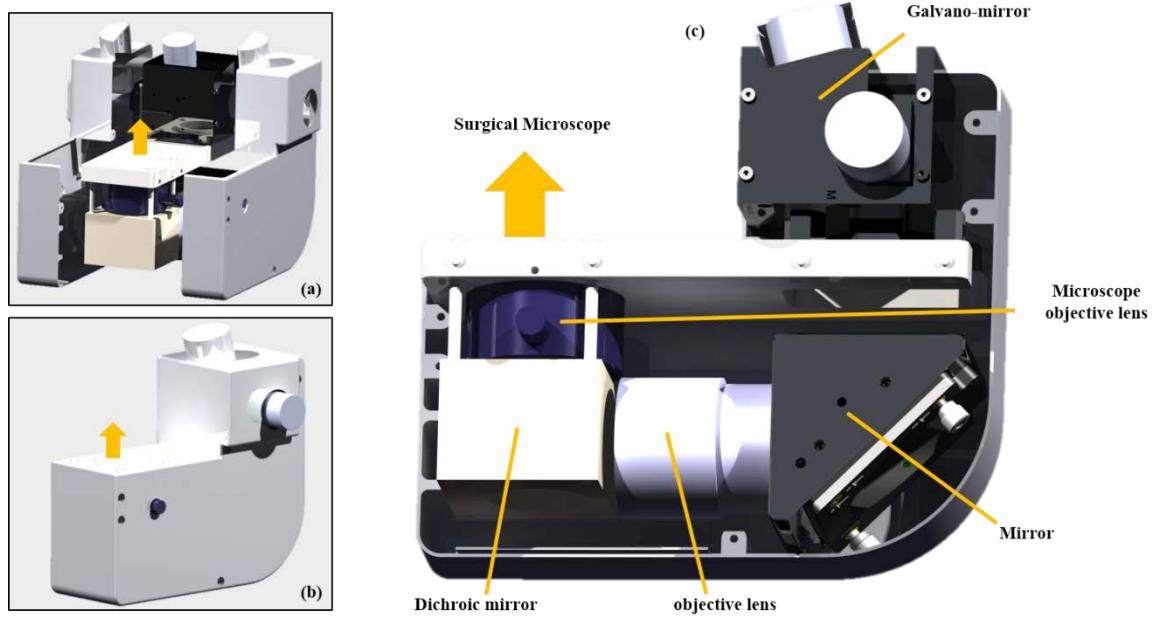


Figure 3-3. Schematics of 3D CAD design for OCT sample arm with the surgical microscope. (a) 3D model drawings of the hardware components. (b) Assembled design. (c) Schematic of the optical components in the hardware. Optical part consisting of the galvano-mirror, surgical microscope, microscope objective lens, mirror, objective lens, dichroic mirror are designed to attached to the surgical microscope system.

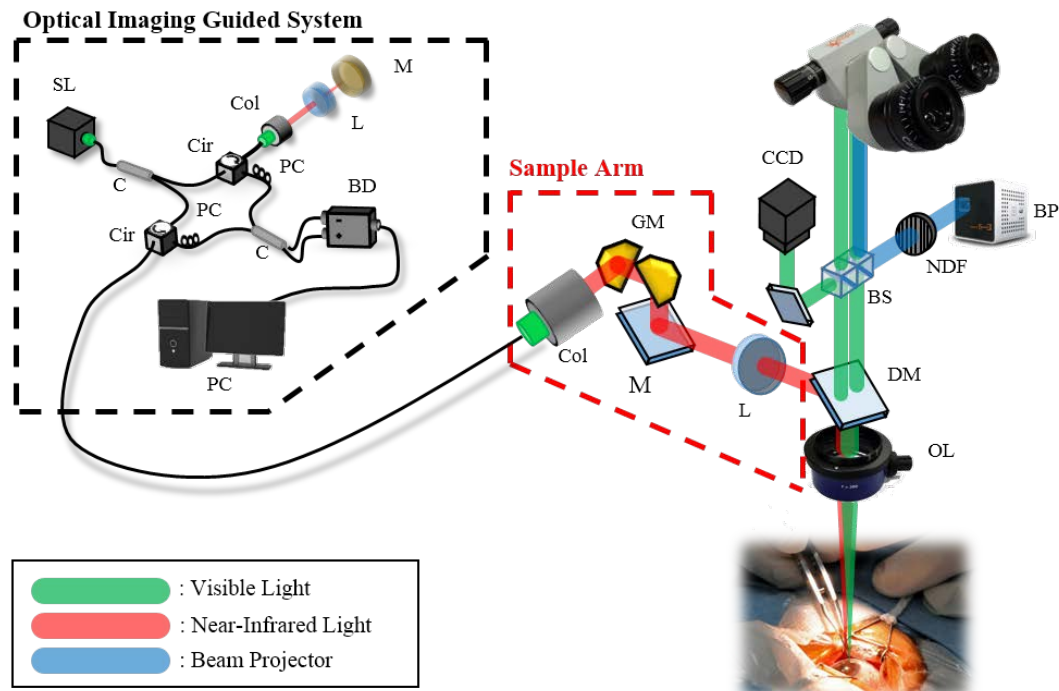


Figure 3-4. Configuration of MI-OCT system. Swept- source Laser (SL), Coupler (C), Circulator (Cir), Collimator (Col), L (Lens), Mirror (M), Polarization Controller (PC), Balanced Detector (BD),and PC. Sample Arm attached microscope includes Collimator, Galvano-Mirror (GM), Lens, Beam Splitter (BS), Dichromatic Mirror (DM), Beam projector (BP), ND-filter (NDF).

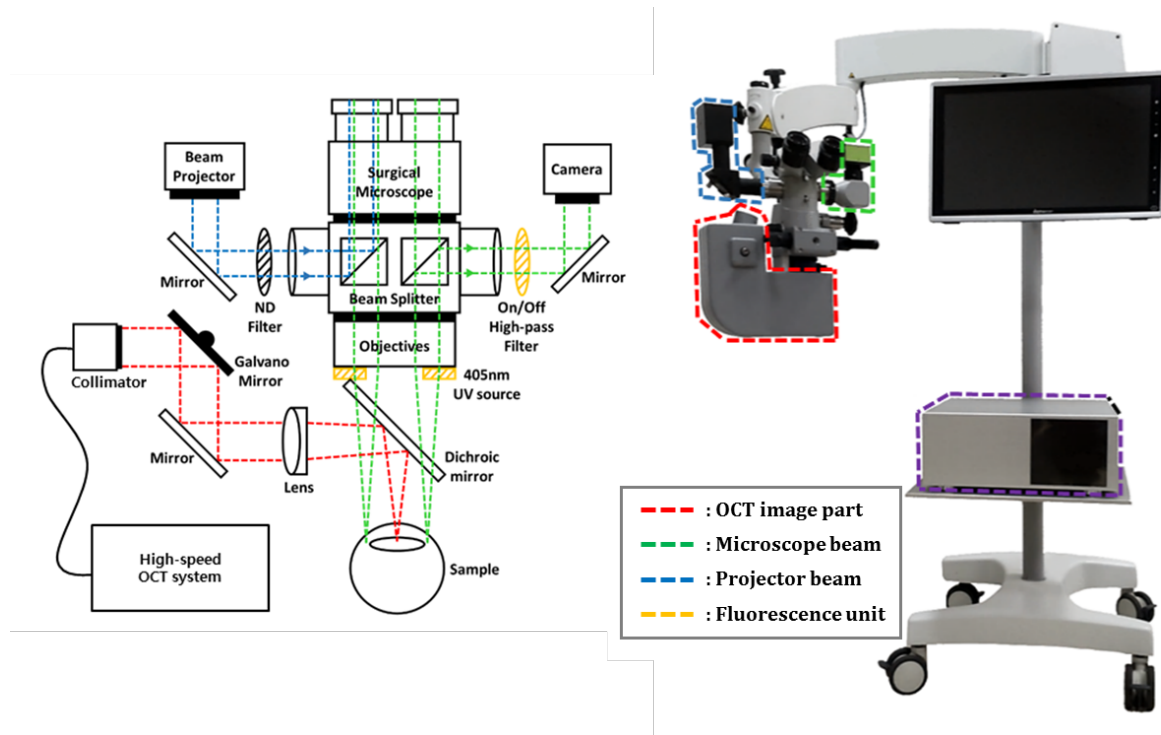


Figure 3-5. Completed MI-OCT system which can be called a smart surgical microscope. It is easily integrated with additional medical devices sharing light source of the OCT.

3.2.2 Augmented-reality imaging under smart surgical microscope

The outcome of the developed smart surgical microscope is shown in Figure 3-6 below. To evaluate the performance of the system, we captured a microscopic image in the eyepiece view of the surgical microscope. In addition, 3D OCT images were simultaneously visualized and overlaid on eyepieces using a beam project. This result confirms that our smart surgical microscopes can provide depth information that was not available in the existing *en-face* view.

We have implemented augmented-reality technology in medical devices and this system will have the potential to be applied in various branches as well as in ophthalmology through clinical studies. It is also expected that it will evolve from new volumetric information to new medical technology.

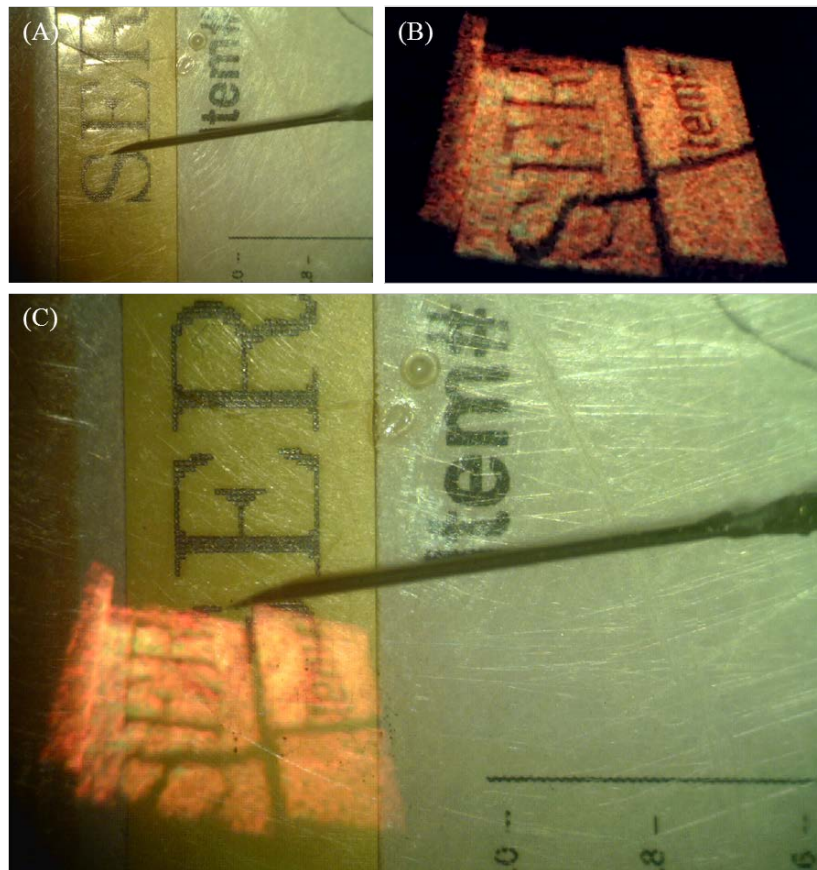


Figure 3-6. Augmented-reality image from smart surgical microscope. (A) Microscopic image in the eyepiece of the surgical microscope. (B) 3D OCT image acquired from high-speed SS-OCT. (C) Scene captured from the eyepiece view that overlays the OCT image on the microscopic image using a beam projector.

3.3 Conclusions

This chapter introduced smart surgical microscope. To develop the system, a microscope combined with OCT was designed, and an advanced method was proposed for MI-OCT, which can be called a smart surgical microscope. The OCT system is capable of viewing microstructures in real time with high resolution images and providing 3D images with volumetric information. In order to integrate surgical microscope and OCT system, we have implemented the augmented reality using optical filter based small beam projector, so that microscopic and tomographic image of the specific surgical site can be provided at high resolution in the eyepiece in real-time. The double complement information provided by the cross-sectional images from OCT and combined surgical microscope is expected to deliver comprehensive information to the surgeon. Surgical microscopes are widely used in most surgical procedures. It will be a medical device that will allow each advantage to be retained through the combination with the OCT and provide new medical technology in the hospital.

CHAPTER 4. Novel microsurgical instruments

4.1 Intro: Optical coherence domain reflectometry

The OCT system, a technology that is mainly dealt with in this study, is based on optical coherence domain reflectometry (OCDR) [66, 67] among various type of low coherence interferometry (LCI). Therefore, the OCDR requires an understanding of the interferometric principle, and this basic technique provides a few micrometers axial resolution and around 2 mm imaging depth by implementing the coherence theory. OCDR is used when measuring depth information for a point at high resolution. In general, OCT can be understood as acquiring an image through the transverse scanning of the sample stage with OCDR technology. Therefore, the basic mechanism of OCDR can be easily understood as a single A-mode in OCT while the OCT is performing the transverse scanning of multiple A-mode.

4.2 Smart surgical forceps

Generalized microsurgery requires the incision and fixation of microstructures within 1 to several tens of micrometers, and the completeness of the operation is differentiated according to the skill of the operator. One of the major factors affecting microsurgery is the operator's hand tremor, which usually requires motion compensation of several tens to several hundreds of micrometers and a maximum frequency of 5 to 15 Hz [68, 69].

In this chapter, we propose a motion-compensable instrument for the stabilized depth direction using the OCDR technique introduced in Section 4.1 above. In this study, we introduce intelligent forceps and presented a low-cost surgical forceps using single mode fiber [70-74].

However, it has disadvantages in that the characteristics of the signal are changed according to the inclined angle from the surface, which is disadvantageous in use in micro-surgery. To solve these drawbacks, we fabricated a fiber optic probe in the form of a ball lens with a relatively long focal length.

Also, it is possible to minimize the error range based on the optical simulation, so that it can be implemented more quickly in actual production and it can reduce trial and error of the manufacturing process.

Probe design and fabrication

Figure 4-1 shows the simulation results of a fiber optic probe for Gaussian beam analysis using ABCD Matrix [75]. The ABCD Matrix formula is used in a wide variety of optical fields as a way of expressing the change of light characteristics due to the nature of light as it passes through optical components. As a result of the simulation, as the curvature of the ball lens and the focal length are proportional to each other, the larger the curvature of the ball lens is, the longer the focal length is, and the usability is greatly improved. Because of this, the accuracy of the hand tremor compensation is reduced, and the distance from the tissue is not kept constant, so this optical simulation is very important. As a result of the simulation for selecting parameters suitable for vibration compensation, the curvature of the ball lens was set at 100 μm . The ball-lens-type optical fiber probe is designed to have a long focal length of about 600 μm and a lateral resolution of about 18 μm .

Figure 4-2 shows the fabrication process of a fiber optic probe [76-78]. Considering the characteristics of single mode fiber (SMF) and coreless silica fiber (CSF) to produce lensed fiber, a ball lens was produced by applying an arc discharge to the end of the fiber with two fibers. In order to optimize the beam size and focal length in the fabrication process, we simulated Matlab 2012 (MathWorks Inc.) and implemented the optimum beam diameter and focal distance through experiments to adjust the CSF length and curvature of the optical fiber end. Figure 4-2(a) shows the process of fabricating SMF and SCF with ball lens by arc discharge effect. It has the advantage of minimizing the coupling resistance of the optical fiber, but it is easy to manufacture. In Figure 4-2(d), the signal intensity of the ball lens is compared with that of the flat fiber, and the ball lens is focused at the focal length. It is also known that the ball lens has excellent tilting characteristics, and it can be seen that the signal is well measured even if it is tilted more than 5 degrees.

Smart surgical forceps using lensed fiber and piezo motor

The ball lens type optical fiber described above has the advantage of minimizing the insertion loss

because the focal length can be formed without using an optical component such as a gradient index (GRIN) lens at the end. The fabricated fiber optic probe can be used as a sensor to measure the distance to the surface, and it is used to make intelligent micro-forceps.

A constant distance from the surface was maintained by using a piezo actuator (LL1011A, PiezoMotor, Inc.) capable of high-speed and precise control as shown in Table 4-1 inside the manufactured forceps. It not only compensates the operator's hand tremor but also reduces the patient's motion artifact, thus allowing stable operation.

Figure 4-3 shows the schematic of smart surgical forceps. The intelligent forceps consist of a piezo actuator used for motion compensation, a case designed to protect against external influences, and a fiber optic probe for distance measurement. The handle was cut from the most widely used surgical micro-forceps (Alcon, Inc.) and the body part of the case was made of a die design. The body of the piezo actuator was fixed to the case and its shaft was connected to the handle of the forceps. The input signal is converted into a distance according to the previously measured value and applied as a desired value of actuator control.

The solid-work modeling of the intelligent forceps for hand tremor compensation and the actual device developed are shown in Figure 4-4. To evaluate the performance of the intelligent forceps on the hand tremor, as shown in Figure 4-5(a), it was mounted on a micro-stage. In order to adjust the distance from the sample, a two-axis micro-stage was constructed so that the forceps could be changed in the vertical and horizontal directions. Figure 4-5(b) shows the inside of the control system to interface with the forceps and detect the signal of the fiber probe. The sample arm of the OCT system introduced in Section 2-1 was replaced with a lensed fiber, and the measured signal implements the control of the piezo actuator with distance feedback-based control in the computer. Figure 4-5(c) shows the feasibility of the intelligent forceps. The performance of the developed forceps is shown in the graph as an indicator of error and root mean square value. There is a position error from 100 μm to 600 μm (RMS: 202.92) in the free hand interval (0 ~ 20 sec) without compensating the hand tremor. However, the error decreased to less than 10 μm (RMS: 9.01) in the compensated motion interval (20 ~ 40 sec). Figure 4-5(d) shows the frequency analysis before and after compensation for the error value for hand tremor through FFT calculation. In the main hand tremor frequency range of 5 ~ 15Hz, it is about 72.4dB before compensation and about 53.6dB after compensation. Through this verification, it was confirmed that the position control performance of the developed intelligent forceps is stable, and it is suggested that the human hand tremor frequency of 5 ~ 15 Hz region can be sufficiently compensated during actual operation.

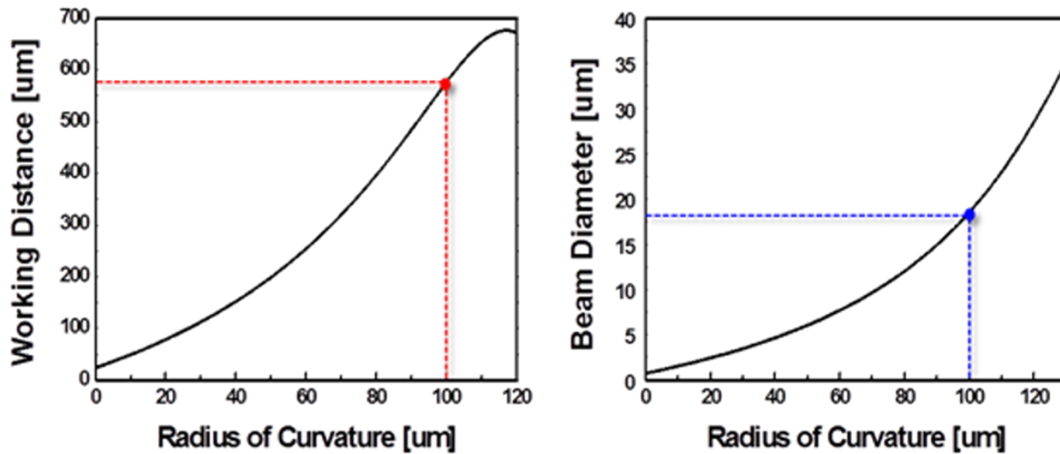
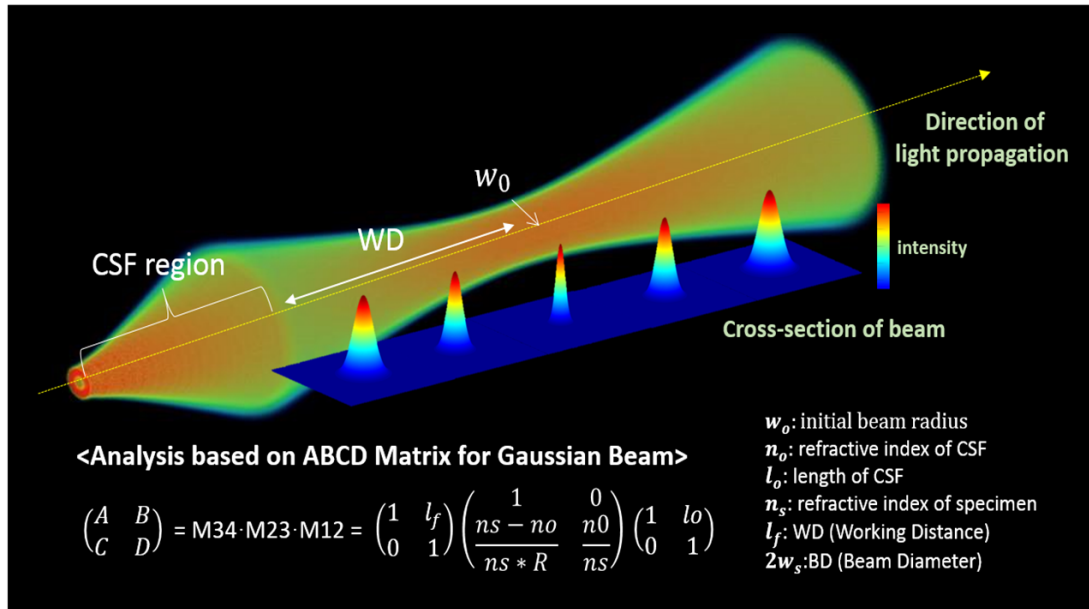


Figure 4-1. Simulation of the lensed fiber with general equation. (a) Equations of the general ABCD matrix ray transform matrix and working distance and beam diameter. (b) Simulation result of the working distance, (c) beam diameter according to variation of the radius of curvature.

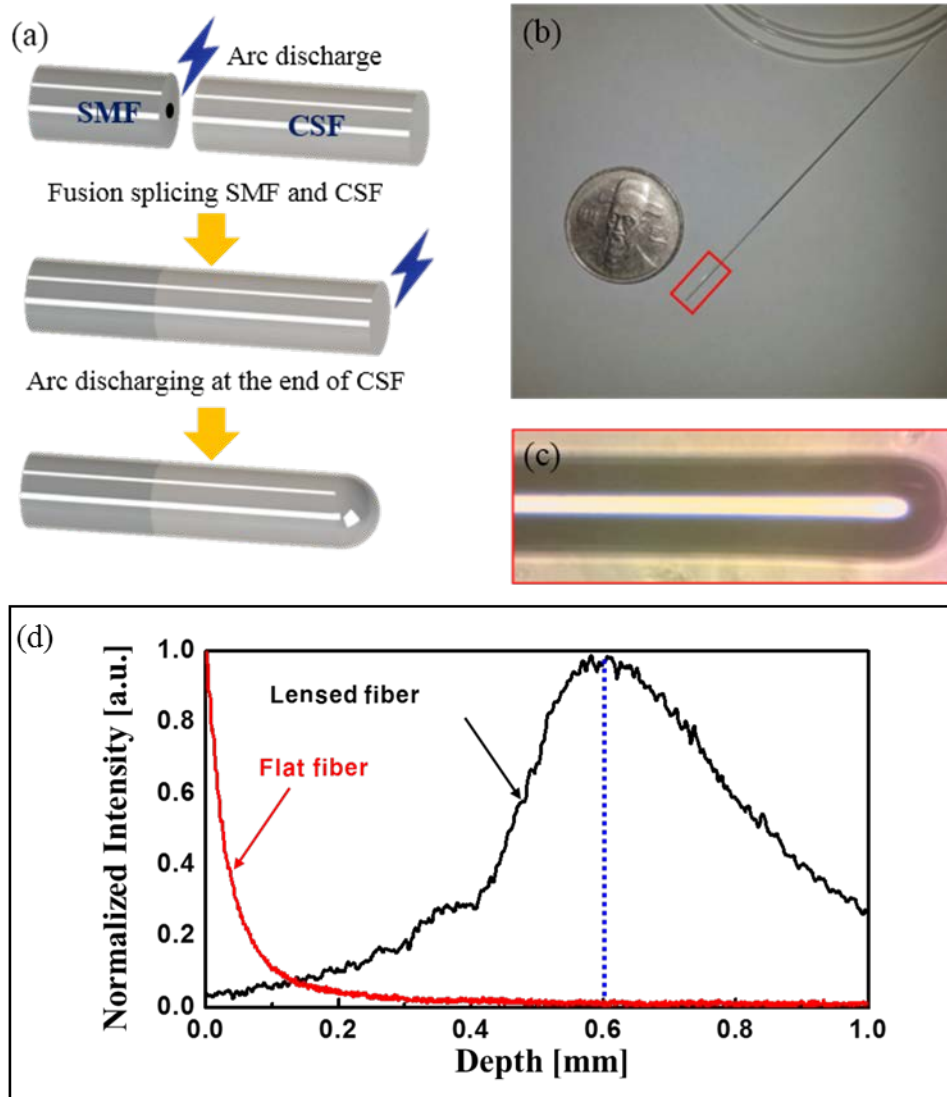


Figure 4-2. Fabrication process of a fiber optic probe. (a) Fabrication process of the lensed fiber. (b) Comparison of the lensed fiber size with coin of 22mm diameter. (c) Image of lensed fiber captured with conventional microscope. (d) Simulation of the lensed fiber beam propagation. Cross-section of the beam from the lensed fiber forms the smallest when working distance (WD) corresponds to the focal point (w_0).




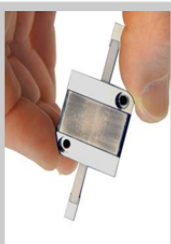

Model	Picture	SQL-RV-1.8	U-264.10	N310	N-412.50
					
Speed (mm/s)	15	10	250	10	5
Resolution (nm)	1	500	100	0.03	300
Length (mm)	22X19X10.8	2.8X2.8X6	57X63X10.2	25X25X12	18X26XRod
Weight (g)	23	0.16	80	50	25
Temperature (°C)	-20~70	-30~80	0~40	0~50	0~50

Table 4-1. Comparison of actuators of various performance. The LL1011A piezo actuator model was selected to compensate for operator hand tremors.

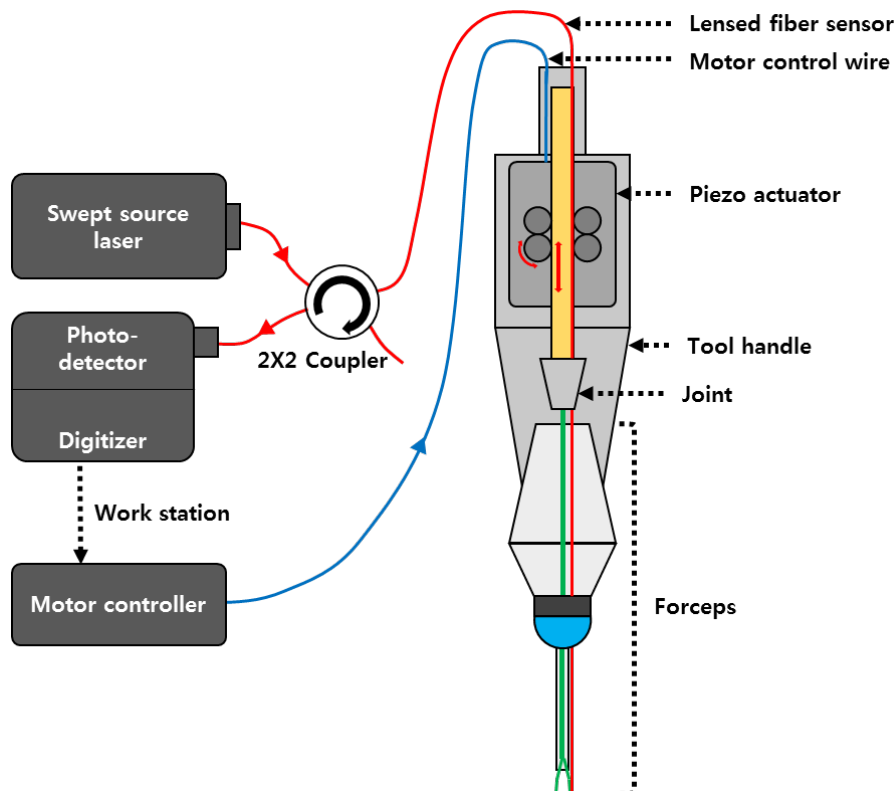


Figure 4-3. Schematic of cross-sectional image for intelligent micro forceps. It consists of a piezo actuator used for motion compensation, a case designed to protect against external influences, and a fiber optic probe for distance measurement.

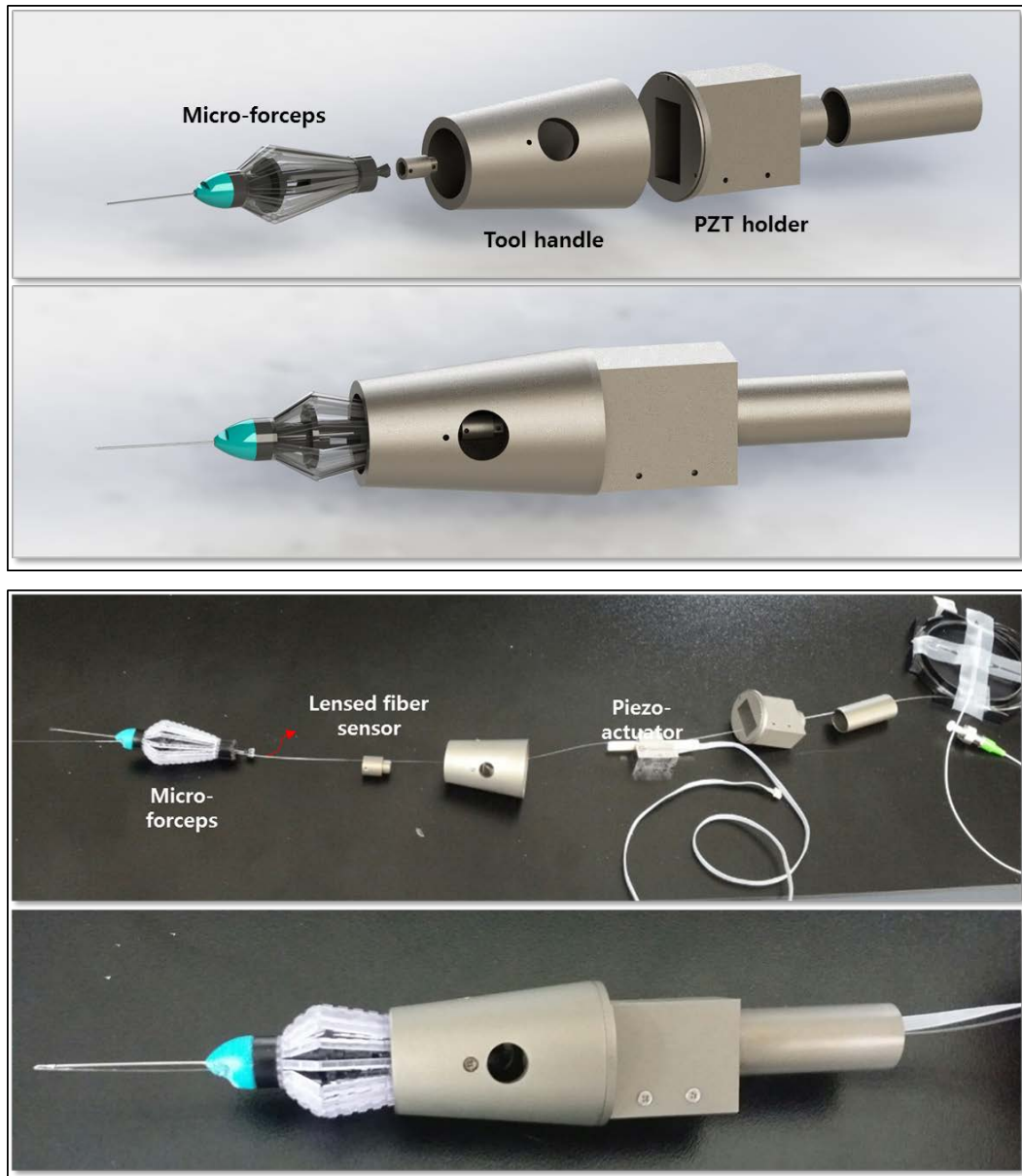


Figure 4-4. The intelligent forceps for hand tremor compensation. (Upper) Schematic of 3D CAD modeling. (Bottom) The actual device in which each part is fully assembled and completed.

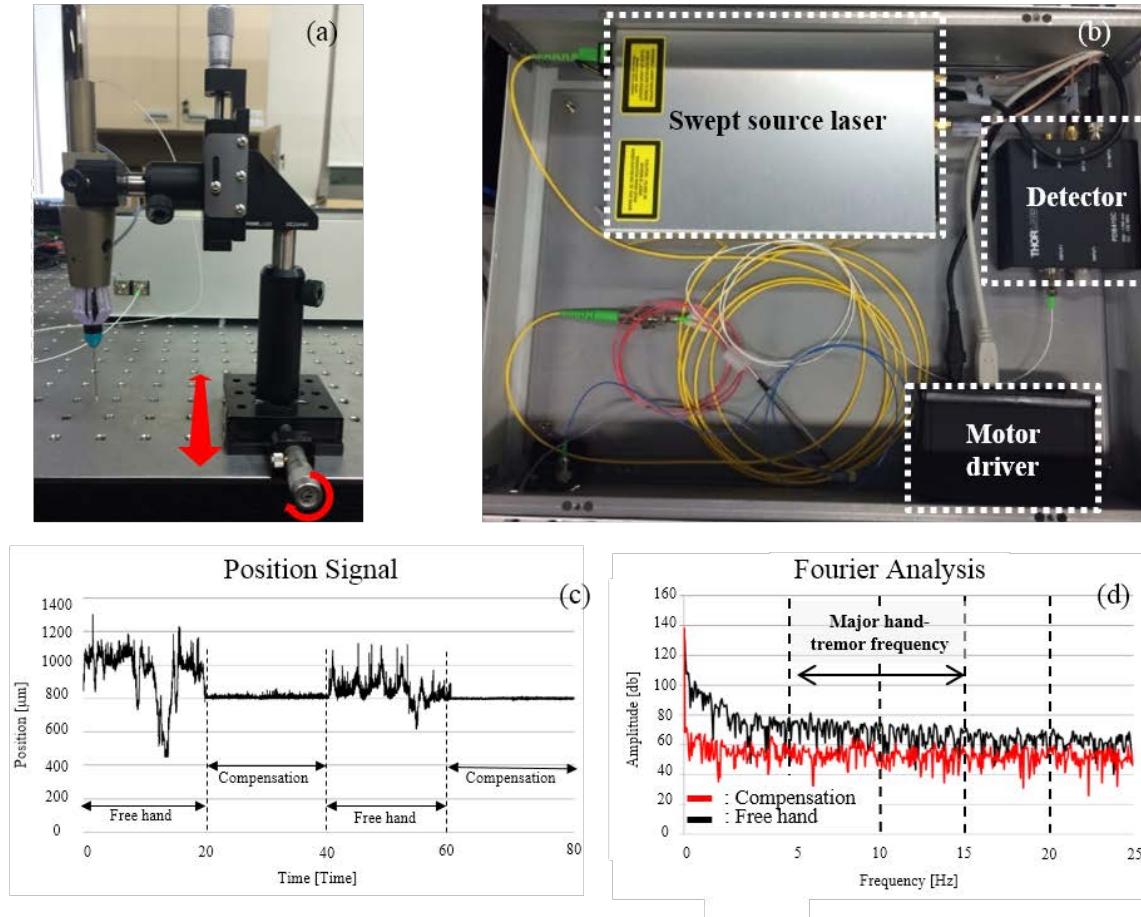


Figure 4-5. System of the intelligent micro-forceps. (a) Image of the intelligent forceps attached on the micro stage for adjusting the distance from the sample. (b) System configuration consisting the Swept source laser, balanced photo detector, and piezo motor driver. (c) Graph of the tip position relative to the target surface while free hand and compensation actuator assisted detecting from the lensed fiber. The Root Mean Square (RMS) value under 20 seconds is 202.92, first compensation interval (20–40 sec) is 9.01. (d) The Fourier analysis of the tip position signal graphs. Here, the amplitude of the free hand and compensated Fourier signal around the major tremor frequency of human, which is from 5 to 15 Hz, is 83.6 and 72.6, respectively. The amplitude of the compensation actuator assisted forceps shows relatively lower in the most of the frequency area. Especially, 13.8 dB is reduced at the major hand tremor frequency band.

4.3 Microsurgery guidance for ophthalmic surgery

4.3.1 Motivation: lamellar keratoplasty

Lamellar keratoplasty (LK) is the transplant procedure to treat disease or injury of cornea which enables partially replacement between recipient's and donor's corneal tissue [79, 80]. Compared to the conventional penetrating keratoplasty (PK) surgery, LK exhibits lower rejection and higher integrity of cornea after transplantation [81-85]. In the case of deep anterior lamellar keratoplasty (DALK), stroma of cornea in dysfunction is to be replaced after being clearly separated out from the Descemet membrane (DM). The remaining lower layers should be a clear and uniform surface for successful DALK surgery. Because a human cornea is thin as shown in Figure 4-6, typically less than ~ 1 mm, the separation process needs a specialized surgical technique.

Anwar's big-bubble technique has been proven to be the most successful for this purpose [86-88]. In the big-bubble technique as shown in Figure 4-7, the air is injected through a thin syringe needle that is inserted inside the patient's cornea. The air blow softly makes uniform corneal segments by inflating the air bubble in the cornea. Here, inserting the needle in the cornea is a deadly part of the procedure. The needle may produce a fatal perforation if inserted too deeply or no big-bubble may be formed if the air is injected at a shallow position. So far, the needle insertion has been performed with no given direct information about the depth of the needle's tip, just with help of en-face visual guidance from the surgical microscope. As a consequence of the required precisions of the needle work in DALK, surgeon could has the risk for perforation the corneal tissue [89, 90]. Moreover, it is difficult to predict visual outcome because of the presence of uneven residual stromal thickness [91].

In order to assist the sophisticated nature of the big-bubble formation, the use of a intraoperative optical coherence tomography (iOCT) [92-96] or iOCT with surgical microscope imaging system [21, 23, 97-99] has been considered for the DALK procedures. Monitoring the needle's manipulations in cornea, one can safely handle a sharp needle and better determine the injection point with knowledge of the depth. However, there is still room to be improved for OCT visualizing entire surgical procedure with comprehensive 3D image in real time [100, 101]. Moreover, the metallic needle is opaque that the underlying tissue becomes invisible in the OCT images [102].

In this report, we introduce a novel position-guided needle combined with M-mode OCT for the DALK procedures. Whereas the OCT needles developed in the previous studies were mainly for diagnostic imaging [19, 103-107], our needle was used for fluid injection just like the ordinary syringe needles as well as position sensing. The performance of our M-mode OCT imaging system was initially evaluated through the phantom mimicking cornea, and its applicability in real ophthalmic surgery was identified in the animal model *ex vivo*.

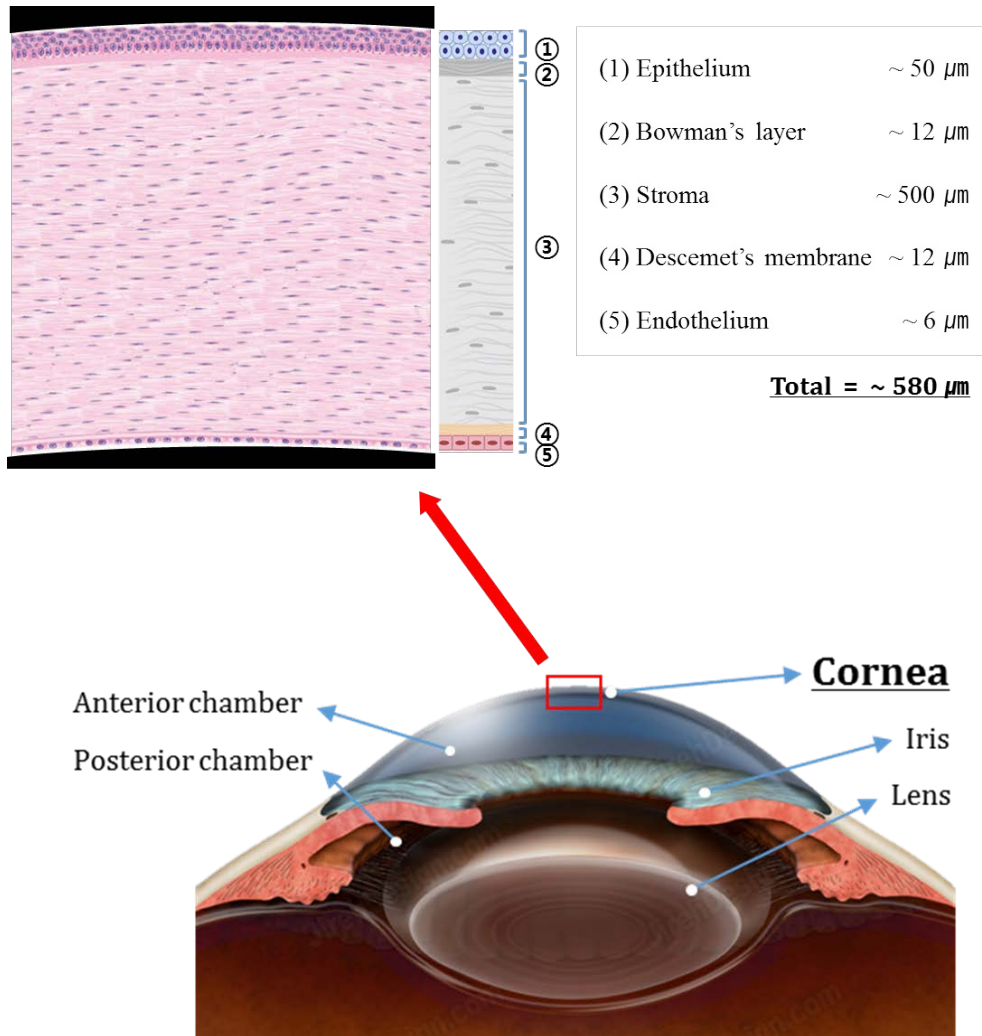


Figure 4-6. Schematics of anterior segment of human eye. Corneal structure consists of five layers with different thicknesses. The total thickness is about five-hundred and eighty micro-meter.

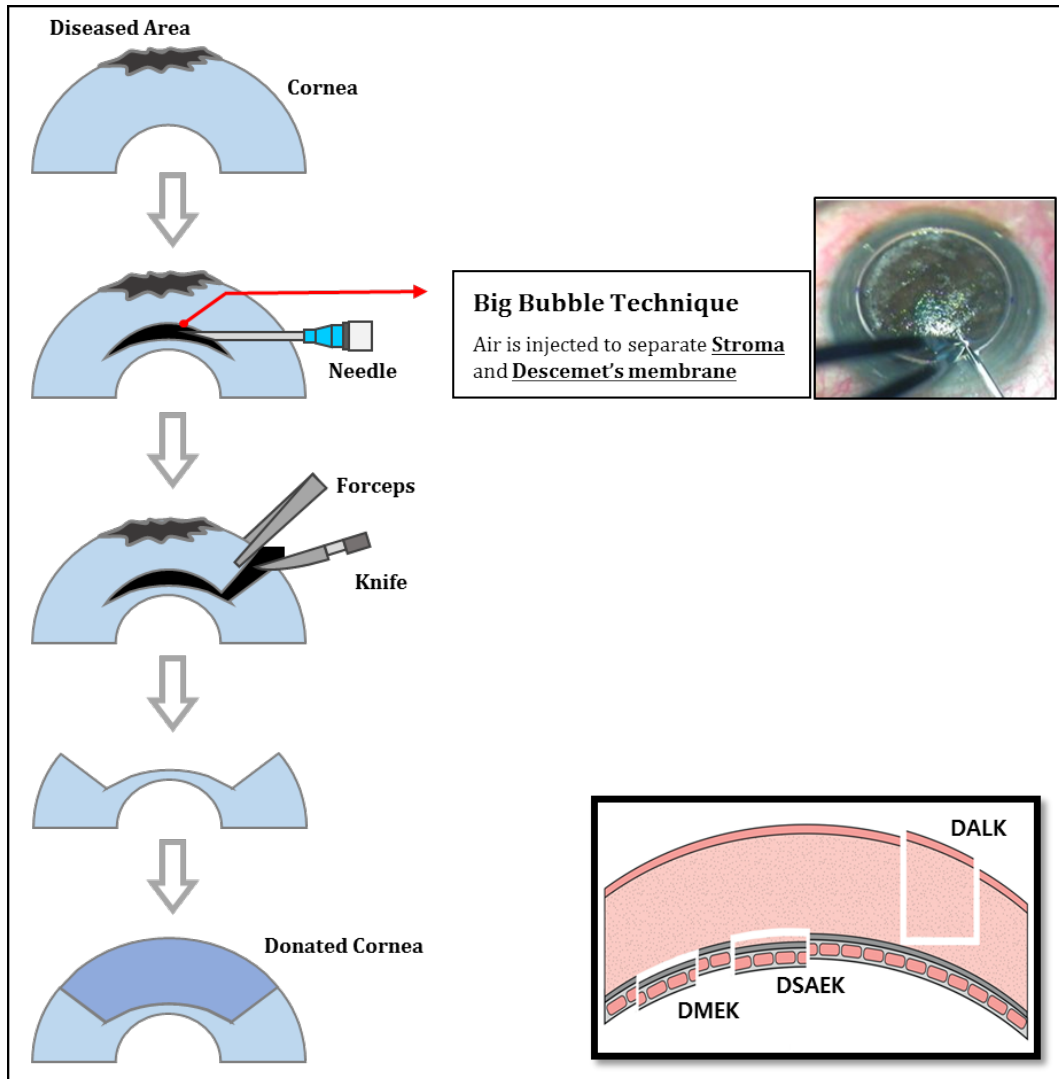


Figure 4-7. Anwar's big-bubble technique for successful DALK surgery. The air is injected through a thin syringe needle that is inserted inside the patient's cornea. The air blow softly makes uniform corneal segments by inflating the air bubble in the cornea.

4.3.2 M-mode OCT needle

Position-guided surgical needle

We employed a stepwise transitional core (STC) fiber enabling the function of position sensor [105]. STC fiber was composed of three different size of single mode fibers (SMF), and large core fiber (LCF) which was built to position-guided needle as shown in Figure 4-8. In order to manufacture the fiber-based position sensor, SMFs were spliced in a sequence of increasing core size, 8.2 μm , 12.5 μm , and 20 μm . Then, LCF with 29 μm core size was attached and a reflector plane was developed at the end, which intended to be exceeding the 44° for total internal reflection. The light coming from SMF pass through transitional fibers (TFs) gradually enlarges a mode field diameter in a stepwise manner. When light reaches to LCF, a low divergence beam having a long effective working distance is propagated. An angle-polished reflector plane at the end of LCF delivers the nearly perpendicular output beam. The STC fiber having $\sim 85 \mu\text{m}$ diameter and 1.1dB of coupling efficiency was fabricated, and packaged with a $\sim 160 \mu\text{m}$ metal jacket for protection. Eventually, it was integrated to 26 gauge needle (0.26 mm of inner, 0.46 mm of outer diameter, and 50 mm length). The minimum beam width of completed STC fiber in needle was 24 μm at $\sim 0.1 \text{ mm}$, and its effective imaging range was $\sim 1 \text{ mm}$ for typical tissues of $n = 1.4$ using Rayleigh length equation. The average lateral resolution of our STC fiber integrated position-guided needle was 30 μm within the effective imaging range.

In order to acquire the depth information from the needle, we utilized the home-built swept source OCT (SS-OCT) imaging system as shown in Figure 4-9. A swept source laser (Axsun Technologies Inc., USA) centered at 1310 nm with bandwidth of 105 nm was incorporated into the SS-OCT system. 90:10 coupler split the light emitted from the swept source laser into the mirror in reference arm and sample arm. Position-guided needle was attached to the sample arm in our system to achieve optical signals from the inside of the tissue. Reflections from each arm were combined and generated the spectral interference signals at the 50:50 coupler. A balanced photo detector (PDB450C, Thorlabs Inc., USA) and digitizer (ATS9350, Alazar Technologies Inc., Canada) were utilized to detect the interference signals. A fast Fourier transform (FFT) was computed to achieve the position profile (M-mode OCT), which has an axial resolution of $\sim 7 \mu\text{m}$. Our customized SS-OCT system facilitates 50 kHz A-line acquisition. Approximately 0.01 seconds was required to update the depth information.

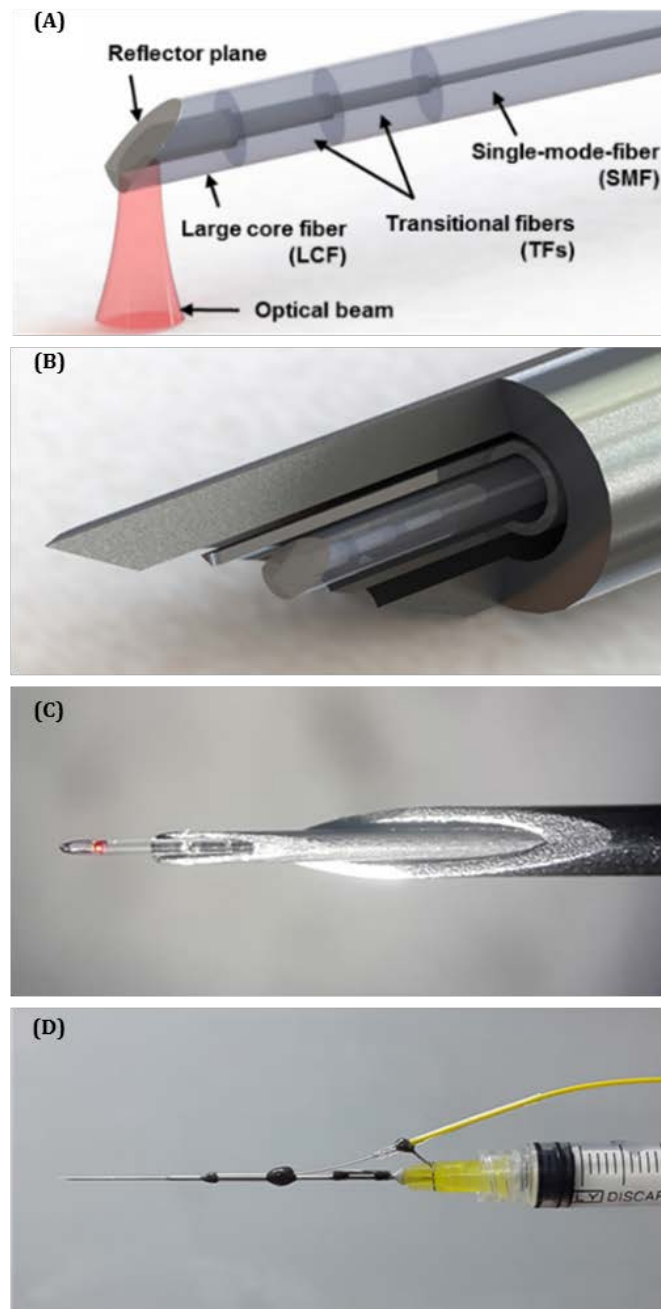


Figure 4-8. Design of position-guided needle. (A) Schematic of stepwise transitional core (STC) fiber [105]. (B) 3D CAD of STC fiber integrated needle. (C) Photo of STC fiber wrapped in metal jacket. (D) Complete position-guided needle applied to 26 gauge needle.

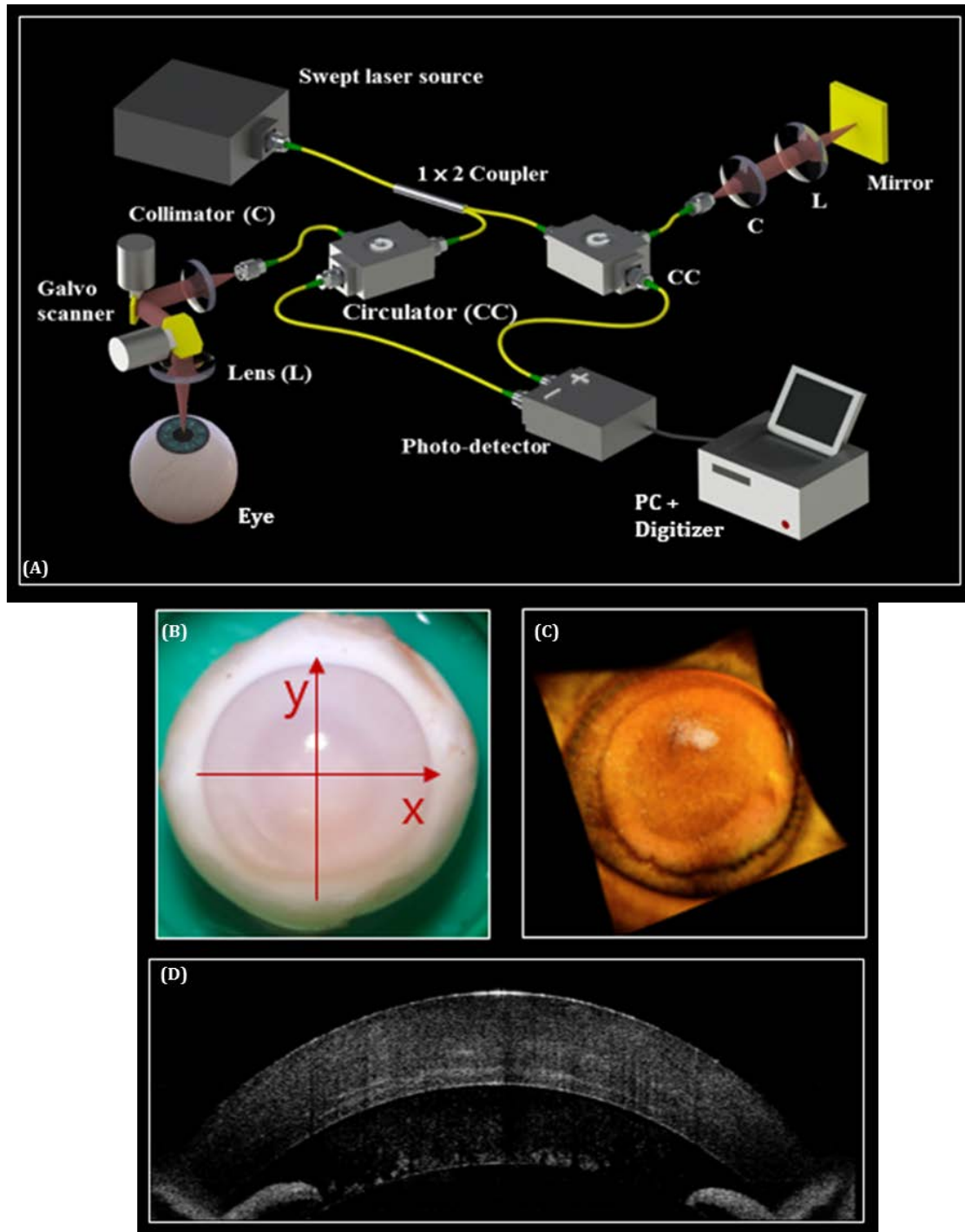


Figure 4-9. Schematic and 2D/3D OCT images of regular OCT imaging system. (A) Schematic of regular OCT imaging system. (B) Microscopic image of rabbit eyeball. (C) 3D OCT image of rabbit eyeball. (D) Cross-sectional image with regular OCT imaging system.

Computational steps for M-mode OCT imaging

The computational steps of our customized system are shown as flow chart in Figure 4-10. Two main parts are performed sequentially to monitor the needle-placement inside of the tissue in real-time. When digitizer detect a triggered-signal from swept-source laser, the system starts to acquire an A-line which consists 1024 samples. As 500 A-lines stacked sequence starts from beginning of acquisition and the stacked data is transferred to queue based on first-in-first-out (FIFO) method. In the signal processing part, DC signals are subtracted. Next, apodization is applied to each A-lines from the stacked data utilizing the hanning window for enhancement of the image contrast. Then, the FFT processing is performed to get axial profile. Averaging of 500 processed A-line data is computed to reduce speckle noise in axial profile. Eventually, axial position profile acquired from position-guided needle is displayed on the graph as an intensity and process sequence iterates when queue buffer incorporates any data. For our system, both acquisition and processing speed were designed to be around 10 milliseconds makes system avoiding the overflow in queue to reduce the latency on data update.

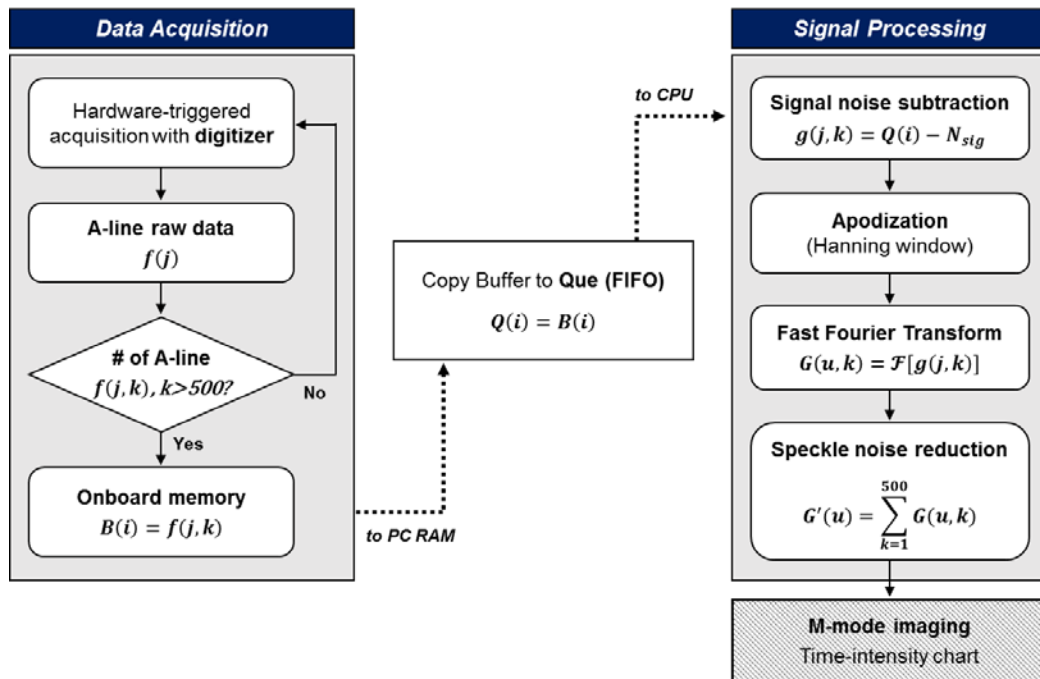


Figure 4-10. Flow chart of computational steps for real-time M-mode OCT imaging. A high-speed digitizer was used for data acquisition, and M-mode images were displayed on the time-intensity chart through signal processing.

Preparation of corneal-mimicking phantom

For the device verification, we prepared the corneal-mimicking phantom which has two layers where the top layer represents the cornea and the bottom one is the anterior chamber. The top layer was prepared by blending an agarose powder and distilled water, and a scatterer was added to the mixture to increase the optical scattering and to imitate the stroma texture. The bottom layer had a low concentration of mixture compared to the top layer for a realization of transparent area of the anterior chamber. The mixtures with different concentrations of agarose were poured into a tray subsequently, and then agarose based corneal-mimicking phantom was produced completely with solidification. Fabricated phantom with 1mm thickness was then utilized to evaluate the functions of the developed position-guided needle. The needle was inserted into the phantom to confirm whether it is able to be reached to an exact position inside phantom model.

Surgical procedure in ex vivo rabbit eye

The rabbit eyes were harvested from two New Zealand rabbits weighting 2.0 ~ 2.5 kg that were euthanized for approved protocols of the institution. All animal procedures in this study were conducted in accordance with institutional guidelines and approved Institutional Animal Care and Use Committee at the College of Medicine, the Catholic University of Korea. The rabbit eye was hold on an anterior chamber manufactured by 3D printer for an optimal surgical procedure. The anterior chamber consisted of a plastic cradle with two nozzles which controlled pressure using water and air to fasten the eye tightly. After setting the eye on the cradle, position-guided needle inserted into the cornea and it measured a remaining thickness of the cornea in real-time when the needle end was moving toward a border between cornea and anterior chamber. When the needle end was reached a target location inside cornea, the air was blown through the needle to separate two layers.

4.3.3 Result

System characteristics

As major characteristics of M-mode OCT imaging system, sensitivity and latency were acquired. To obtain sensitivity of developed system, first of all, signal-to-noise (SNR) of STC fiber integrated position-guided needle was measured by placing a mirror in front of the needle end. We took the ratio between the peak of the amplitude of the point-spread-function after FFT of data and the measured value of noise floor when the reflection was blocked in sample arm. The measured maximum SNR value was around 25 dB. It was found that the apodization and resampling process applied to the original signals dramatically reduced the noise level which mostly placed at -10 dB. To test the system performance for the reflected signal measurement as a function of the ranging distance, a mirror was used. Figure 4-11(A) shows the depth dependent signal decay for the mirror at different optical path difference positions, where a decrease of ~12 dB over a depth range of 2 mm was observed for our system.

Also latency, as capability of real-time display, is another important characteristics for M-mode OCT imaging system. Utilizing the 50 kHz trigger-signal from laser source made time of processing loop to be ideally around 10 milliseconds. We measured loop time including the acquisition and computation loops for 600 seconds and presented the result as time-trip chart as shown in Figure 4-11(B). Loops were performed for 60,000 times to visualize the depth information, mostly for 10 milliseconds.

Evaluation of phantom study

Cornea mimicking phantom made by solidified agarose layers with different concentrations and scatters was evaluated as shown in Figure 4-12(A) in order to identify the accuracy of position-guided needle as position sensor. The boundary of the phantom layers as shown in Figure 4-12(B) was clearly visualized from regular OCT images as shown in Figure 4-12(C) and M-mode imaging from position-guided needle as shown in Figure 4-12(D) while needle moves deeper inside of the phantom. Here, the regular OCT imaging system was utilized to estimate the needle end in cross-sectional view. A-line profile acquired from needle end was continuously monitored as it was inserted into the phantom. A-line profile was directly converted and visualized as the physical thickness, while reflecting the calibration table of needle location. Figure 4-12(D) presents the demonstration when position-guided needle is applied to the cornea phantom and approaches the desired distance. As the needle end penetrates the surface of the phantom, the depth information describing the whole phantom thickness visualized as a graph by stacking them for every 10 milliseconds.

The Figure 4-12(D) shows the correct needle position inside of the phantom. The red and yellow arrows shown in Figure 4-12(C) denote the distance between distal end of the needle and the surface of the next layer, which corresponds to the thickness of the image. Hence, when the needle was just inserted to the phantom, thickness of boundary was closer as it marked with red arrow. Therefore, we were able to understand the location of the needle inside of the phantom in real time.

Evaluation of animal study

The M-mode OCT needle was applied to DALK procedure with rabbit animal model *ex vivo*. Figure 4-13 showing illustrates the image guidance procedure approaching the needle near DM of the enucleated rabbit eyeball to prepare for the next step of surgical process.

As position-guided needle with the facing bevel downward is carefully penetrated tangentially into paracentral rabbit cornea. The live feed-back of inserted needle is visualized on the monitor to help clinician to perceive the depth ratio. Whole cornea thickness is visualized at the epithelial layer and gets thinner when needle approach deeper and near paracentral cornea. Moreover, additional signals were detected under the cornea layer as needle gets near DM. Assuming from the morphology, these signals were coming from the iris of rabbit eye. The green line shown in the Figure 4-13 traces the residual thickness between DM and needle end, and provide user-friendly interface, making clinician easier to make decision. Demonstration of our probe was successfully performed and it is found that position-guided needle has great potential of applying it to clinical setting.

Clinician usually laid the needle parallel to the corneal surface in order to avoid the perforation under the DM layer and to separate the cornea layer with reduced stroma damages when big-bubble technique is performed. We further evaluated the feasibility of our needle by imaging the big-bubble technique applied rabbit eyeball with customized SS-OCT system and studied the morphology of it. In order to capture regular OCT images, the surgical needle was replaced to the 2-axis galvo-scanner at sample arm. $512 \times 500 \times 500$ voxel of OCT images were captured immediately after needle reached the $100 \mu\text{m}$ above the DM layer in rabbit eyeball. In addition, air was injected into the cornea to perform the big-bubble technique and the OCT images were captured above the cornea surface as well. Figure 4-14 shows that the needle was inserted into the enucleated rabbit eyeball (already performed in above section). As shown the Figure 4-15, 3D image presents the whole structure of cornea including the needle. Blue and red line presents the cross-sectional image perpendicular and parallel to the needle, respectively. It is clearly shown that needle end was placed perpendicular with surface of paracentral of cornea and any damage or perforation was not found as shown in Figure 4-15(A) denoted yellow arrow. After big-bubble technique was applied, Figure 4-15(B) shows that more than half of stroma layer was detached and air was filled underneath. According to Figure 4-15, it is visually verified that DALK was successfully demonstrated without any tissue damages by applying position-guided needle which provides the depth information.

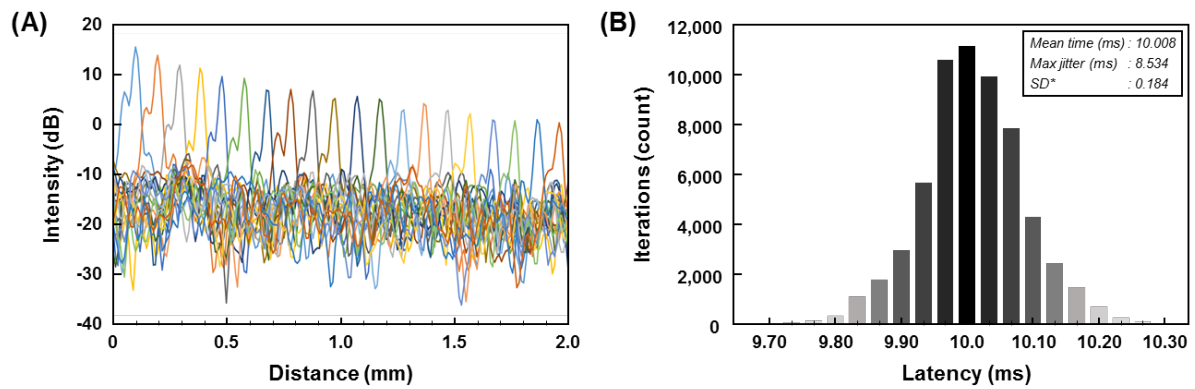


Figure 4-11. Performance representing chart for system sensitivity and latency. (A) SNR graph of STC fiber integrated position-guided needle represent decrease of signal intensity to 12 dB across depth range of 2 mm. (B) Latency histogram of the M-mode OCT imaging system. The average of loop time was 10.008 milliseconds with maximum 8.534 milliseconds and standard deviation of 0.184. SD* : standard deviation.

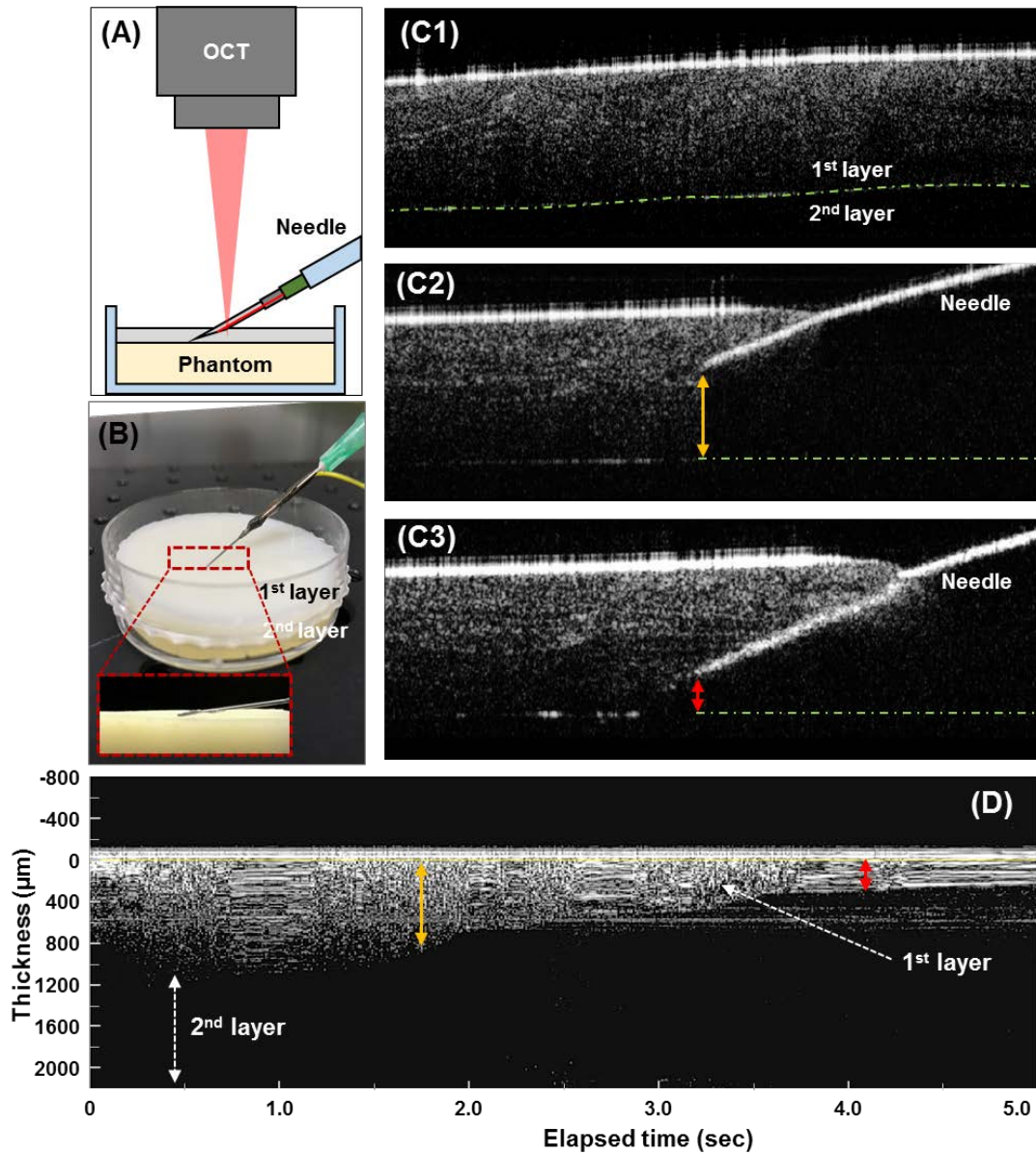


Figure 4-12. Phantom study evaluating the feasibility of the position-guided needle combined with M-mode OCT. (A) Schematic diagram of phantom study. (B) Corneal mimicking phantom developed with double layers of different concentrated agarose. (C1)-(C3) regular OCT image was presented when the needle punched through the surface of agarose jell and passed by the middle of first layer at 1.68 sec, and came closer to 2nd layer at 4.14 sec, respectively. (D) M-mode imaging from position-guided needle in real time that has capability of tracking depth information. Red and yellow arrows denote the residual thickness between the needle distal end and the boundary (assuming the Descemet's membrane and endothelium) within the phantom, respectively.

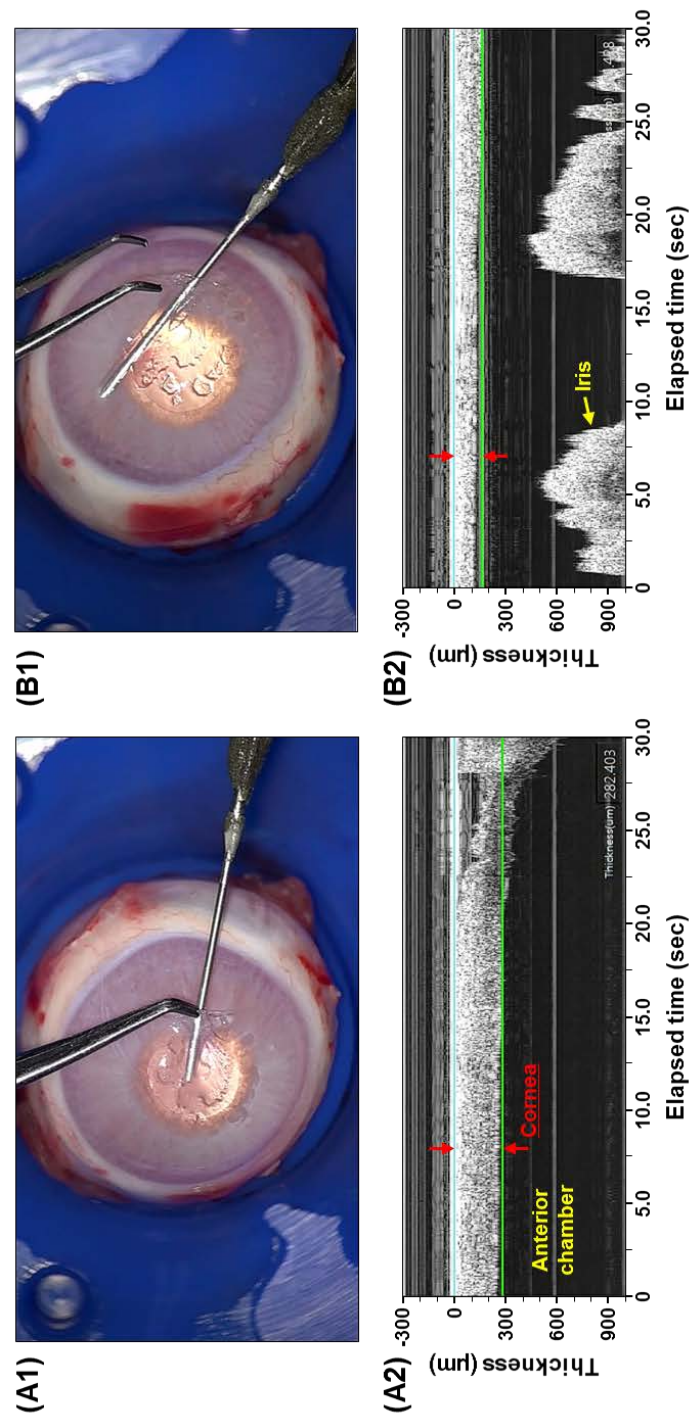


Figure 4-13. Animal study on rabbit eyeball demonstrating the M-mode OCT needle. (A1) Animal surgery using position-guided needle when the tip of needle was inserted into the first layer of cornea. (A2) The corresponding M-mode OCT image from the needle when its tip was maintaining the cornea layer with residual thickness of around 300 μm . (B1) Next medical procedure when the surgeon was aided with the needle to quantitatively find out the desired position of cornea. (B2) The corresponding M-mode OCT image was captured when the needle approached near Descemet's membrane (DM) of the enucleated rabbit eyeball and detected the rest of cornea thickness within 100 μm .

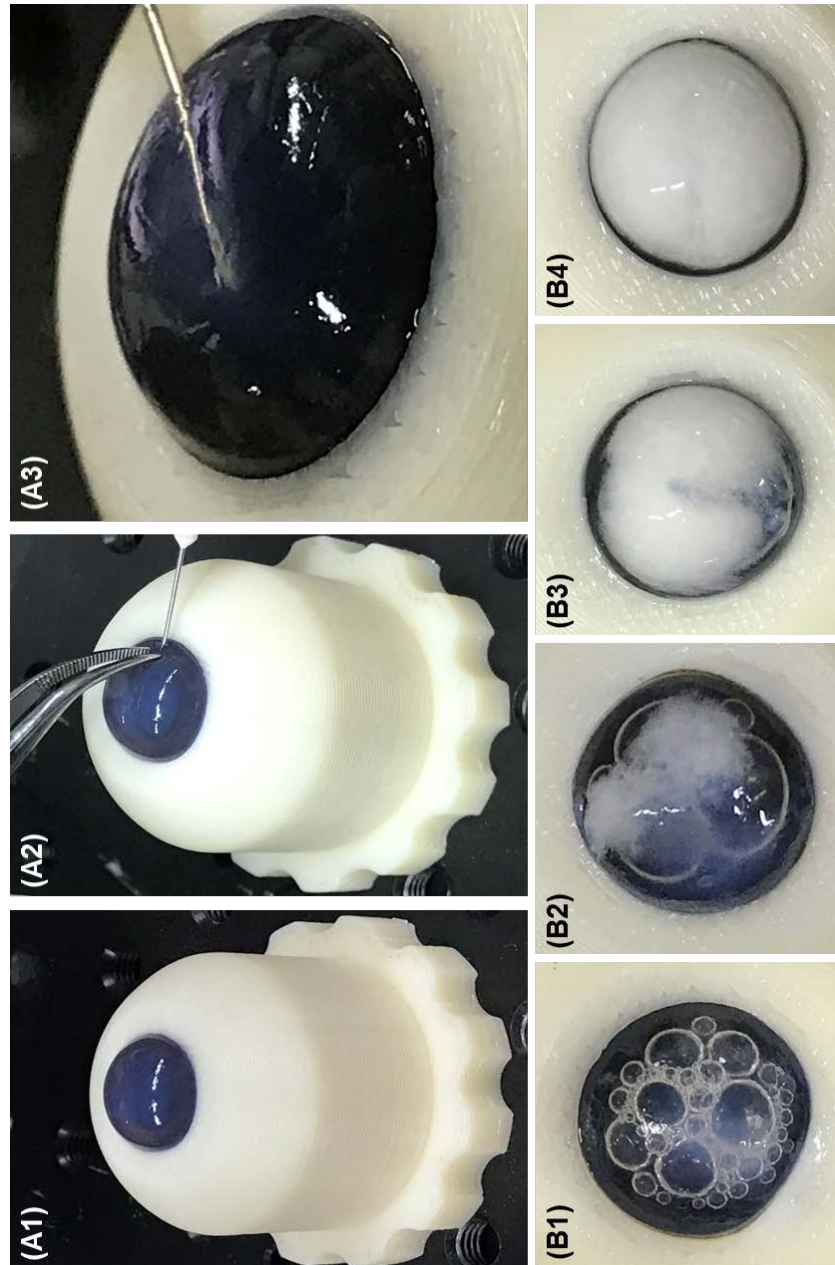


Figure 4-14. Anterior chamber made with 3D printer to hold rabbit eyes. (A1)-(A3) Process of inserting needle before air injection into the rabbit eye. (B) Failed big-bubble case 1, 2 and successful big-bubble case 3, 4 after air injection.

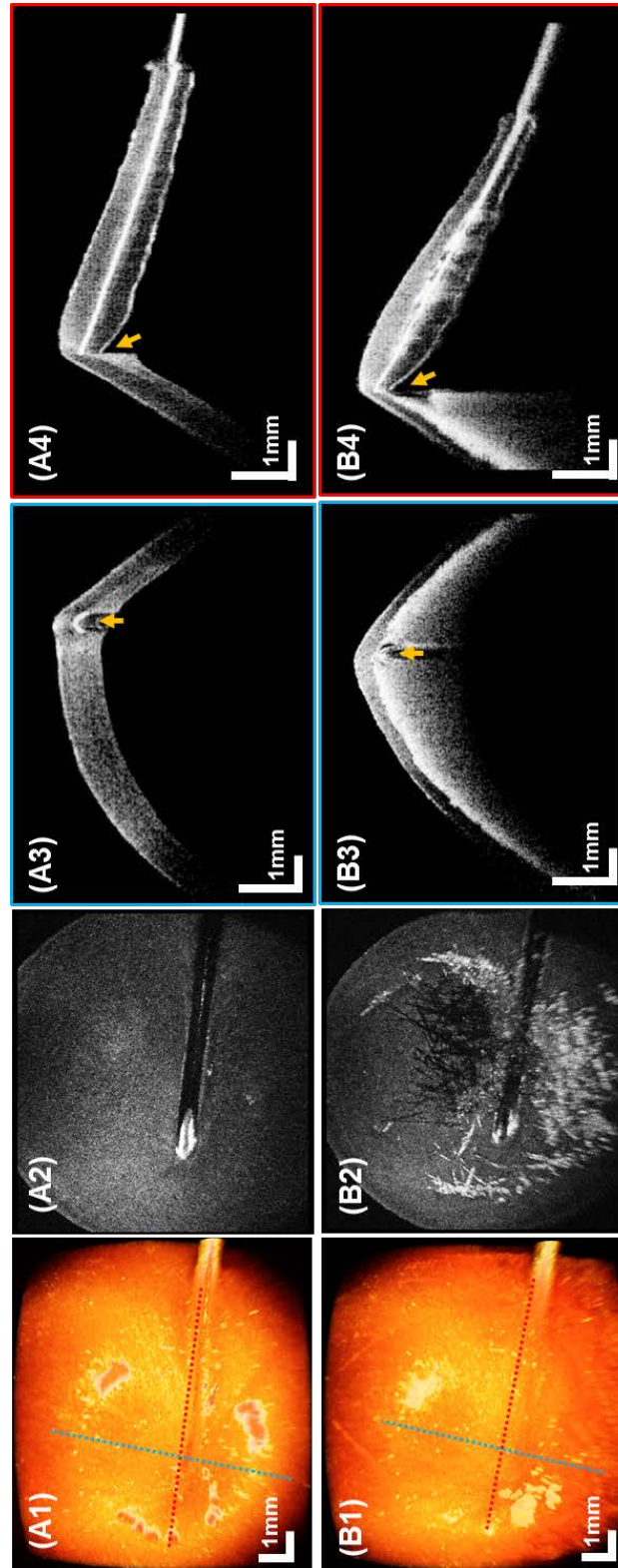


Figure 4-15. $512 \times 500 \times 500$ voxel of OCT image was captured immediately after needle tip reached the remained cornea layer with thickness of $100\mu\text{m}$. (A1) – (A4) 3D OCT image, en-face image, and cross sectional images in different view before air injection. (B1) – (B4) after air injection.

4.4 Conclusion

In this study, we introduced the novel M-mode OCT needle for aiding the accurate DALK surgery. Since the developed needle had functionality not only simple air bubble injection, but also position sensing, it would improve the surgical yield of DALK while minimizing the fatal perforation due to unexpected needle manipulation. The STC fiber operating as an optical sensor in surgical needle was successfully traced the position of needle end in real-time which was confirmed by phantom study. Through the animal model, we found that the position-guided surgical needle provided accurate feedback regarding needle end placement inside cornea and helped to stable air bubble formation. Furthermore, displaying the position information as an image could help for user easily to detect the region of dysfunctional tissue, and offer the comprehensive information during entire surgery. Thus, experimental results presented that our device and corresponding new surgical protocol has great potential for use in DALK as well as other microsurgery.

However, the current of our device can be enhanced and matured by adapting other advanced engineering techniques. Our surgical needle can readily be integrated into an existing intraoperative OCT with surgical microscope or implemented as hand-held surgical tool. In previous study, many literatures have been reported to successful adaptations of OCT for a surgical tool and its potential for monitoring the surgical procedures. Since OCT is modular system, imaging path of OCT system can either to be shared for both intraoperative OCT imaging as well as sensor. Few studies were already described the feasibility of intraoperative OCT to DALK. Thus, the combination of existing intraoperative OCT and our device would make great impact for microsurgery which requires the precise manipulation of needle as well as the continuous observation of surgical region. Our device platform can also be transformed as tremor compensating device [72] by utilizing the motion feedback actuator and software based on our position information. In addition, current position information can be converted to sound interpretation for becoming the user friendly surgical device. Thus, a fully developed and ergonomically-engineered surgical needle would find numerous applications where precise depth information of needle with morphologic data could be required in microsurgery as well as drug delivery [108].

CHAPTER 5. Concluding remarks

OCT technology, which provides high-resolution images, was introduced in Chapter 1. The motivation to satisfy clinic needs in microsurgery through engineering solutions has been presented. My thesis research focused on overcoming current limitations by developing intraoperative OCT and novel surgical instruments.

In Chapter 2, I applied high-speed OCT technology for practical clinical studies of thyroid cancer surgery. To provide the clinician with information about the invasion of the thyroid capsule, an intraoperative OCT image identifying the microscopic ETE was demonstrated. As a result, OCT images were compared with histological images, and more than 84% accuracy was confirmed from the pathology report. This study is the first research to introduce an intraoperative OCT that can improve the intraoperative examination of thyroid cancer using conventional ultrasound with an accuracy of about 60%.

In Chapter 3, I developed a smart surgical microscope system that combine the intraoperative OCT introduced above into a surgical microscope for use during actual surgery. The surgeon can not frequently take his eyes off the eyepiece of the surgical microscope during surgery in the operating room. For this reason, our smart surgical microscope could overlay the OCT images of tissue in the eyepiece view. So, we combined the beam path of the OCT and the surgical microscope to observe the matched area. The OCT image was displayed on the eyepiece using a beam projector.

Finally, in Chapter 4, I introduced two types of novel surgical instruments. In the microsurgery using conventional surgical instruments, a technique for providing more safety by compensating for a human hand tremor was required. Our fiber sensors attached to the end of the surgical instrument measured the position information and the error-based control is performed on the piezo actuator to compensate for tremor. In order to evaluate the performance of this intelligent forceps, we performed compensation frequency analysis and showed about 13dB of Tremor compensation performance. A position-guided needle was developed with other types of surgical instruments. STC fiber was fabricated as a sensor to measure needle position information and M-mode OCT imaging method for real-time surgical guide was presented. The developed position-guided needle was applied to DALK surgery and showed its feasibility through an ex-vivo study.

References

1. D. R. Macdonald, T. L. Cascino, S. C. Schold, Jr., and J. G. Cairncross, "Response criteria for phase II studies of supratentorial malignant glioma," *J Clin Oncol* **8**, 1277-1280 (1990).
2. R. K. Ten Haken, A. F. Thornton, Jr., H. M. Sandler, M. L. LaVigne, D. J. Quint, B. A. Fraass, M. L. Kessler, and D. L. McShan, "A quantitative assessment of the addition of MRI to CT-based, 3-D treatment planning of brain tumors," *Radiother Oncol* **25**, 121-133 (1992).
3. J. G. Fujimoto, C. Pitris, S. A. Boppart, and M. E. Brezinski, "Optical coherence tomography: an emerging technology for biomedical imaging and optical biopsy," *Neoplasia* **2**, 9-25 (2000).
4. S. A. Boppart, W. Luo, D. L. Marks, and K. W. Singletary, "Optical coherence tomography: feasibility for basic research and image-guided surgery of breast cancer," *Breast Cancer Res Treat* **84**, 85-97 (2004).
5. W. Drexler, M. Liu, A. Kumar, T. Kamali, A. Unterhuber, and R. A. Leitgeb, "Optical coherence tomography today: speed, contrast, and multimodality," *J Biomed Opt* **19**, 071412 (2014).
6. W. A. Welge and J. K. Barton, "Expanding Functionality of Commercial Optical Coherence Tomography Systems by Integrating a Custom Endoscope," *PLoS One* **10**, e0139396 (2015).
7. G. J. Tearney, M. E. Brezinski, B. E. Bouma, S. A. Boppart, C. Pitris, J. F. Southern, and J. G. Fujimoto, "In vivo endoscopic optical biopsy with optical coherence tomography," *Science* **276**, 2037-2039 (1997).
8. D. Huang, E. A. Swanson, C. P. Lin, J. S. Schuman, W. G. Stinson, W. Chang, M. R. Hee, T. Flotte, K. Gregory, C. A. Puliafito, and et al., "Optical coherence tomography," *Science* **254**, 1178-1181 (1991).
9. J. G. Fujimoto, M. E. Brezinski, G. J. Tearney, S. A. Boppart, B. Bouma, M. R. Hee, J. F. Southern, and E. A. Swanson, "Optical biopsy and imaging using optical coherence tomography," *Nat Med* **1**, 970-972 (1995).
10. A. F. Fercher, C. K. Hitzenberger, W. Drexler, G. Kamp, and H. Sattmann, "In vivo optical coherence tomography," *Am J Ophthalmol* **116**, 113-114 (1993).
11. E. A. Swanson, J. A. Izatt, M. R. Hee, D. Huang, C. P. Lin, J. S. Schuman, C. A. Puliafito, and J. G. Fujimoto, "In vivo retinal imaging by optical coherence tomography," *Opt Lett* **18**, 1864-1866 (1993).
12. R. Leitgeb, C. Hitzenberger, and A. Fercher, "Performance of fourier domain vs. time domain optical coherence tomography," *Opt Express* **11**, 889-894 (2003).

13. J. F. de Boer, B. Cense, B. H. Park, M. C. Pierce, G. J. Tearney, and B. E. Bouma, "Improved signal-to-noise ratio in spectral-domain compared with time-domain optical coherence tomography," *Opt Lett* **28**, 2067-2069 (2003).
14. M. Choma, M. Sarunic, C. Yang, and J. Izatt, "Sensitivity advantage of swept source and Fourier domain optical coherence tomography," *Opt Express* **11**, 2183-2189 (2003).
15. M. Wojtkowski, R. Leitgeb, A. Kowalczyk, T. Bajraszewski, and A. F. Fercher, "In vivo human retinal imaging by Fourier domain optical coherence tomography," *J Biomed Opt* **7**, 457-463 (2002).
16. S. A. Boppart, B. E. Bouma, C. Pitris, G. J. Tearney, J. G. Fujimoto, and M. E. Brezinski, "Forward-imaging instruments for optical coherence tomography," *Opt Lett* **22**, 1618-1620 (1997).
17. W. Jung, J. Kim, M. Jeon, E. J. Chaney, C. N. Stewart, and S. A. Boppart, "Handheld Optical Coherence Tomography Scanner for Primary Care Diagnostics," *Ieee T Bio-Med Eng* **58**, 741-744 (2011).
18. W. G. Jung, J. Zhang, L. Wang, P. Wilder-Smith, Z. P. Chen, D. T. McCormick, and N. C. Tien, "Three-dimensional optical coherence tomography employing a 2-axis microelectromechanical scanning mirror," *Ieee J Sel Top Quant* **11**, 806-810 (2005).
19. X. D. Li, C. Chudoba, T. Ko, C. Pitris, and J. G. Fujimoto, "Imaging needle for optical coherence tomography," *Optics Letters* **25**, 1520-1522 (2000).
20. Y. K. K. Tao, J. P. Ehlers, C. A. Toth, and J. A. Izatt, "Intraoperative spectral domain optical coherence tomography for vitreoretinal surgery," *Optics Letters* **35**, 3315-3317 (2010).
21. Y. K. K. Tao, S. K. Srivastava, and J. P. Ehlers, "Microscope-integrated intraoperative OCT with electrically tunable focus and heads-up display for imaging of ophthalmic surgical maneuvers," *Biomed Opt Express* **5**, 1877-1885 (2014).
22. J. P. Ehlers, S. K. Srivastava, D. Feiler, A. I. Noonan, A. M. Rollins, and Y. K. K. Tao, "Integrative Advances for OCT-Guided Ophthalmic Surgery and Intraoperative OCT: Microscope Integration, Surgical Instrumentation, and Heads-Up Display Surgeon Feedback," *Plos One* **9**(2014).
23. J. P. Ehlers, P. K. Kaiser, and S. K. Srivastava, "Intraoperative optical coherence tomography using the RESCAN 700: preliminary results from the DISCOVER study," *Brit J Ophthalmol* **98**, 1329-1332 (2014).
24. D. Huang and M. Shure, "Handbook of optical coherence tomography," *Ophthalmic surgery, lasers & imaging : the official journal of the International Society for Imaging in the Eye* **34**, 78-79 (2003).
25. A. F. Fercher, "Optical coherence tomography - development, principles, applications," *Zeitschrift fur medizinische Physik* **20**, 251-276 (2010).
26. S. Szpilczynski, "[3d edition of Vitellion's Optics in 1572 in the light of unfavorable comments]," *Archiwum historii medycyny* **38**, 337-341 (1975).

27. E. Hecht, *Optics*, 4th ed. (Addison-Wesley, Reading, Mass., 2002), pp. vi, 698 p.
28. H. J. Gerritsen, W. W. Millbrandt, and R. L. Omega, "A michelson interferometer for use in measuring characteristics of phonograph cartridges," *Applied optics* **9**, 1231-1232 (1970).
29. M. Francon and S. Mallick, "Improvement of the degree of spatial coherence in a Michelson interferometer," *Applied optics* **6**, 873-876 (1967).
30. J. Hu, H. Hu, and Y. Ji, "Detection method of nonlinearity errors by statistical signal analysis in heterodyne Michelson interferometer," *Opt Express* **18**, 5831-5839 (2010).
31. J. J. Monzon and L. L. Sanchez-Soto, "Absorbing beam splitter in a Michelson interferometer," *Applied optics* **34**, 7834-7839 (1995).
32. A. Mabrouki, M. Gadonna, and R. Le Naour, "Polarization characterization of a Mach-Zehnder interferometer," *Applied optics* **35**, 3591-3596 (1996).
33. M. Plewicki, F. Weise, S. M. Weber, and A. Lindinger, "Phase, amplitude, and polarization shaping with a pulse shaper in a Mach-Zehnder interferometer," *Applied optics* **45**, 8354-8359 (2006).
34. T. Mizuno, T. Kitoh, M. Oguma, Y. Inoue, T. Shibata, and H. Takahashi, "Mach-Zehnder interferometer with a uniform wavelength period," *Opt Lett* **29**, 454-456 (2004).
35. S. J. Spammer and P. L. Swart, "Differentiating optical-fiber Mach-Zehnder interferometer," *Applied optics* **34**, 2350-2353 (1995).
36. R. Leitgeb, M. Wojtkowski, A. Kowalczyk, C. K. Hitzenberger, M. Sticker, and A. F. Fercher, "Spectral measurement of absorption by spectroscopic frequency-domain optical coherence tomography," *Opt Lett* **25**, 820-822 (2000).
37. K. Zhang and J. U. Kang, "Real-time intraoperative 4D full-range FD-OCT based on the dual graphics processing units architecture for microsurgery guidance," *Biomed Opt Express* **2**, 764-770 (2011).
38. K. Zhang and J. U. Kang, "Real-time 4D signal processing and visualization using graphics processing unit on a regular nonlinear-k Fourier-domain OCT system," *Opt Express* **18**, 11772-11784 (2010).
39. K. Zhang and J. U. Kang, "Graphics processing unit accelerated non-uniform fast Fourier transform for ultrahigh-speed, real-time Fourier-domain OCT," *Opt Express* **18**, 23472-23487 (2010).
40. J. Luce, M. Hoggarth, J. Lin, A. Block, and J. Roeske, "SU-E-J-91: FFT Based Medical Image Registration Using a Graphics Processing Unit (GPU)," *Medical physics* **39**, 3673 (2012).
41. T. V. Hoang, X. Cavin, and D. W. Ritchie, "gEMfitter: a highly parallel FFT-based 3D density fitting tool with GPU texture memory acceleration," *Journal of structural biology* **184**, 348-354 (2013).
42. S. Schroder, H. Kastendieck, and W. Bocker, "[Occult papillary thyroid carcinoma. Clinical significance and morphology of a common tumor]," *Deutsche medizinische Wochenschrift* **111**, 582-586 (1986).

43. B. K. Chan, T. S. Desser, I. R. McDougall, R. J. Weigel, and R. B. Jeffrey, Jr., "Common and uncommon sonographic features of papillary thyroid carcinoma," *Journal of ultrasound in medicine : official journal of the American Institute of Ultrasound in Medicine* **22**, 1083-1090 (2003).
44. A. Flint, R. D. Davenport, and R. V. Lloyd, "The tall cell variant of papillary carcinoma of the thyroid gland. Comparison with the common form of papillary carcinoma by DNA and morphometric analysis," *Archives of pathology & laboratory medicine* **115**, 169-171 (1991).
45. K. Karunakaran, D. Marudhupandian, R. Ganesan, and M. Gobinath, "Anamolous course of right common carotid artery in a case of papillary carcinoma thyroid," *The Indian journal of surgery* **75**, 145-146 (2013).
46. W. Y. Kim, H. Y. Kim, G. S. Son, J. W. Bae, and J. B. Lee, "Clinicopathological, immunohistochemical factors and recurrence associated with extrathyroidal extension in papillary thyroid microcarcinoma," *Journal of cancer research and therapeutics* **10**, 50-55 (2014).
47. S. Ortiz, J. M. Rodriguez, T. Soria, D. Perez-Flores, A. Pinero, J. Moreno, and P. Parrilla, "Extrathyroid spread in papillary carcinoma of the thyroid: clinicopathological and prognostic study," *Otolaryngology--head and neck surgery : official journal of American Academy of Otolaryngology-Head and Neck Surgery* **124**, 261-265 (2001).
48. S. P. Jung, M. Kim, J. H. Choe, J. S. Kim, S. J. Nam, and J. H. Kim, "Clinical implication of cancer adhesion in papillary thyroid carcinoma: clinicopathologic characteristics and prognosis analyzed with degree of extrathyroidal extension," *World journal of surgery* **37**, 1606-1613 (2013).
49. P. W. Rosario, G. F. Mourao, and M. R. Calsolari, "Apparently intrathyroid papillary thyroid carcinoma >1 and <=4 cm: is the need for completion thyroidectomy common among patients submitted to lobectomy?," *Clinical endocrinology* **85**, 150-151 (2016).
50. N. Wada, H. Nakayama, N. Suganuma, Y. Masudo, Y. Rino, M. Masuda, and T. Imada, "Prognostic value of the sixth edition AJCC/UICC TNM classification for differentiated thyroid carcinoma with extrathyroid extension," *The Journal of clinical endocrinology and metabolism* **92**, 215-218 (2007).
51. H. J. Moon, E. K. Kim, W. Y. Chung, J. H. Yoon, and J. Y. Kwak, "Minimal extrathyroidal extension in patients with papillary thyroid microcarcinoma: is it a real prognostic factor?," *Annals of surgical oncology* **18**, 1916-1923 (2011).
52. H. S. Lee, C. Park, S. W. Kim, T. Park, B. K. Chun, J. C. Hong, and K. D. Lee, "Correlation of minimal extrathyroidal extension with pathologic features of lymph node metastasis in patients with papillary thyroid carcinoma," *Journal of surgical oncology* **112**, 592-596 (2015).
53. H. Yokouchi, K. Kodama, M. Higashiyama, K. Takami, T. Kobayashi, H. Takami, S. Nakamura,

- and T. Horai, "Successful removal of a primitive neuroectodermal tumor in the lung with gross extension into the left atrium," *The Thoracic and cardiovascular surgeon* **47**, 257-259 (1999).
54. J. S. Choi, J. Kim, J. Y. Kwak, M. J. Kim, H. S. Chang, and E. K. Kim, "Preoperative staging of papillary thyroid carcinoma: comparison of ultrasound imaging and CT," *AJR. American journal of roentgenology* **193**, 871-878 (2009).
 55. J. Y. Kwak, E. K. Kim, J. H. Youk, M. J. Kim, E. J. Son, S. H. Choi, and K. K. Oh, "Extrathyroid extension of well-differentiated papillary thyroid microcarcinoma on US," *Thyroid : official journal of the American Thyroid Association* **18**, 609-614 (2008).
 56. Y. M. Park, S. G. Wang, J. Y. Goh, D. H. Shin, I. J. Kim, and B. J. Lee, "Intraoperative frozen section for the evaluation of extrathyroidal extension in papillary thyroid cancer," *World journal of surgery* **39**, 187-193 (2015).
 57. A. P. Labanaris, K. Engelhard, V. Zugor, R. Nutzel, and R. Kuhn, "Prostate cancer detection using an extended prostate biopsy schema in combination with additional targeted cores from suspicious images in conventional and functional endorectal magnetic resonance imaging of the prostate," *Prostate cancer and prostatic diseases* **13**, 65-70 (2010).
 58. B. L. Cohen, "Laws of statistics ignored by statisticians," *Health physics* **35**, 582-584 (1978).
 59. H. S. Lee, S. W. Shin, J. K. Bae, W. G. Jung, S. W. Kim, C. Oak, B. K. Chun, Y. C. Ahn, B. J. Lee, and K. D. Lee, "Preliminary study of optical coherence tomography imaging to identify microscopic extrathyroidal extension in patients with papillary thyroid carcinoma," *Lasers in surgery and medicine* **48**, 371-376 (2016).
 60. D. Schultheiss and J. Denil, "History of the microscope and development of microsurgery: a revolution for reproductive tract surgery," *Andrologia* **34**, 234-241 (2002).
 61. G. Widmann and R. J. Bale, "Accuracy in computer-aided implant surgery--a review," *The International journal of oral & maxillofacial implants* **21**, 305-313 (2006).
 62. A. C. Ho, Y. L. Fisher, J. S. Slakter, D. R. Guyer, J. A. Sorenson, and L. A. Yannuzzi, "Intraoperative indocyanine green videoangiography in subretinal surgery," *Archives of ophthalmology* **112**, 872-874 (1994).
 63. A. P. Da Mata, S. E. Burk, C. D. Riemann, R. H. Rosa, Jr., M. E. Snyder, M. R. Petersen, and R. E. Foster, "Indocyanine green-assisted peeling of the retinal internal limiting membrane during vitrectomy surgery for macular hole repair," *Ophthalmology* **108**, 1187-1192 (2001).
 64. C. Haritoglou, A. Gandorfer, and A. Kampik, "Indocyanine green can distinguish posterior vitreous cortex from internal-limiting membrane during vitrectomy with removal of epiretinal membrane," *Retina* **23**, 262 (2003).
 65. Y. Ren, R. Bu, L. Zhang, X. Huang, and Y. Li, "Implantation of radioactive particles into the cranial base and orbital apex with the use of a magnetic resonance imaging-based surgical navigation system," *Oral surgery, oral medicine, oral pathology and oral radiology* **116**, e473-477 (2013).

66. R. C. Youngquist, S. Carr, and D. E. Davies, "Optical coherence-domain reflectometry: a new optical evaluation technique," *Opt Lett* **12**, 158-160 (1987).
67. E. A. Swanson, D. Huang, M. R. Hee, J. G. Fujimoto, C. P. Lin, and C. A. Puliafito, "High-speed optical coherence domain reflectometry," *Opt Lett* **17**, 151-153 (1992).
68. C. J. Coulson, P. S. Slack, and X. Ma, "The effect of supporting a surgeon's wrist on their hand tremor," *Microsurgery* **30**, 565-568 (2010).
69. A. Bartolic, M. Santic, and S. Ribaric, "Automated tremor amplitude and frequency determination from power spectra," *Computer methods and programs in biomedicine* **94**, 77-87 (2009).
70. J. U. Kang, Y. Huang, K. Zhang, Z. Ibrahim, J. Cha, W. P. Lee, G. Brandacher, and P. L. Gehlbach, "Real-time three-dimensional Fourier-domain optical coherence tomography video image guided microsurgeries," *J Biomed Opt* **17**, 081403-081401 (2012).
71. C. Song, D. Y. Park, P. L. Gehlbach, S. J. Park, and J. U. Kang, "Fiber-optic OCT sensor guided "SMART" micro-forceps for microsurgery," *Biomed Opt Express* **4**, 1045-1050 (2013).
72. C. Song, P. L. Gehlbach, and J. U. Kang, "Active tremor cancellation by a "smart" handheld vitreoretinal microsurgical tool using swept source optical coherence tomography," *Opt Express* **20**, 23414-23421 (2012).
73. C. Song, P. L. Gehlbach, and J. U. Kang, "Swept source optical coherence tomography based smart handheld vitreoretinal microsurgical tool for tremor suppression," *Conference proceedings : ... Annual International Conference of the IEEE Engineering in Medicine and Biology Society. IEEE Engineering in Medicine and Biology Society. Annual Conference 2012*, 1405-1408 (2012).
74. C. Song, P. L. Gehlbach, and J. U. Kang, "Ball Lens Fiber Optic Sensor based Smart Handheld Microsurgical Instrument," *Proceedings of SPIE--the International Society for Optical Engineering* **8576**(2013).
75. S. Gangopadhyay and S. Sarkar, "ABCD matrix for reflection and refraction of Gaussian light beams at surfaces of hyperboloid of revolution and efficiency computation for laser diode to single-mode fiber coupling by way of a hyperbolic lens on the fiber tip," *Applied optics* **36**, 8582-8586 (1997).
76. R. P. Ratowsky, L. Yang, R. J. Deri, K. W. Chang, J. S. Kallman, and G. Trott, "Laser diode to single-mode fiber ball lens coupling efficiency: full-wave calculation and measurements," *Applied optics* **36**, 3435-3438 (1997).
77. J. Ai, J. Popelek, Y. Li, and R. T. Chen, "Beam-splitting ball lens: a new integrated optical component," *Opt Lett* **24**, 1478-1480 (1999).
78. R. G. Wilson, "Ball-lens coupling efficiency for laser-diode to single-mode fiber: comparison of independent studies by distinct methods," *Applied optics* **37**, 3201-3205 (1998).

79. A. Mortada, "Surgery of partial lamellar keratoplasty complicated by a tiny perforation of recipient corneal bed," *Bulletin of the Ophthalmological Society of Egypt* **62**, 265-270 (1969).
80. J. S. Saini, A. K. Jain, J. Sukhija, and V. Saroha, "Indications and outcome of optical partial thickness lamellar keratoplasty," *Cornea* **22**, 111-113 (2003).
81. A. Anshu, A. Parthasarathy, J. S. Mehta, H. M. Htoon, and D. T. Tan, "Outcomes of therapeutic deep lamellar keratoplasty and penetrating keratoplasty for advanced infectious keratitis: a comparative study," *Ophthalmology* **116**, 615-623 (2009).
82. I. Bahar, I. Kaiserman, S. Srinivasan, J. Ya-Ping, A. R. Slomovic, and D. S. Rootman, "Comparison of three different techniques of corneal transplantation for keratoconus," *Am J Ophthalmol* **146**, 905-912 e901 (2008).
83. J. M. Richard, D. Paton, and A. R. Gasset, "A comparison of penetrating keratoplasty and lamellar keratoplasty in the surgical management of keratoconus," *Am J Ophthalmol* **86**, 807-811 (1978).
84. S. L. Watson, A. Ramsay, J. K. Dart, C. Bunce, and E. Craig, "Comparison of deep lamellar keratoplasty and penetrating keratoplasty in patients with keratoconus," *Ophthalmology* **111**, 1676-1682 (2004).
85. M. Kawashima, T. Kawakita, S. Den, S. Shimmura, K. Tsubota, and J. Shimazaki, "Comparison of deep lamellar keratoplasty and penetrating keratoplasty for lattice and macular corneal dystrophies," *Am J Ophthalmol* **142**, 304-309 (2006).
86. M. Anwar and K. D. Teichmann, "Deep lamellar keratoplasty: surgical techniques for anterior lamellar keratoplasty with and without baring of Descemet's membrane," *Cornea* **21**, 374-383 (2002).
87. L. Fontana, G. Parente, and G. Tassinari, "Clinical outcomes after deep anterior lamellar keratoplasty using the big-bubble technique in patients with keratoconus," *Am J Ophthalmol* **143**, 117-124 (2007).
88. M. Anwar and K. D. Teichmann, "Big-bubble technique to bare Descemet's membrane in anterior lamellar keratoplasty," *Journal of cataract and refractive surgery* **28**, 398-403 (2002).
89. H. M. Anwar, A. El-Danasoury, and A. N. Hashem, "The use of fibrin glue to seal Descemet membrane microperforations occurring during deep anterior lamellar keratoplasty," *Cornea* **31**, 1193-1196 (2012).
90. A. Leccisotti, "Descemet's membrane perforation during deep anterior lamellar keratoplasty: prognosis," *Journal of cataract and refractive surgery* **33**, 825-829 (2007).
91. K. A. Knutsson, P. Rama, and G. Paganoni, "Modified big-bubble technique compared to manual dissection deep anterior lamellar keratoplasty in the treatment of keratoconus," *Acta ophthalmologica* **93**, 431-438 (2015).
92. P. Steven, C. Le Blanc, E. Lankenau, M. Krug, S. Oelckers, L. M. Heindl, U. Gehlsen, G.

- Huettmann, and C. Cursiefen, "Optimising deep anterior lamellar keratoplasty (DALK) using intraoperative online optical coherence tomography (iOCT)," *The British journal of ophthalmology* **98**, 900-904 (2014).
93. R. B. Kucumen, E. Gorgun, N. M. Yenerel, and C. A. Utine, "Intraoperative use of AS-OCT during intrastromal corneal ring segment implantation," *Ophthalmic surgery, lasers & imaging : the official journal of the International Society for Imaging in the Eye* **43**, S109-116 (2012).
 94. L. De Benito-Llopis, J. S. Mehta, R. I. Angunawela, M. Ang, and D. T. Tan, "Intraoperative anterior segment optical coherence tomography: a novel assessment tool during deep anterior lamellar keratoplasty," *Am J Ophthalmol* **157**, 334-341 e333 (2014).
 95. G. Geerling, M. Muller, C. Winter, H. Hoerauf, S. Oelckers, H. Laqua, and R. Birngruber, "Intraoperative 2-dimensional optical coherence tomography as a new tool for anterior segment surgery," *Archives of ophthalmology* **123**, 253-257 (2005).
 96. V. Scorgia, M. Busin, A. Lucisano, J. Beltz, A. Carta, and G. Scorgia, "Anterior segment optical coherence tomography-guided big-bubble technique," *Ophthalmology* **120**, 471-476 (2013).
 97. J. P. Ehlers, Y. K. Tao, S. Farsiu, R. Maldonado, J. A. Izatt, and C. A. Toth, "Integration of a spectral domain optical coherence tomography system into a surgical microscope for intraoperative imaging," *Investigative ophthalmology & visual science* **52**, 3153-3159 (2011).
 98. N. D. Pasricha, C. Shieh, O. M. Carrasco-Zevallos, B. Keller, D. Cunefare, J. S. Mehta, S. Farsiu, J. A. Izatt, C. A. Toth, and A. N. Kuo, "Needle Depth and Big-Bubble Success in Deep Anterior Lamellar Keratoplasty: An Ex Vivo Microscope-Integrated OCT Study," *Cornea* **35**, 1471-1477 (2016).
 99. B. Todorich, C. Shieh, P. J. DeSouza, O. M. Carrasco-Zevallos, D. L. Cunefare, S. S. Stinnett, J. A. Izatt, S. Farsiu, P. Mruthyunjaya, A. N. Kuo, and C. A. Toth, "Impact of Microscope-Integrated OCT on Ophthalmology Resident Performance of Anterior Segment Surgical Maneuvers in Model Eyes," *Investigative ophthalmology & visual science* **57**, OCT146-153 (2016).
 100. J. P. Ehlers, Y. K. Tao, S. Farsiu, R. Maldonado, J. A. Izatt, and C. A. Toth, "Visualization of real-time intraoperative maneuvers with a microscope-mounted spectral domain optical coherence tomography system," *Retina* **33**, 232-236 (2013).
 101. O. M. Carrasco-Zevallos, B. Keller, C. Viehland, L. Shen, G. Waterman, B. Todorich, C. Shieh, P. Hahn, S. Farsiu, A. N. Kuo, C. A. Toth, and J. A. Izatt, "Live volumetric (4D) visualization and guidance of in vivo human ophthalmic surgery with intraoperative optical coherence tomography," *Scientific reports* **6**, 31689 (2016).
 102. J. P. Ehlers, S. K. Srivastava, D. Feiler, A. I. Noonan, A. M. Rollins, and Y. K. Tao, "Integrative advances for OCT-guided ophthalmic surgery and intraoperative OCT: microscope

- integration, surgical instrumentation, and heads-up display surgeon feedback," PLoS One **9**, e105224 (2014).
103. S. Han, M. V. Sarunic, J. Wu, M. Humayun, and C. Yang, "Handheld forward-imaging needle endoscope for ophthalmic optical coherence tomography inspection," J Biomed Opt **13**, 020505 (2008).
 104. D. Lorensen, X. Yang, R. W. Kirk, B. C. Quirk, R. A. McLaughlin, and D. D. Sampson, "Ultrathin side-viewing needle probe for optical coherence tomography," Opt Lett **36**, 3894-3896 (2011).
 105. J. Lee, Y. Chae, Y. C. Ahn, and S. Moon, "Ultra-thin and flexible endoscopy probe for optical coherence tomography based on stepwise transitional core fiber," Biomed Opt Express **6**, 1782-1796 (2015).
 106. B. C. Quirk, R. A. McLaughlin, A. Curatolo, R. W. Kirk, P. B. Noble, and D. D. Sampson, "In situ imaging of lung alveoli with an optical coherence tomography needle probe," J Biomed Opt **16**, 036009 (2011).
 107. L. Scolaro, D. Lorensen, R. A. McLaughlin, B. C. Quirk, R. W. Kirk, and D. D. Sampson, "High-sensitivity anastigmatic imaging needle for optical coherence tomography," Opt Lett **37**, 5247-5249 (2012).
 108. M. R. Prausnitz and R. Langer, "Transdermal drug delivery," Nature biotechnology **26**, 1261-1268 (2008).